

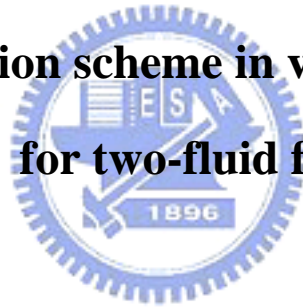
國立交通大學

機械工程學系

碩士論文

在流體體積法中使用高解析離散法計算兩相流

Use of high-resolution scheme in volume-of-fluid method  
for two-fluid flow



研究生：林仕文

指導教授：崔燕勇博士

中華民國九十七年七月

# 在流體體積法中使用高解析離散法計算兩相流

Use of high-resolution scheme in volume-of-fluid method for two-fluid flow

研究生：林仕文

Student : Shi-Wen Lin

指導教授：崔燕勇

Advisor : Yeng-Yung Tsui

國立交通大學

機械工程研究所



A Thesis

Submitted to Institute of Mechanical Engineering

Collage of Engineering

National Chiao Tung University

In Partial Fulfillment of the Requirements

For the degree of

Master of Science

In

Mechanical Engineering

July 2008

Hsinchu, Taiwan, Republic of China

## Acknowledgments

I would like to thank Prof. Yeng-Youg Tsui for his constructive criticism, guidance provided throughout my research, patience and continuous support.

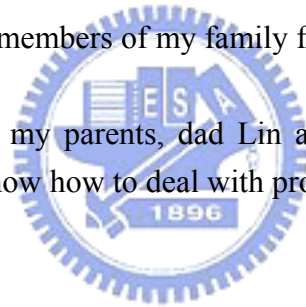
I would like to thank all individuals of CFD Laboratory.

Thanks to the seniors, Yu-Chang Hu, Tong-Ting Chen, and Tian-Cherng Wu for their teaching and helping when I have difficulties in the investigate.

Thanks to Xin-En Wu and Jun-Yan Lee for their friendships and companions. They give me great help during the two years.

Then, I would like to thank all members of my family for their attention during the two years.

Finally, I would like to thank my parents, dad Lin and mom Zhong for their support and encouragement. They let me know how to deal with problems and overcome the difficulties.



# **Use of high-resolution scheme in volume-of-fluid method for two-fluid flow**

**Student : Shi-Wen Lin**

**Advisor : Prof. Yeng-Yung Tsui**

**Institute of Mechanical Engineering**

**National Chiao Tung University**

## **ABSTRACT**

A numerical method for direct simulations of two-fluid flows is established in this study. The motion of the interface is captured by the solution of a transport equation for the volume fraction. Some numerical schemes, such as high resolution and compressive schemes are discussed in this study. The high resolution schemes preserve the shape of the interface but can not reduce the numerical diffusion. The compressive schemes are able to reach less numerical diffusion but let the interface deformed. Most composite schemes switch the compressive scheme and high resolution scheme with a switching function about the slope of the interface in order to overcome the above problem. The aim of this study is to develop a composite of the modified MUSCL and modified bounded downwind scheme with a switching function. This scheme presents the high accurate results in test cases and can be used on the quadrilateral and triangular mesh.

# 在流體體積法中使用高解析離散法計算兩相流

研究生 林仕文

指導教授 崔燕勇 博士

國立交通大學機械工程學系

## 摘要

在本研究中將建立一種直接模擬兩相流的數值方法。在此方法中，藉由求解流體體積分率的傳輸方程式，來抓取兩流體間的介面運動。在本研究中將討論許多數值的離散法，像是高解析離散法和壓縮式離散法。高解析離散法可以維持兩流體間界面的外形，卻沒有辦法減少在介面上的數值擴散。而壓縮式離散法可以達到較少的數值擴散，卻會造成介面形狀的變形。為了處理上述的問題，大部分混合離散法都是採用一個與介面斜率相關的轉換函數，在高解析離散法和壓縮式離散法之間做切換。本研究主要的目的是在於發展一種在 modified MUSCL 和 modified bounded downwind scheme 之間轉換的混合離散法。此方法在本文中所測試的案例中都有相當高的準確性，而且本方法可以在三角形和四邊形的網格系統中使用。

# Content

<b>ABSTRACT</b> .....	iii
<b>Content</b> .....	v
<b>List of Table</b> .....	vii
<b>List of Figure</b> .....	viii
<b>Nomenclature</b> .....	xii
<b>Abbreviation</b> .....	xiv
<b>Chapter1 Introduction</b> .....	1
1.1 Background .....	1
1.2 Related studies .....	2
1.2.1 Lagrangian schemes .....	2
1.2.2 Eulerian schemes .....	2
1.3 Outline of this thesis .....	7
<b>Chapter2 Mathematical Model</b> .....	9
2.1 Introduction .....	9
2.2 General transport equation .....	9
2.3 Mass and momentum conservation equation .....	10
2.4 VOF equation .....	10
2.5 Surface tension .....	12
2.6 Boundary conditions .....	13
<b>Chapter3 Numerical Method</b> .....	14
3.1 Introduction .....	14
3.2 Discretization of the VOF equation .....	14
3.3 Discretization of the momentum equation .....	15
3.3.1 Unsteady term .....	15
3.3.2 Convection term .....	16
3.3.3 Diffusion term .....	16
3.3.4 Source term .....	17
3.3.5 Arrangement of the difference transport equation .....	18
3.4 Pressure-velocity coupling of the PISO algorithm .....	18
3.5 Solution procedure .....	24
<b>Chapter4 High Resolution Differencing Schemes</b> .....	25
4.1 Introduction .....	25
4.2 Convective flux of volume fraction .....	25
4.3 CBC and TVD constraints .....	27
4.4 Linear and non-linear schemes .....	27
4.5 Composite scheme with switching function .....	28
<b>Chapter5 Results and Discussion</b> .....	32
5.1 Introduction .....	32

5.2 Uniform density flow .....	32
5.3 Shear flow .....	34
5.4 Broken dam .....	36
5.5 Filling process in an open tank .....	38
<b>Chapter6 Conclusion and Future Work .....</b>	<b>40</b>
<b>Chapter7 Reference .....</b>	<b>41</b>



## List of Table

Table 4.1 The NVD equation and flux limiter function of linear and non-linear difference schemes .....	47
Table 5.1 Errors of different schemes in $Co = 0.25$ (quadrilateral mesh) .....	48
Table 5.2 Errors of different schemes in $Co = 0.75$ (quadrilateral mesh) .....	48
Table 5.3 Errors of different schemes in $Co = 0.25$ (triangular mesh).....	48
Table 5.4 Errors of different schemes in $Co = 0.75$ (triangular mesh).....	49
Table 5.5 Errors of different composite schemes in $Co = 0.25$ (quadrilateral mesh) .....	49
Table 5.6 Errors of different composite schemes in $Co = 0.75$ (quadrilateral mesh) .....	49
Table 5.7 Errors of different composite schemes in $Co = 0.25$ (triangular mesh)	49
Table 5.8 Errors of different composite schemes in $Co = 0.75$ (triangular mesh)	49





## List of Figure

Figure 1.1 The method of two-fluid flow (a) Lagrangian (b) Eulerian scheme .	50
Figure 1.2 Front tracking method.....	51
Figure 1.3 Marker and cell method .....	51
Figure 1.4 Line techniques .....	52
Figure 1.5 Donor and acceptor cell configuration.....	53
Figure 2.1 General form of the conservation law .....	54
Figure 2.2 VOF method on the Eulerian grids.....	54
Figure 2.3 Continuity of the velocity and discontinuity of the momentum.....	55
Figure 2.4 Fluid arrangements and the sign of the curvature .....	55
Figure 3.1 Illustration of the primary cell P and the neighbor cell nb with a considering face.....	56
Figure 4.1 The relationship of a control volume and its neighbor cells .....	57
Figure 4.2 The CBC constraint in NVD.....	57
Figure 4.3 The CBC constraint in NVD.....	58
Figure 4.4 The TVD condition in TVD diagram .....	58
Figure 4.5 Linear schemes in Normalized Variable Diagram.....	59
Figure 4.6 Linear schemes in TVD Diagram.....	59
Figure 4.7 SMART .....	60
Figure 4.8 MUSCL.....	60
Figure 4.9 SUPERBEE .....	60
Figure 4.10 STOIC .....	61
Figure 4.11 OSHER .....	61
Figure 4.12 BDS.....	61
Figure 4.13 Van Leer .....	62
Figure 4.14 CHARM.....	62
Figure 4.15 Modified BDS.....	62
Figure 4.16 Modified MUSCL.....	63
Figure 4.17 The NVD of (a) HYPER-C and (b) UQ ( $C_0 = 0.5$ ).....	63
Figure 4.18 The switching function of CICSAM scheme .....	64
Figure 4.19 The switching function of HRIC scheme .....	64
Figure 4.20 The switching function of the composite of M-MUSCL and M-BDS .....	64
Figure 5.1 (a) The constant velocity field and initial position of hollow circle .	65
Figure 5.1 (b) The constant velocity field and initial position of hollow square	65
Figure 5.2 Triangular computational mesh in uniform density flow (22478 cells) .....	66

Figure 5.3 (a) The exact distribution of the hollow circle .....	67
Figure 5.3 (b) The exact distribution of the hollow square.....	67
Figure 5.4 The final shape of hollow circle from different schemes in quadrilateral mesh.....	68
Figure 5.5 The final shape of hollow square from different schemes in quadrilateral mesh .....	69
Figure 5.6 The final shape of hollow circle from different schemes in triangular mesh.....	70
Figure 5.7 The final shape of hollow square from different schemes in triangular mesh.....	71
Figure 5.8 The final shape of hollow circle from different composite schemes in quadrilateral mesh .....	72
Figure 5.9 The final shape of hollow square from different composite scheme in quadrilateral mesh .....	73
Figure 5.10 The final shape of hollow circle from different composite scheme in triangular mesh.....	74
Figure 5.11 The final shape of hollow square from different composite scheme in triangular mesh.....	75
Figure 5.12 The volume fraction distribution in a shear flow field.....	76
Figure 5.13 Triangular mesh in uniform density flow (22494 cells).....	76
Figure 5.14 The volume fraction distribution in shear flow with $Co=0.25$ (quadrilateral mesh).....	77
Figure 5.15 The volume fraction distribution in shear flow with $Co=0.25$ (quadrilateral mesh).....	78
Figure 5.16 The volume fraction distribution in shear flow with $Co=0.25$ (quadrilateral mesh).....	79
Figure 5.17 The volume fraction distribution in shear flow with $Co=0.25$ (quadrilateral mesh).....	80
Figure 5.18 The volume fraction distribution in shear flow with $Co=0.75$ (quadrilateral mesh).....	81
Figure 5.19 The volume fraction distribution in shear flow with $Co=0.75$ (quadrilateral mesh).....	82
Figure 5.20 The volume fraction distribution in shear flow with $Co=0.75$ (quadrilateral mesh).....	83
Figure 5.21 The volume fraction distribution in shear flow with $Co=0.75$ (quadrilateral mesh).....	84
Figure 5.22 The volume fraction distribution in shear flow with $Co=0.25$ (triangular mesh) .....	85

Figure 5.23 The volume fraction distribution in shear flow with $Co=0.25$ (triangular mesh) .....	86
Figure 5.24 The volume fraction distribution in shear flow with $Co=0.25$ (triangular mesh) .....	87
Figure 5.25 The volume fraction distribution in shear flow with $Co=0.25$ (triangular mesh) .....	88
Figure 5.26 The volume fraction distribution in shear flow with $Co=0.75$ (triangular mesh) .....	89
Figure 5.27 The volume fraction distribution in shear flow with $Co=0.75$ (triangular mesh) .....	90
Figure 5.28 The volume fraction distribution in shear flow with $Co=0.75$ (triangular mesh) .....	91
Figure 5.29 The volume fraction distribution in shear flow with $Co=0.75$ (triangular mesh) .....	92
Figure 5.30 Comparison of errors in the shear flow with $Co=0.25$ (quadrilateral mesh) .....	93
Figure 5.31 Comparison of errors in the shear flow with $Co=0.75$ (quadrilateral mesh) .....	93
Figure 5.32 Comparison of errors in the shear flow with $Co=0.25$ (triangular mesh) .....	94
Figure 5.33 Comparison of errors in the shear flow with $Co=0.75$ (triangular mesh) .....	94
Figure 5.34 Schematic of the broken dam .....	95
Figure 5.35 Experimental results of a collapsing water column by Koshizuka .	96
Figure 5.36 Schematic representation of the non-uniform and quadrilateral mesh with $56 \times 36$ grids in broken dam .....	97
Figure 5.37 Schematic representation of the triangular mesh with 4506 cells in broken dam .....	97
Figure 5.38 Schematic representation of the triangular mesh with 12354 cells in broken dam .....	97
Figure 5.39 Numerical results of the broken dam on the uniform and quadrilateral mesh with $48 \times 28$ grids .....	98
Figure 5.40 Numerical results of the broken dam on the uniform and quadrilateral mesh with $120 \times 70$ grids .....	99
Figure 5.41 Numerical results of the broken dam on the non-uniform and quadrilateral mesh with $56 \times 36$ grids .....	100
Figure 5.42 Numerical results of the broken dam on the triangular mesh with 4506 cells .....	101

Figure 5.43 Numerical results of the broken dam on the triangular mesh with 12354 cells.....	102
Figure 5.44 The position of the leading edge in broken dam .....	103
Figure 5.45 The height of the collapsing water in broken dam .....	103
Figure 5.46 Schematic representation of the filling process in an open tank ...	104
Figure 5.47 Schematic representation of the triangular mesh with 902 cells in filling process .....	104
Figure 5.48 Schematic representation of the triangular mesh with 2024 cells in filling process .....	105
Figure 5.49 Schematic representation of the triangular mesh with 3584 cells in filling process .....	105
Figure 5.50 The volume fraction distribution and velocity field of the filling process on the uniform and quadrilateral mesh with $28 \times 28$ .....	106
Figure 5.51 The volume fraction distribution and velocity field of the filling process on the uniform and quadrilateral mesh with $40 \times 40$ grids .....	107
Figure 5.52 The volume fraction distribution and velocity field of the filling process on the uniform and quadrilateral mesh with $80 \times 80$ grids.....	108
Figure 5.53 The volume fraction distribution and velocity field of the filling process on the triangular mesh with 902 cells .....	109
Figure 5.54 The volume fraction distribution and velocity field of the filling process on the triangular mesh with 2024 cells .....	110
Figure 5.55 The volume fraction distribution and velocity field of the filling process on the triangular mesh with 3584 cells .....	111
Figure 5.56 The position of leading of the filling process in the open tank .....	112
Figure 5.57 The water volume inside the tank.....	112

## Nomenclature

$A$	Coefficient of algebraic equation
$Co$	Courant number
$F_C$	Boundary flux due to convection
$F_D$	Boundary flux due to diffusion
$f$	Face, point in the centre of the face
$f_\sigma$	Surface tension force
$g$	Gravitational acceleration
$\dot{m}_f$	Mass flow rate cross face
$P$	Pressure
$Q_\phi$	Source term in discretized momentum equation
$S_\alpha$	Source term in discretized the indicator equation
$t$	Time
$w_f$	Weighting factor
$x, y$	Components of Cartesian coordinate
$\vec{\delta d}$	Vector pointing from center of primary cell to the center of neighbor one
$\phi$	Property
$\Delta V$	Volume
$\gamma(r)$	Flux limiter equation
$\alpha$	Volume fraction
$\sigma$	Surface tension coefficient
$\rho$	Fluid density
$\mu$	Viscosity coefficient

$\Delta$	Difference operator
$\nabla$	Gradient
$\theta_f$	Angle between the normal to interface and orthogonal component of the face area vector
$\psi(\theta_f)$	Switching function
$n$	New time level
$o$	Old time level



## Abbreviation

BDS	Bounded Downwind Scheme
CBC	Convective Boundedness Criterion
CDS	Central Difference Scheme
CICSAM	Compressive Interface Capturing Scheme for Arbitrary Meshes
CUS	Cubic upwind difference scheme
CV	Control Volume
DDS	Downwind Difference Scheme
HRS	High Resolution Scheme
LUS	Linear Upwind Scheme
MAC	Marker and cell
MUSCL	Monotonic Upwind Scheme for Conservation Law
NVD	Normalized Variable Diagram
PISO	Pressure Implicit with Splitting of Operator
QUICK	Quadratic Upwind Interpolation for Convection Kinematics
SLIC	Simple Line Interface Calculation
SMART	Sharp and Monotonic Algorithm for Realistic Transport
STOIC	Second- and Third-Order Interpolation for Convection
TVD	Total Variation Diminishing
UDS	Upwind Difference Scheme
UQ	ULTIMATE-QUICKEST
M-MUSCL	Modified Monotonic Upwind Scheme for Conservation Law
M-BDS	Modified Bounded Downwind Scheme

# Chapter1 Introduction

## 1.1 Background

The flow involving two immiscible fluids has been of interest to many investigators during the last decades. How to predict the position and the movement of the interfaces in the two-fluid flow accurately is very important in many scientific and technical applications. The objective of this study is the development of a numerical method which can cope with the above problem. In many engineering problems and industrial processes, such as marine engineering, biochemical engineering, tube/channel flows, and casting, welding, molding, injection or extrusion processes, the simulation of two-phase flow with discrete interface is a rather popular issue. This simulation has also played an important part in IC package process and the production of LED screen. In marine engineering, some numerical results of free surface flow with wave breaking are applied to the motion of sea water. Muzaferija et al. have presented the flow around ship hulls or submerged hydrofoils [1]. In biochemical engineering, this technique is used to simulate the transportation of biochemical fluids in the capillary channels, such as the blood in veins. On the other areas, mold-filling process with heat transfer is an important application in casting. K.A. Percleous et al. investigate the collapse of a liquid column in a sealed cavity and simulate cooling process of a step-like model which is a common test one [2]. In the tube/channel flows area, the numerical results of two-phase flow are widely employed. In [3], Yang et al. present the flow boiling of refrigerant R134B in a horizontal coiled tube. They predict the temperature profile and the phenomenon of the flow boiling in the straight and bending parts of the coiled tube. In [4], the simulation of two-phase flow can also be used in the fuel cell. Yun Wang et al. [4] have developed a two-phase model for the flow in mini-channels of a proton exchange membrane (PEM) fuel cell. The results of their investigations can be applicable to many common two-phase flow behaviors across the micro- or mini- channels. Although the application of the two-phase flow is so extensive, the representative problems of the flow with two immiscible fluids can be classified into three



categories [5]. The first one is dispersed flow that the two fluids in the flow field are considered as suspensions without a defined interface. The second is that the two fluids are separated by a sharp interface without breaking. The third is the transitional flow that the interface of two-phase flow may or may not be broken. In this study, the numerical method mainly deals with the last two problems.

## **1.2 Related studies**

Several numerical methods of two-fluid flow with a moving interface have been posed. The methods which are used to predict the phenomenon of two-phase flow can be divided into two main categories: Lagrangian and Eulerian schemes (Fig. 1.1) [6].

### **1.2.1 Lagrangian schemes**

The first method can keep free surface sharp between the two fluids and present the exact position of the free surface with re-meshing as the calculation proceeds. The mesh of this scheme is deformed and changed all the time. The main procedure of this method is that the position of the free surface at next time step is calculated by using the velocity field which is known. When the new free surface boundary is defined, we can reconstruct grids and update new properties for the new flow field [7]. The position of the interface can be predicted precisely, because the boundary mesh matches the free surface. Although the accurate prediction of the free surface can be carried out by the Lagrangian scheme, this method can not be employed to the quite complex flow field. Many deformations and stretches which result from the breaking, overturning, or gravity wave may cause numerical errors as well as reducing the precision. In [8], there is a Lagrangian scheme which is presented by Peric et al. This scheme can be employed in some simple and no large interface deforming cases, but its drawback is that the scheme cannot be used while the interface is unfolded.

### **1.2.2 Eulerian schemes**

The second method can reduce errors which result from the deforming grids by using fixed grids that are generated before calculating the movement of the interface. The main

disadvantage of this method is the fact that it is prone to result in numerical diffusion. The diffusion will make the interface to spread over several mesh cells and the interface between the two immiscible fluids is going to be no longer sharp. In reality, the interface remains sharp due to the surface tension and the action of gravity, which separates immiscible fluids of different densities [2]. The interface of the two-phase flow must be tracked by employing some special treatments because its motion can not match the mesh any more as the calculation proceeds. A lot of techniques have been developed to cope with the problems of the multi-fluid flow systems in the past decade. These techniques can be classified to three main categories: 1. tracking the interface by using a set of mass-less particles; 2. using several mass-less marker particles to point out the only one kind of fluids and interface; 3. capturing the interface by an indicator function, such as a level set function or a volume fraction function. There are several Eulerian schemes will be introduced in the following part.

#### **(A) Front tracking method**

This front tracking method [9] (Fig. 1.2) is applied to construct the interface between the liquid and gas by a simple trajectory technique. A lot of mass-less particles are uniformly distributed over the interface in the first instance, but the Navier-Stokes equations are solved in a fixed and Eulerian grid system. The numbers of particles on the interface may be increased or reduced as the calculation proceeds. The new positions of these particles can be obtained by integrating the Eulerian fluid velocity field near the particles for each time step. This method has been used to deal with the motion of rising bubble, the breaking of water waves, and the collapse of an unsupported water column. This method is quite accurate but rather complex. Its first drawback is that the re-meshing of the Lagrangian mesh is needed. Another difficult is that transforming the mesh data of the Lagrangian system into the Eulerian is quite complicated. In the three-dimensional problems, the front tracking method has another problem because the particles on the interface are not a string one any more. This problem will cause the calculational time and the computer storage to increase significantly.

## **(B) Level set method**

A level set method for moving interfaces was proposed in [10]. The interface is identified as the zero level set of a smooth distance function from the front of the interface. This method not only eliminates the problems of the numerical diffusion which will smear the sharp front, but also avoids adding or reducing points to the moving grid. This method presents the interface by solving a scalar convection equation of the level set function. This method is easy to code due to the use of Eulerian grid and can result in more accurate results when the flow motion of the interface coincides with one of the coordinate axis. This method can also be easily generalized to three dimensions. However, the main drawback of this method is that level set methods loses its accuracy because the mass is not conserved when the interface is significantly deformed. Sussman et al. used it to simulate the flows of bubbles and droplets [10], and Li presented the results of Rayleigh-Taylor instability [11].

## **(C) Marker and cell method**

Marker and cell method (MAC) (Fig 1.3) was proposed by Harlow and Welch in [12]. Several mass-less marker particles are distributed over a space which is filled with one particular fluid with a free surface, and these marker particles are used to calculate the motion of the flow field including the free surface. This method is quite accurate and can be used accurately to deal with many complex problems, such as an interface subjected to shearing and vorticity, and wave breaking in two-dimensional system, but it may become expensive of operating in three-dimensional one. More marker particles will be added when treating problems with interface stretching, shrinking, breaking, or merging in three dimensions. The above process results in increase of computational time and computer storage. There have been many studies about this method [13, 14].

## **(D) Volume-of-fluid method**

In volume-of-fluid method, the fluids of two-fluid flow are represented by one scalar indicator function called volume fraction. The value of the volume fraction is bounded

between zero and unity. The value of unity denotes one of the fluids. The value of zero denotes the other fluid. The volume fraction value between zero and unity indicate the interface. This method is quite popular and easy to code in the finite-volume method. The scalar indicator function is convected through the computational domain by solving a scalar convective equation like other transport equations. The scalar indicator function can not maintain a step function on the interface because most convective schemes result in numerical diffusion and dispersion. There are three categories of this volume-of-fluid method as follows.

### **Line techniques**

This method has been implemented in two-dimensional problems, but the reconstruction of the interface in three-dimensional flows is difficult. The methods are used for interface reconstruction can be classified into three categories as follows.

The first method is SLIC method (Simple Line Interface Calculation) which was proposed by Noh and Woodward in 1976 [15]. The interface is approximated by using lines parallel to one of the coordinate axes. The volume fractions of the left and right cells of the prime cell are used to reconstruct the interface in the prime cell approximately when the sweeping direction coincides with the x-axis. On the other hand, the volume fractions in the cells above and under the prime cell are used in the y-axial sweeping. The second method is the one with improvement on the SLIC method by Chorin [16]. All direct neighbors of the prime cell will be used for interface reconstruction in the prime cell. The third method (PLIC or Youngs' VOF) which is posed by Youngs [17] is more accurate than the SLIC method. In this method, the interface is approximated by using oblique lines. Unlike the SLIC method, all neighboring cells are used to approximate the slope of the interface in Youngs' VOF. The above methods are illustrated in figure 1.4.

### **Donor-acceptor techniques**

In this method, the value of the volume fraction transported through a cell face between two cells can be approximated by the volume fraction value of the downwind cell (Figure 1.5).

This method will cause the volume fraction values unbounded, i.e. the values of the volume fraction may become greater than one or less than zero. In order to ensure the boundedness, the method which improves the level of volume fraction value on the face by using the value of the donor cell is proposed by Ramshaw and Trapp [18] , but it will cause the incorrect steeping on the interface due to change any finite gradient into a step. As mention above, the volume fraction on the face correlates closely with the flow and interface direction. Another method was proposed to cope with the above problem in [19]. Hirt and Nichols calculate the volume fraction value on the face by including some information on the slope of the interface into fluxing algorithm.

### **High-order differencing schemes**

In this method, the convective scalar transport equation is discretised by using a high order scheme or a blending scheme to predict the interface of two-fluid system. The main errors of this method are numerical diffusion which smears the front of the fluids and numerical dispersion which causes non-physical oscillation. The first-order upwind scheme has the numerical diffusion. This diffusion becomes significantly strong when the flow direction is normal to the interface direction. In order to reduce the numerical diffusion, the linear upwind scheme (LUDS) [20] and the quadratic upstream interpolation for convective kinematics (QUICK) scheme [21] were proposed. The former is second-order accurate and interpolated by the two upwind values. The latter is third-order accurate and interpolated by the two upwind and one downwind values. These high order schemes can reduce numerical diffusion, but they may cause numerical dispersion, such as oscillations, in the strong gradient regions.

In order to cope with the dispersion problem, the flux-blending and flux-limiter technique have been proposed. The former can be classified into two classes. The first class is based on adding an anti-diffusion flux to a first order upwind scheme [22] and used to resolve sharp gradient without over-/under-shoots. The second method is based on introducing some

smoothing diffusive fluxes into an unbounded high-order scheme, and it can prevent oscillations. The flux-blending technique will become expensive due to their multi-step nature and balancing the two fluxes. In [22], the flux corrected transport (FCT) method has posed. FCT schemes are non-diffusive in nature, but create unphysical flotsam and jetsam.

The flux-limiter technique can remove non-physical oscillations and is based on the numerical flux on the interface of a cell which can be adjusted by using the flux-limiter function that enforce the boundedness. High resolution schemes (HRs) [23] are the schemes which obey the above criterion. The methods, such as Normalized Variable (NV) and Normalized Variable Diagram (NVD) [24], can be used to employ the flux-limiter technique. The flux limiter function is presented by Van Leer [25]. Sweby developed the Total Variation Diminishing (TVD) [26] approach for high resolution schemes. In the past decades, many high resolution schemes have been proposed, such as SMART of Gaskell and Lau [27], GAMMA of Jasak [28], SUPERBEE of Roe [29], STOIC of Darwish [30], MUSCL and Van Leer of Van Leer [31].

Numerical diffusion can be classified into two main components, namely cross-stream and stream-wise. These two numerical diffusions can be associated with the angle between the flow and interface direction. The blending strategy was proposed in order to improve the accuracy and less numerical diffusion including cross-stream and stream-wise. The key issue in the composite scheme is not just when to switch, but how to switch [32]. Hence, the best approach must have a continuous switching function whereby the values of compressive and high resolution schemes are blended together with a blending factor. This method has been used in utilized in the HRIC of Muzaferija [33], STACS of Darwish [34], CICSAM of Ubbink [35] and the composite of MUSCL and SUPERBEE [36].

### **1.3 Outline of this thesis**

In this study, a high resolution scheme with switching function in the volume-of-fluid method used to solve the two-fluid flow is employed. This composite scheme can enhance the

accuracy of numerical results, preserve the sharpness on the interface and prevent the smearing.

In Chapter 2, the governing equations used to simulate the two-fluid flow, such as the continuity, momentum and volume-of-fluid equations will be introduced. The surface tension term in the momentum equation and the boundary conditions used in our simulation will be addressed.

In Chapter 3, governing equations will be discretized by using the finite volume method. The coupling between the velocity and pressure is treated by the PISO algorithm. The solution procedure of our numerical method will be introduced.

In Chapter 4, the method used to calculate the face value of the volume fraction will be introduced, and several schemes will be formulated. The former switching function will be introduced and a new composite scheme will be developed.

In Chapter 5, four cases will be tested. The first two cases, such as uniform density flow and shear flow will be used to evaluate the accuracy and availability of our numerical method by comparing with the result in the previous papers. The last two cases will be simulated by the new composite scheme. The results of them will show the superiority and accuracy of this method against the other composite schemes.

In Chapter 6, the main conclusions and discussion of this thesis are given.

## Chapter2 Mathematical Model

### 2.1 Introduction

In our calculation, the different fluids can be defined as a single and continuous fluid, and the fluid properties have a jump at the interface. The volume fraction is denoted as a step function on the interface. This volume fraction will be used to affect the properties of the fluid and separate the two immiscible fluids by a well defined interface. The main subject of this chapter is the description of the mathematical model which is used to solve the two-fluid system. In this study, there are several basic assumptions in our mathematical model. The model simulates the unsteady, incompressible, viscous, two-dimensional, and two-fluid systems, and the body force term includes both gravity and surface tension force. The surface tension term is a rather important effect on the interface in the two-fluid flow. The surface tension is modeled by the continuum surface force (CSF) model proposed by Brackbill et al. [37].

### 2.2 General transport equation

The conservation laws for mass, momentum, and energy are used to describe the physical behavior of the fluid flow. The general form of the conservation equation for a flow property  $\phi$  in the control volume (C.V.) system shown in figure 2.1, is

$$\frac{\partial}{\partial t} \int_V \phi dV + \oint_S F_C \cdot d\vec{S} = \oint_S F_D \cdot d\vec{S} + \int_V Q_V dV + \oint_S Q_S \cdot d\vec{S} \quad (2.1)$$

where  $t$  is the time,  $Q_V$  the internal source,  $Q_S$  the source at the boundary,  $F_C = \rho \vec{V} \phi$  the flux over the boundary due to convection,  $\vec{V}$  the fluid velocity,  $F_D$  the flux over the boundary due to diffusion,  $V$  the control volume and  $S$  the control surface. We can use the Gauss's theorem to rewrite equation (2.1):

$$\frac{\partial}{\partial t} \int_V \phi dV + \int_V \nabla \cdot F_C dV = \int_V \nabla \cdot F_D dV + \int_V Q_V dV + \int_V \nabla \cdot Q_S dV \quad (2.2)$$

The above equation can be rewritten to the general conservative differential form when the control volume is contracted to a single point:



$$\frac{\partial \varphi}{\partial t} + \nabla \cdot F_C = \nabla \cdot F_D + Q_V + \nabla \cdot Q_S \quad (2.3)$$

### 2.3 Mass and momentum conservation equation

The conservation equations for mass and momentum can be obtained by substituting  $\varphi=\rho$  by neglecting the diffusion term and the source terms, and  $\varphi=\vec{V}$  with the assumption of a laminar Newtonian working fluid under unsteady and incompressible conditions with body force and surface tension force. The mass and momentum conservation equations can be written as following:

$$\frac{\partial \rho}{\partial t} + \nabla \cdot \rho \vec{V} = 0 \quad (2.4)$$

$$\frac{\partial \rho \vec{V}}{\partial t} + \nabla \cdot (\rho \vec{V} \vec{V}) = -\nabla p + \nabla \cdot (\mu \nabla \vec{V}) + \rho g + f_\sigma \quad (2.5)$$

where  $\rho$  is the fluid density,  $\vec{V}$  the velocity,  $P$  the pressure,  $\mu$  the viscosity coefficient,  $g$  the gravitational acceleration and  $f_\sigma$  the surface tension.

The density and viscosity of the effective fluid in the equation (2.4) and (2.5) can be calculated by the volume fraction, as

$$\rho = \rho_1 \alpha + \rho_2 (1 - \alpha) \quad (2.6)$$

$$\mu = \mu_1 \alpha + \mu_2 (1 - \alpha) \quad (2.7)$$

where the subscripts 1 and 2 denote the two fluids,  $\alpha$  is the volume fraction. The density and viscosity of the different fluids are considered as variables through the full domain but constants in each kind of fluids. As mentioned above, all properties are piecewise continuous due to the volume fraction.

### 2.4 VOF equation

In the following, we will define different fluids by using the volume fraction in the volume-of-fluid (VOF) method on the Eulerian grid system (see figure 2.2). The value of volume fraction can be defined as

$$\alpha = \frac{\text{Volume of fluid 1}}{\text{Total Volume of Control Volume}} \quad (2.8)$$

Therefore, the fluids through the entire computational domain can be divided into three

categories by the volume fraction as

$$\alpha = \begin{cases} 1 & \text{for the points inside the fluid 1} \\ 0 & \text{for the points inside the fluid 2} \\ 0 < \alpha < 1 & \text{for the points inside the transitional region} \end{cases} \quad (2.9)$$

The two-fluid system is propagated as the Lagrangian invariant and thus has a zero material derivative [19]:

$$\frac{D\alpha}{Dt} = \frac{\partial\alpha}{\partial t} + \vec{V} \cdot \nabla\alpha = 0 \quad (2.10)$$

The above equations (2.4) to (2.10) can describe the fluid flow of the two-fluid system. However, the form of the volume fraction, shown as (2.10), is not a conservative one and is not suitable for numerical solution. Because of the reason, it must to be reformulated [33]. The mass conservation equation (2.4) is a conservation form. It can be rewritten as

$$\begin{aligned} \frac{\partial\rho}{\partial t} + \vec{V} \cdot \nabla\rho + \rho\nabla \cdot \vec{V} &= 0 \\ \Rightarrow \nabla \cdot \vec{V} &= \frac{-1}{\rho} \left( \frac{\partial\rho}{\partial t} + \vec{V} \cdot \nabla\rho \right) = -\frac{1}{\rho} \left( \frac{D\rho}{Dt} \right) = -\frac{D(\ln\rho)}{Dt} \end{aligned} \quad (2.11)$$

This non-conservation form of the mass conservation equation is much suitable for the two-fluid system with high density ratio, because the  $\vec{V}$  on the interface is defined as continuous. Figure 2.3 shows the densities at the inlet and outlet are not the same in the closed domain. The velocity  $\vec{V}$  of the fluid of entering and leaving the domain is the same, but the momentum  $\rho\vec{V}$  of the fluid entering and leaving the domain is different. In addition, the fluids of this study are the assumption that they are incompressible. By substituting equation (2.6) into equation (2.11) the non-conservative equation becomes

$$\begin{aligned} \nabla \cdot \vec{V} &= \frac{-1}{\rho} \frac{D}{Dt} [\alpha(\rho_1 - \rho_2) + \rho_2] \\ &= \frac{\rho_2 - \rho_1}{\rho} \left( \frac{D\alpha}{Dt} \right) \\ &= 0 \end{aligned} \quad (2.12)$$

The equation (2.10) can be rearranged into a conservation form with the incompressible

condition by recognizing that  $\nabla \cdot \alpha \vec{V} = \alpha \cdot \nabla \vec{V} + \vec{V} \cdot \nabla \alpha$  as:

$$\frac{\partial \alpha}{\partial t} + \nabla \cdot \alpha \vec{V} = 0 \quad (2.13)$$

In the present study, the continuity equation (2.12), the momentum equation (2.5) and the VOF equation (2.13) together with the equation (2.6) and (2.7) will be employed to model the two-fluid flow.

## 2.5 Surface tension

As mentioned above, the surface tension will be modeled by the continuum surface force (CSF) model [37]. Surface tension creates a pressure jump which supplies the mean interface curvature with its necessary work on the interface. The surface tension coefficient  $\sigma$  exists for any pair of fluids and its magnitude is determined by the nature of the fluids. The value of  $\sigma$  is always positive for immiscible fluids and negative for miscible fluids [38]. The pressure jump is a function of the mean interface curvature, and it can be shown as [39]:

$$\Delta P = P_i - P_o = \sigma \left( \frac{1}{R_1} + \frac{1}{R_2} \right) = \sigma \kappa \quad (2.14)$$

where  $R_1$  and  $R_2$  are the principal radii of curvature of the surface,  $P_i$  is the pressure on the concave side of the curved surface,  $P_o$  the pressure on the convex side,  $\sigma$  is the surface tension coefficient and  $\kappa$  is the mean interface curvature. For  $\kappa > 0$  fluid 1 lies on the concave side of the interface and for  $\kappa < 0$  fluid 2 lies on the concave side (figure 2.4). The gradient of  $\alpha$  which is zero everywhere except at transient region, gives the normal vector, which always point from fluid 2 toward fluid 1 (figure 2.4):

$$\vec{n} = \nabla \alpha \quad (2.15)$$

Thus, the mean interface curvature  $\kappa$  can be rewritten in terms of divergence of the unit normal vector as:

$$\kappa = -\nabla \cdot \left( \frac{\vec{n}}{|\vec{n}|} \right) = -\nabla \cdot \left( \frac{\nabla \alpha}{|\nabla \alpha|} \right) \quad (2.16)$$

By substituting equation (2.16) into equation (2.14), the surface tension term in the

momentum equation can be expressed as

$$f_{\sigma} = \nabla P = \Delta P \vec{n} = \sigma \kappa \nabla \alpha = -\sigma \nabla \cdot \left( \frac{\nabla \alpha}{|\nabla \alpha|} \right) \nabla \alpha \quad (2.17)$$

## 2.6 Boundary conditions

**Inlet:** A velocity distribution is specified at the inlet.

**Outlet:** The outlet boundary condition uses the fixed pressure boundary condition. The boundary values are obtained from convective boundary condition [40]

$$\frac{\partial \phi}{\partial t} + \vec{V}_c \cdot \nabla \phi = 0 \quad (2.18)$$

where  $\phi$  represent the transported property and  $\vec{V}_c$  is the convective velocity.

**Rigid boundary (walls):** A rigid boundary is generally defined as a non-slip boundary condition ( $u=0, v=0$ ).



## Chapter3 Numerical Method

### 3.1 Introduction

In the chapter 2, the mathematical model of the two-fluid flow has been described in detail. It is a necessary to choose a suitable discretization method, such as the finite difference (FD), finite volume (FV) or the finite element (FE) methods. These methods approximate the differential equations by a system of algebraic equations. Finite volume method is the method which uses integral form of conservation equations. The calculated domain can be divided into many several control volumes. In our computation, the VOF equation and the momentum will be discretized by using the finite volume method. The coupling between pressure and velocity will be treated by the PISO algorithm [41].

### 3.2 Discretization of the VOF equation

The finite volume method for the VOF equation of equation (2.13) is first integrated over a control volume, and then can be transformed by the Gauss divergence theory as:

$$\int_V \frac{\partial \alpha}{\partial t} dV + \int_V \nabla \cdot \alpha \vec{V} dV = 0 \quad (3.1)$$

$$\int_C \frac{\partial \alpha}{\partial t} dV + \oint_S \alpha \vec{V} \cdot d\vec{S} = 0 \quad (3.2)$$

The unsteady term can be discretized as:

$$\int_V \frac{\partial \alpha}{\partial t} dV \approx \frac{\Delta V}{\Delta t} (\alpha_D^n - \alpha_D^o) \quad (3.3)$$

where  $\Delta V$  is the volume of the cell, the superscripts n and o denote respectively the new and old time steps, D is the donor cell.

The second term can be discretized as:

$$\oint_S (\vec{V} \alpha) \cdot d\vec{S} \approx \sum_f (\vec{V} \alpha^*)_f \cdot \vec{S}_f \quad (3.4)$$

where

$$\alpha_f^* = \frac{1}{2} (\alpha_f^n + \alpha_f^o) \quad (3.5)$$

where the subscript  $f$  denotes the properties on the surface of a control volume.

In the above equation, the value of  $\alpha_f^*$  is obtained by using the second-order Crank-Nicolson scheme.

The volume fraction on the considering face can be determined by a function of neighbor cells and a flux limiter function  $\gamma(r)$ , which will be introduced in next chapter, shown as:

$$\alpha_f = \alpha_D + \gamma(r) \left( \frac{\alpha_A - \alpha_D}{2} \right) \quad (3.6)$$

Substituting the above equations into equation (3.1) yields

$$A_P \alpha_P^n = \sum_{nb} A_{nb} \alpha_{nb}^n + S_\alpha \quad (3.7)$$

$$A_P = \sum_{nb} A_{nb} + \frac{\Delta \forall}{\Delta t} \quad (3.8)$$

$$A_{nb} = \frac{1}{2} \max(-\dot{F}_v, 0) \quad (3.9)$$

$$S_\alpha = \sum_{nb} \left[ \frac{1}{2} \max(-\dot{F}_v, 0) (\alpha_{nb}^o - \alpha_P^o) - \frac{\gamma(r)}{2} (\phi_A - \phi_D) \dot{F}_v \right] + \frac{\Delta \forall}{\Delta t} \alpha_P^o \quad (3.10)$$

where  $\dot{F}_v = \bar{V}_f \cdot \bar{S}_f$  is the volume flux, the subscript  $P$  denotes the primary node and  $nb$  denotes the neighbor node.

### 3.3 Discretization of the momentum equation

The momentum equations can be expressed by

$$\frac{\partial \rho \phi}{\partial t} + \nabla \cdot (\rho \bar{V} \phi) = \nabla \cdot (\mu \nabla \phi) + Q_\phi \quad (3.11)$$

where  $Q_\phi$  is the source term of momentum equation, and  $\phi$  represents the velocity components. Then, take a volume integral of the above equation and make use of Gauss theorem to yield:

$$\int_V \rho \frac{\partial \phi}{\partial t} d\forall + \oint_S (\rho \bar{V} \phi) \cdot d\bar{S} = \oint_S (\mu \nabla \phi) \cdot d\bar{S} + \int_V Q_\phi d\forall \quad (3.12)$$

#### 3.3.1 Unsteady term

The volume integral of the unsteady term can be discretized as

$$\int_V \frac{\partial \rho \phi}{\partial t} dV \approx \frac{\rho_P^o \Delta V}{\Delta t} (\phi_P^n - \phi_P^o) \quad (3.13)$$

### 3.3.2 Convection term

The surface integral for the convection term can be approximated by

$$\oint_S (\rho \vec{V} \phi) \cdot d\vec{S} \approx \sum_f (\rho \nabla \phi)_f \cdot \vec{S}_f = \sum_f F_f^C = \sum_f \dot{m}_f \phi_f \quad (3.14)$$

where  $\dot{m}_f$  is the mass flux through the considering face.

The convective flux on the considering face can be estimated as a function of neighbor cells by a flux limiter function  $\gamma(r)$ , which will be introduced in the next Chapter.

$$\phi_f = \phi_D + \gamma(r) \left( \frac{\phi_A - \phi_D}{2} \right) \quad (3.15)$$

where the subscript D denotes the donor node and A the acceptor node. In our calculation, the Van Leer scheme will be employed in the momentum equations.

The form of flux limiter function of Van Leer will be described in Chapter 4. The convective fluxes at donor node and acceptor node can be calculated as:

$$\begin{cases} \phi_D = \phi_P, & \phi_A = \phi_{nb} & \text{for } \dot{m}_f > 0 \\ \phi_D = \phi_{nb}, & \phi_A = \phi_P & \text{for } \dot{m}_f < 0 \end{cases} \quad (3.16)$$

where the subscript P denotes the primary node and nb stands for the neighboring node (see Figure 3.1).

### 3.3.3 Diffusion term

The surface integral of the diffusion term is approximated by

$$\oint_S (\mu \nabla \phi) \cdot d\vec{S} \approx \sum_f (\mu^o \nabla \phi)_f \cdot \vec{S}_f = \sum_f F_f^D \quad (3.17)$$

Let,

$$\vec{S}_f = \vec{d} + (\vec{S}_f - \vec{d}) \quad (3.18)$$

where  $\vec{d}$  is a vector pointing in the direction from the primary volume center to the

neighboring volume center (Figure 3.1). The length  $|\vec{d}|$  was considered to be the factor affecting the diffusion dominancy and numerical stability. Hence, the over-relaxed approach for  $\vec{d}$  was introduced

$$\vec{d} = \frac{|\vec{S}_f|^2}{\vec{\delta}_d \cdot \vec{S}_f} \vec{\delta}_d \quad (3.19)$$

The diffusion flux can then be expressed as:

$$F_f^D = \frac{\mu_f^o |\vec{S}_f|^2}{\vec{\delta}_d \cdot \vec{S}_f} (\phi_{nb}^n - \phi_p^n) + \mu_f^o \nabla \phi_f^o \cdot (\vec{S}_f - \vec{d}) \quad (3.20)$$

### 3.3.4 Source term

The volume integral of the diffusion term is approximated by

$$\int_V Q_\phi dV \approx (q_\phi \Delta V)_p \quad (3.21)$$

The source terms in the momentum equation are pressure, gravitational acceleration and surface tension terms. In the following, each term will be introduced.

#### Pressure term

The surface integral of the pressure term is approximated as

$$\oint_S P d\vec{S} = \sum_f P_f^o \vec{S}_f = \nabla P^o \Delta V \quad (3.22)$$

#### Gravitational acceleration term

The gravitational acceleration term can be approximated as

$$\int_V \rho \vec{g} dV = \vec{g} \rho^o \Delta V \quad (3.23)$$

#### Surface tension term

The volume integral of the surface term can be obtained from the approximation

$(\nabla \alpha)_p = \frac{1}{\Delta V} \sum_f \vec{S}_f \alpha_f$ , where  $\alpha_f$  is the face value obtained by the interpolation from the two neighboring nodes. Thus,



$$\begin{aligned}
\int_V \sigma \kappa \nabla \alpha dV &= \sigma \kappa_p (\nabla \alpha)_p \Delta \nabla = -\sigma \left[ \nabla \cdot \left( \frac{\nabla \alpha}{|\nabla \alpha|} \right) \right]_p \frac{1}{\Delta \nabla} \sum_f \bar{S}_f \alpha_f \Delta \nabla \\
&= \frac{-\sigma}{\Delta \nabla} \sum_f \bar{S}_f \cdot \left[ \frac{(\nabla \alpha)_f}{|\nabla \alpha|_f} \right] \sum_f \bar{S}_f \alpha_f
\end{aligned} \tag{3.24}$$

### 3.3.5 Arrangement of the difference transport equation

The discretized form of the momentum equation is approximated by the following form.

$$A_p \phi_p^n = \sum_{nb} A_{nb} \phi_{nb}^n + Q_\phi - \nabla P^o \Delta \nabla \tag{3.25}$$

where

$$\begin{aligned}
A_p &= \sum_{nb} A_{nb} + \rho_p \frac{\Delta \nabla}{\Delta t} \\
A_{nb} &= \frac{\mu_f^o |\bar{S}_f|^2}{\bar{\delta}_d \cdot \bar{S}_f} + \max(-\dot{m}_f, 0)
\end{aligned} \tag{3.26}$$

$$\begin{aligned}
Q_\phi &= \sum_f \left\{ -\dot{m}_f \frac{\gamma(r)}{2} (\phi_A - \phi_D) + \mu_f^o \nabla \phi_f^o (\bar{S}_f - \bar{d}) \right\} \\
&\quad + \rho_p^o \frac{\Delta \nabla}{\Delta t} \phi^o + \bar{g} \rho_p^o \Delta \nabla + \sigma \kappa (\nabla \alpha_p^o) \Delta \nabla
\end{aligned}$$

### 3.4 Pressure-velocity coupling of the PISO algorithm

The method of Pressure-Implicit with Splitting of Operators, which is proposed by Issa [41], is called PISO algorithm. In this study, the PISO algorithm will be used to deal with the unsteady problems. In the following, the procedure of PISO algorithm is addressed.

#### Predictor step

The predictor step is to solve the momentum equation using the prevailing pressure field.

$$A_p \vec{V}_p^* = \sum_{nb} A_{nb} \vec{V}_{nb}^* + (S - \nabla P_p^o \Delta \nabla) \tag{3.27}$$

The above equation solves the velocity field but the mass conservation law has not been satisfied yet. Dividing the above equation by  $A_p$  yields

$$\vec{V}_p^* = \frac{\sum_{nb} A_{nb} \vec{V}_{nb}^*}{A_p} + \frac{S}{A_p} - \left( \frac{\Delta \nabla}{A_p} \right)_p \nabla P_p^o \tag{3.28}$$

Let

$$\bar{H}_P^* = \frac{\sum_{nb} A_{nb} \bar{V}_{nb}^* + S}{A_p} \quad (3.29)$$

Then,  $\bar{V}_P^*$  is written as

$$\bar{V}_P^* = \bar{H}_P^* - \left( \frac{\Delta \nabla}{A_p} \right)_P \nabla P_P^o \quad (3.30)$$

In the equation (3.29), the superscript “—” stands for the value interpolated from the primary cell P and the neighbor cell C with a weighting factor  $w_f$ .

### First corrector step

The corrector steps are taking care of the mass conservation law of the flow field by updating the corresponding pressure. The new velocities and the corresponding new pressure assumed to be obtained from the first corrector step are denoted with superscript \*\* and \*.

$$A_p \bar{V}_P^{**} = \sum_{nb} A_{nb} \bar{V}_{nb}^* + (S - \nabla P_P^* \Delta \nabla) \quad (3.31)$$

Dividing the above equation by  $A_p$  and using the definition of (3.29)

$$\bar{V}_P^{**} = \frac{\sum_{nb} A_{nb} \bar{V}_{nb}^*}{A_p} + \frac{S}{A_p} - \left( \frac{\Delta \nabla}{A_p} \right)_P \nabla P_P^* = \bar{H}_P^* - \left( \frac{\Delta \nabla}{A_p} \right)_P \nabla P_P^* \quad (3.32)$$

The first velocity correction equation ( $\bar{V}'_P$ ) is obtained by  $V' \equiv V^{**} - V^*$ ,  $P' \equiv P^* - P^o$ , and shown as

$$\bar{V}'_P = - \left( \frac{\Delta \nabla}{A_p} \right)_P \nabla P'_P \quad (3.33)$$

At the cell face, the velocity correction equation can be obtained in a similar manner.

$$\bar{V}'_f = - \left( \frac{\Delta \nabla}{A_p} \right)_f \nabla P'_f \quad (3.34)$$

Therefore, the volume flux correction equation is obtained as

$$\dot{V}'_f = \vec{V}'_f \cdot \vec{S}_f = \left[ - \left( \frac{\Delta \nabla}{A_P} \right)_f \nabla P'_f \right] \cdot \vec{S}_f \quad (3.35)$$

Over-relaxed approach is employed to let  $\vec{S}_f = \vec{d} + (\vec{S}_f - \vec{d})$  for better numerical diffusion control.

$$\dot{V}'_f = - \left[ \left( \frac{\Delta \nabla}{A_P} \right)_f \frac{|\vec{S}_f|^2}{\vec{\delta}_{Pnb} \cdot \vec{S}_f} (\nabla P'_f \cdot \vec{\delta}_{Pnb}) + \left( \frac{\Delta \nabla}{A_P} \right)_f \nabla P'_f \cdot (\vec{S}_f - \vec{d}) \right] \quad (3.36)$$

where  $\vec{d} = \frac{|\vec{S}_f|^2}{\vec{\delta}_{nb} \cdot \vec{S}_f} \vec{\delta}_{nb}$

Then, replacing the term  $\nabla P'_f \cdot \vec{\delta}_{Pnb}$  by  $P'_{nb} - P'_p$  yields

$$\dot{V}'_f = - \left[ \left( \frac{\Delta \nabla}{A_P} \right)_f \frac{|\vec{S}_f|^2}{\vec{\delta}_{Pnb} \cdot \vec{S}_f} (P'_{nb} - P'_p) + \left( \frac{\Delta \nabla}{A_P} \right)_f \nabla P'_f \cdot (\vec{S}_f - \vec{d}) \right] \quad (3.37)$$

The first volume flux correction equation can be presented as

$$\dot{V}^{**}_f = \dot{V}'_f - \left[ \left( \frac{\Delta \nabla}{A_P} \right)_f \frac{|\vec{S}_f|^2}{\vec{\delta}_{Pnb} \cdot \vec{S}_f} (P'_{nb} - P'_p) + \left( \frac{\Delta \nabla}{A_P} \right)_f \nabla P'_f \cdot (\vec{S}_f - \vec{d}) \right] \quad (3.38)$$

The volume flux at the face ( $\dot{V}^*_f$ ) of the above equation can be obtained by the following.

The relationship between velocity and the pressure at the face can be written as the form of (3.30) similarly.

$$\vec{V}^*_f = \vec{H}^*_f - \left( \frac{\Delta \nabla}{A_P} \right)_f \nabla P^o_f \quad (3.39)$$

where

$$\vec{H}^*_f = \vec{V}^*_f + \left( \frac{\Delta \nabla}{A_P} \right)_f \nabla P^o_f \quad (3.40)$$

$\vec{V}^*_f$  and  $\nabla P^o_f$  are written by a weighting factor  $w_f$  and shown as

$$\nabla P^o_f = w_f \nabla P^o_{nb} + (1 - w_f) \nabla P^o_p \quad (3.41)$$

$$\overline{\vec{V}}_f = w_f \vec{V}_{nb}^* + (1 - w_f) \overline{\vec{V}}_P^* \quad (3.42)$$

Substituting equation (3.40) into equation (3.39) to obtain:

$$\vec{V}_f^* = \left[ \overline{\vec{V}}_f^* + \left( \frac{\Delta \nabla}{A_P} \right)_f \overline{\nabla P}_f \right] - \left( \frac{\Delta \nabla}{A_P} \right)_f \nabla P_f^o \quad (3.43)$$

where  $\left( \frac{\Delta \nabla}{A_P} \right)_f$  is an average value of primary cell and neighbor cell.

$$\left( \frac{\Delta \nabla}{A_P} \right)_f = \frac{1}{2} \left[ \left( \frac{\Delta \nabla}{A_P} \right)_P + \left( \frac{\Delta \nabla}{A_P} \right)_{nb} \right] \quad (3.44)$$

Then, the volume flux at the face ( $\dot{V}_f^*$ ) can be obtained.

$$\begin{aligned} \dot{V}_f^* &= \vec{V}_f^* \cdot \vec{S}_f = \overline{\vec{V}}_f^* \cdot \vec{S}_f - \left( \frac{\Delta \nabla}{A_P} \right)_f (\nabla P_f^* - \overline{\nabla P}_f^o) \cdot \vec{S}_f \\ &\approx \overline{\vec{V}}_f^* \cdot \vec{S}_f - \left( \frac{\Delta \nabla}{A_P} \right)_f (\nabla P_f^* - \overline{\nabla P}_f^o) \cdot \vec{d} \end{aligned} \quad (3.45)$$

The continuity equation is discretized as

$$\sum_f \dot{V}_f^{**} = \sum_f \dot{V}_f^* + \sum_f \dot{V}'_f = 0 \quad (3.46)$$

The pressure correction equation is obtained by substituting (3.38) into (3.46).

$$A_P^P P'_P = \sum_f A_{nb}^P P'_{nb} - \sum_f \dot{V}_f^* + S_{P1} + S_{P2} \quad (3.47)$$

where

$$\begin{aligned} A_P^P &= \sum_f A_{nb}^P \\ A_{nb}^P &= \left( \frac{\Delta \nabla}{A_P} \right)_f \frac{|\vec{S}_f|^2}{\vec{\delta}_{nb} \cdot \vec{S}_f} \\ S_{P1} &= -\sum_f \dot{V}_f^* \\ S_{P2} &= \sum_f \left( \frac{\Delta \nabla}{A_P} \right)_f \nabla P_f^* \cdot (\vec{S}_f - \vec{d}) \end{aligned}$$

## Second corrector step

To enhance the SIMPLE procedure PISO performs a second corrector step. Similarly, the momentum equation is taken as

$$A_P \vec{V}_P^{***} = \sum_{nb} A_{nb} \vec{V}_{nb}^{**} + (S - \nabla P_P^{**} \Delta \nabla) \quad (3.48)$$

where the new velocities and the corresponding new pressure are denoted with superscript \*\*\* and \*\*.

Similarly, the second velocity corrector can be deduced as

$$\vec{V}_P'' = \left( \frac{\sum_f A_{nb} \vec{V}'_{nb}}{A_P} \right)_f - \left( \frac{\Delta \nabla}{A_P} \right)_f \nabla P_f'' \quad (3.49)$$

where  $V'' \equiv V^{***} - V^{**}$ ,  $V' \equiv V^{**} - V^*$ ,  $P'' \equiv P^{**} - P^*$

Again, the volume flow rate corrector is

$$\dot{V}_f'' = \left[ \left( \frac{\sum_f A_{nb} \vec{V}'_{nb}}{A_P} \right)_f - \left( \frac{\Delta \nabla}{A_P} \right)_f \nabla P_f'' \right] \cdot \vec{S}_f \quad (3.50)$$

The second corrector step is

$$A_P^P P'_P = \sum_f A_{nb}^P P'_{nb} + S_{P1}^2 + S_{P2}^2 \quad (3.51)$$

where

$$\begin{aligned} A_P^P &= \sum_f A_{nb}^P \\ A_{nb}^P &= \left( \frac{\Delta \nabla}{A_P} \right)_f \frac{|\vec{S}_f|^2}{\vec{\delta}_{Pnb} \cdot \vec{S}_f} \\ S_{P1}^2 &= - \left( \frac{\sum_f A_{nb} \vec{V}'_{nb}}{A_P} \right)_f \cdot \vec{S}_f \\ S_{P2}^2 &= \sum_f \left( \frac{\Delta \nabla}{A_P} \right)_f \nabla P_f'' \cdot (\vec{S}_f - \vec{d}) \end{aligned} \quad (3.52)$$

Although more corrector steps are needed completed satisfy for the conservation law, two corrector steps are sufficient to have the accuracy of solution within temporal truncation error.



### **Solution procedure of PISO**

- Step 1.** read the velocities and pressure of the flow field from the old time level.
- Step 2.** solve the momentum equation (3.27) to get  $V^*$
- Step 3.** compute  $P'$  by solving the first pressure correction equation (3.47) to update velocities and pressure to get  $V^{**}$  and  $P^*$ .
- Step 4.** compute  $P''$  by solving the second pressure correction equation (3.51) to further update velocities and pressure to get  $V^{***}$  and  $P^{**}$ .
- Step 5.** if the required time step is achieved, then stop the calculation and output the data otherwise proceed to the next time step and repeat all over the way from step 1 to step 4.

### **3.5 Solution procedure**

The VOF equation and momentum equation have been discretized. In this section, the solution procedure of two-fluid flow system will be described.

1. Initialize all variables at initial time  $t_0$
2. Solve the VOF equation for volume fraction  $\alpha$  by using the old time volumetric fluxes.
3. Update the coefficients of the momentum equations. Use the new  $\alpha$  values to obtain an estimate for new viscosity and density.
4. Solve the momentum equation and continue with PISO algorithm.
5. If the final time step has not been reached, advance to the next time step and return to step 2.

## Chapter4 High Resolution Differencing Schemes

### 4.1 Introduction

As mentioned above, an effective scheme adopted to solve the two-phase flow must have some features, such as small diffusion, boundedness, and maintenance of sharp interface. The schemes which are introduced in the first chapter can not include above features at the same time. For example, the first-order upwind difference scheme is bounded but too diffusive. The problem which results from numerical diffusion is very important in the two-fluid system with the interface between two fluids. The strong numerical diffusion will smear the characteristic of the step function on the interface. In this chapter, the linear and non-linear scheme will be presented, and a composite scheme with switching function which can maintain the sharpness and shape of the interface will be proposed.

### 4.2 Convective flux of volume fraction

As mentioned above, the discretization of the VOF equation has been established. In the calculation process, the value on the considering face of a cell must be approximated. The approximation of the face value is necessary to ensure the accuracy and stable. The face value  $\alpha_f$  can be estimation about a function of neighbor cells. Only two neighbor cells should be considered in the unstructured grid system. Figure 4.1 shows a control volume and its neighbor cells including the upwind and acceptor. The subscript U, D and A denote upwind cell, donor cell and acceptor cell.

In general, the methods, such as the upwind difference scheme (4.1) and the central difference scheme (4.2), are adopted to approximate this value.

$$\alpha_f = \alpha_D \quad (4.1)$$

$$\alpha_f = \frac{1}{2}(\alpha_A + \alpha_D) \quad (4.2)$$

where  $\alpha_f$  is the value of volume fraction on the face,  $\alpha_D$  the value of volume fraction of the donor cell, and  $\alpha_A$  the value of volume fraction of the acceptor cell.



These two schemes can be associated by the variable of  $\gamma$  shown as:

$$\alpha_f = \alpha_D + \frac{\gamma}{2}(\alpha_A - \alpha_D) \quad (4.3)$$

The term which has  $\gamma$  in the equation (4.3) is called the anti-diffusion correction to the upwind differencing. When  $\gamma=1$ , the equation (4.3) becomes central difference scheme. Then, this approximation will result in oscillations in the regions where the gradients are large. Because of the above, the variable  $\gamma$  must be limited. The schemes with limitation will present high accuracy and resolution results which guarantee boundedness. The schemes with total variation diminishing (TVD) flux limiters were proposed in [23] in order to ensure the bounded solution. These schemes are implemented in the context of the normalized variables formulation (NVF) [24] for the development of normalized variables diagram (NVD) schemes originally. The limiter  $\gamma$  is defined as a function of the gradient  $r$  [26], shown as:

$$r = \frac{\alpha_D - \alpha_U}{\alpha_A - \alpha_D} \quad (4.4)$$

where  $\alpha_U$  is the value of volume fraction of the upwind cell.

The value of  $\alpha$  can be normalized as [24]:

$$\tilde{\alpha} = \frac{\alpha - \alpha_U}{\alpha_A - \alpha_U} \quad (4.5)$$

with the normalization, we can get following equations:

$$\begin{aligned} \tilde{\alpha}_D &= \frac{\alpha_D - \alpha_U}{\alpha_A - \alpha_U} \\ \tilde{\alpha}_f &= \frac{\alpha_f - \alpha_U}{\alpha_A - \alpha_U} \\ \tilde{\alpha}_U &= 0 \\ \tilde{\alpha}_A &= 1 \end{aligned} \quad (4.6)$$

Introduce this normalized variable into equation (4.3), and it can be rewritten as following equation, and  $\tilde{\alpha}_f$  is just the function of  $\tilde{\alpha}_D$ .

$$\tilde{\alpha}_f = \tilde{\alpha}_D + \gamma(r) \left( \frac{1 - \tilde{\alpha}_D}{2} \right) \quad (4.7)$$

where  $r = \frac{\tilde{\alpha}_D}{1 - \tilde{\alpha}_D}$

### 4.3 CBC and TVD constraints

In order to ensure a bounded value, the high resolution schemes (HRs) [23] must satisfy the Convective Boundedness Criterion (CBC) or total variation diminishing (TVD) condition. The high resolution schemes will prevent the oscillation or wiggles and get more accurate results around shocks and discontinuities in the two-fluid flow simulation. The Convective Boundedness Criterion (CBC) which was proposed by Gaskell and Lau [27] can be shown in the NVD (Fig 4.2):

$$\begin{cases} \tilde{\alpha}_f = \tilde{\alpha}_D & \text{for } \tilde{\alpha}_D < 0 \text{ or } \tilde{\alpha}_D > 1 \\ \tilde{\alpha}_D \leq \tilde{\alpha}_f \leq 1 & \text{for } 0 \leq \tilde{\alpha}_D \leq 1 \end{cases} \quad (4.8)$$

Sweby [26] has proposed another constraint which makes the scheme satisfy the TVD condition and it can be shown as:

$$0 \leq \left( \frac{\gamma_f(r)}{r}, \gamma_f(r) \right) \leq 2 \quad (4.9)$$

The above constraints can be illustrated from Fig. 4.2 to Fig. 4.4. Fig. 4.2 and Fig 4.3 present the comparison with TVD constraint and the CBC constraint in the NVD. TVD constraint in the TVD diagram is showed in Fig. 4.4, and the hatched region is known as the second-order regime.

### 4.4 Linear and non-linear schemes

In this section, several high order schemes will be introduced. Generally speaking, these schemes can be divided into linear and non-linear schemes. First, linear schemes are built and can be explained by using of the combination of UDS and an anti-diffusion term or by the flux limiter function  $\gamma(r)$ . The normalized variable and the flux limiter function of the linear schemes can be found in table 4.1. Furthermore, these schemes will be plotted in the normalized variables diagram (NVD) and total variation diminishing (TVD) diagram (see Fig.

4.5 and 4.6).

UDS and DDS are both the first-order schemes. UDS (Upwind Difference Scheme) is an unconditional stable scheme and provides a stable solution at any time. However, this scheme always causes too much numerical diffusion which decreases the accuracy of the simulation. DDS (Downwind Difference Scheme) results in less numerical diffusion result but unbounded. The other schemes, such as CDS (Central Difference Scheme), LUS (Linear Upwind Scheme) and Fromm scheme, are two-order accuracy schemes. The schemes, including QUICK (Quadratic Upwind Interpolation for Convective Kinematics) and CUS (Cubic Upwind Scheme), have higher-order accuracy than above schemes. In the figure 4.5 and 4.6, the lines of second- and third- order schemes pass by the point (0.5, 0.75) in the NVD and the point (1, 1) in the TVD diagram. These linear schemes except the upwind difference scheme are not satisfied Convective Boundedness Criterion (CBC). High resolution schemes are developed by changing the high-order schemes into a non-linear one which satisfy the CBC. These non-linear schemes can be divided two categories. SMART and STOIC schemes are referred to NVD scheme, and MUSCL, SUPERBEE, OSHER and Van Leer schemes can be referred to TVD scheme. In present paper, two modified NVD schemes called M-MUSCL (Modified MUSCL) and M-BDS (Modified Bounded Downwind Scheme) will be developed to simulate the indicator function of the volume fraction. The normalized variable and the flux limiter function of these non-linear schemes can be summarized in table 4.1, and Fig. 4.7 to 4.16 show the NVD and TVD diagrams of these non-linear schemes.

#### **4.5 Composite scheme with switching function**

Solving the face value of the volume fraction by using only one high resolution scheme can not give consideration to both less numerical diffusion and non-deformed interface. The high resolution schemes preserve the shape of the interface but can not reduce the numerical diffusion. The compressive schemes are able to reach less numerical diffusion but let the interface deformed. Most composite schemes switch the compressive scheme and high

resolution scheme with a switching function about the slope of the interface in order to overcome the above problem. The method about composite scheme has been used in the former investigations. The key issue is how to switch schemes not when. The switching function has the basic on the angle between interface and direction of motion. It will decide which kind of the scheme to calculate the normalized face value of the volume fraction. If the interface is perpendicular to the cell face, a high resolution scheme would be appropriate. If the interface is parallel to the cell face, a compressive scheme would be appropriate. In general, the angle between the interface and control volume face is between these two cases. The normalized face value can be written as:

$$\tilde{\alpha}_f = \tilde{\alpha}_{f(\text{compressive})} \psi(\theta_f) + \tilde{\alpha}_{f(HR)} (1 - \psi(\theta_f)) \quad (4.10)$$

where  $\psi(\theta_f)$  is the switching function between zero and unity, and

$$\theta_f = \cos^{-1} \left| \frac{\nabla \alpha_f \cdot \vec{d}}{\|\nabla \alpha_f\| \|\vec{d}\|} \right|, \quad 0^\circ \leq \theta_f \leq 180^\circ \quad (4.11)$$

The well known composite schemes, such as HRIC of Muzaferija [33] and CICSAM of Ubbink [35] will be introduced. The composite of modified MUSCL and modified BDS will be also developed in this section.

### CICSAM

In order to reduce the numerical diffusion and keep the sharpness of the interface, the compressive scheme called Hyper-C has been proposed by Leonard [42]. In general, the most compressive scheme is very suitable to the two-fluid flow with moving interface, but the Hyper-C may sometimes make the interface deformed or wrinkled. Therefore, Ubbink uses the ULTIMATE-QUICKEST (UQ) scheme to preserve the shape of the interface. The UQ (4.12) and Hyper-C (4.13) scheme (Fig. 4.17) can be shown as:

$$\tilde{\alpha}_f = \begin{cases} \tilde{\alpha}_D, & \tilde{\alpha}_D \geq 1 \text{ or } \tilde{\alpha}_D \leq 0 \\ \min \left\{ \frac{8Co\tilde{\alpha}_D + (1-Co)(6\tilde{\alpha}_D + 3)}{8}, \min \left\{ 1, \frac{\tilde{\alpha}_D}{Co} \right\} \right\}, & 1 > \tilde{\alpha}_D > 0 \end{cases} \quad (4.12)$$

$$\tilde{\alpha}_f = \begin{cases} \tilde{\alpha}_D, & \tilde{\alpha}_D \geq 1 \text{ or } \tilde{\alpha}_D \leq 0 \\ \min \left( 1, \frac{\tilde{\alpha}_D}{Co} \right), & 0 < \tilde{\alpha}_D < 1 \end{cases} \quad (4.13)$$

The Compressive Interface Capturing Scheme for Arbitrary Meshes (CICSAM) scheme is developed by using the composite of the Hyper-C and UQ scheme with switching function  $\psi(\theta_f)$  (Fig. 4.18) given as:

$$\psi(\theta_f) = \min \left[ \frac{\cos(2\theta_f) + 1}{2}, 1 \right] \quad (4.14)$$

Then, the CICSAM scheme can be written as:

$$\tilde{\alpha}_{f(CICSAM)} = \tilde{\alpha}_{f(HYPER-C)}\psi(\theta_f) + \tilde{\alpha}_{f(UQ)}(1 - \psi(\theta_f)) \quad (4.15)$$

where the switching function  $f(\theta_f)$  is shown as (4.14).

## HRIC

This composite scheme, like the above method, switches the upwind difference scheme and bounded downwind scheme with the switching function (Fig. 4.19) shown as

$$\psi(\theta_f) = \sqrt{|\cos(\theta_f)|} \quad (4.16)$$

Then, the HRIC scheme can be shown as:

$$\tilde{\alpha}_{f(HRIC)} = \begin{cases} \tilde{\alpha}_{f(BDS)}\psi(\theta_f) + \tilde{\alpha}_{f(UDS)}(1 - \psi(\theta_f)), & Co < 0.3 \\ \left\{ \begin{aligned} & \tilde{\alpha}_{f(BDS)}\psi(\theta_f) + \tilde{\alpha}_{f(UDS)}(1 - \psi(\theta_f)) + \\ & \left[ \tilde{\alpha}_{f(BDS)}\psi(\theta_f) + \tilde{\alpha}_{f(UDS)}(1 - \psi(\theta_f)) - \tilde{\alpha}_{f(UDS)} \right] \frac{0.7 - Co}{0.7 - 0.3} \end{aligned} \right\}, & 0.3 < Co < 0.7 \\ \tilde{\alpha}_{f(UDS)}, & Co > 0.7 \end{cases} \quad (4.17)$$

## Composite of modified MUSCL and modified BDS

In present paper, the development of a new composite scheme switches the modified MUSCL and modified BDS scheme posed in the above chapter with the switching function (Fig. 4.20) given as:

$$f(\theta_f) = [\cos^4(\theta_f)] \quad (4.18)$$

This switching function has been proposed in [34], and this method can be formulated as:

$$\tilde{\alpha}_f = \tilde{\alpha}_{f(M-BDS)}\psi(\theta_f) + \tilde{\alpha}_{f(M-MUSCL)}(1 - \psi(\theta_f)) \quad (4.19)$$

The composite scheme of modified MUSCL and modified BDS will be used to simulate cases in our investigation.



## Chapter5 Results and Discussion

### 5.1 Introduction

The method of high resolution schemes in volume-of-fluid method for two-fluid flow has been developed in the previous chapter. In this chapter, four cases will be tested, and the accuracy of this method will be presented by the comparison between the numerical and theoretical solutions.

### 5.2 Uniform density flow

In this section, the test case focuses on the advection of interfaces of different shapes. We will demonstrate the accuracy of high resolution schemes in the volume-of-fluid method by placing two different hollow scalar fields in a uniform and oblique velocity field. The initial distributions of the two scalar fields are a hollow square, which coincides with the coordinate axes, and a hollow circle. The side lengths of outer and inner interfaces of the hollow square are 0.8 and 0.4. The maximum and minimum diameters of the hollow circle are 0.8 and 0.4. The velocity field  $(u,v)=(2,1)$  (Fig. 5.1) is constant in the full computation domain which is a  $4 \times 4$  square. The centers of these two scalar fields are at  $(0.8,0.8)$  initially and they propagate to  $(2.8,1.8)$  after one second. The uniform and quadrilateral mesh with  $100 \times 100$  grids and triangular mesh with 22478 cells (Fig. 5.2) will be used in the calculation process. The time step is chosen to maintain a maximum mesh Courant number of 0.25 and 0.75.

For the purpose of comparison the solution error between the exact and numerical solution can be given as [32]:

$$E = \frac{\sum_{i=1}^{all \ cell} |\alpha_i^n \Delta \nabla_i - \alpha_i^a \Delta \nabla_i|}{\sum_{i=1}^{all \ cell} \alpha_i^o \Delta \nabla_u} \quad (5.1)$$

where  $\alpha^n$  is the calculated solution after n time steps,  $\alpha^a$  the exact solution, and  $\alpha^o$  the initial condition. The exact solution of this case should be advected with no changing of the shape and it shown in figure 5.3.

From the figure 5.4 to 5.7, the final shapes of these two hollow scalar fields by

calculating the indicator function with different high resolution schemes are presented. Contours display the distribution of the value of volume fraction from 0.05 to 0.95 with 10 levels. The errors are summarized from table 5.1 to 5.4.

The results of  $Co = 0.75$  is more diffusive than  $Co = 0.25$ , and the numerical diffusion causes the interface of hollow shapes smearing. The upwind difference scheme can not be used to simulate because it is too diffusive. Although bounded downwind and downwind difference schemes can get higher compressive results, the interface is broken in high Courant number. The modified bounded downwind scheme which is a high compressive scheme can maintain the sharpness of the interface and the error is less than other schemes. It will be an efficient scheme to simulate two-fluid flow in the low Courant number, but the interface may be deformed in the high Courant number. The composite scheme with switching function will be adopted to solve the above problem.

The results of composite schemes used to solve this case will be presented from Fig 5.8 to 5.11. The errors are shown from table 5.5 to 5.8. The CICSAM scheme can retain the sharp interface with less numerical diffusion in low Courant, but the result in high Courant number losses the accuracy due to the numerical diffusion. The HRIC scheme may reach the small error, but the shape of interface will be deformed. The composite of MUSCL and SUPERBEE get the nice shape of the interface in any Courant number, but the interface can not maintain its sharpness. Therefore, the composite of modified BDS and modified MUSCL will be adopted in our simulation. This scheme can get the smallest error, maintain the sharpness of interface and keep the shape of the interface.



### 5.3 Shear flow

The problem about maintaining the initial shape in the two-fluid flow will become rather complex when the deformation of the interface is considered. There is a shear velocity field in the real two-fluid flow. Therefore, we must test our numerical method in the shear flow. In this section, a velocity field shown as (5.2) will be used to simulate this situation in a  $\pi \times \pi$  computational domain [32]. Two different meshes will be employed in calculations. One is the uniform and quadrilateral mesh with  $100 \times 100$  grids. The other is the triangular mesh with 22494 cells (Fig. 5.13).

$$\vec{V} = \sin x \cos y \vec{i} + \cos x \sin y \vec{j} \quad (5.2)$$

Fig 5.12 shows that a shear velocity is enforced on a circle distribution of volume fraction. The initial position of the circle is  $(0.5\pi, 0.2(1+\pi))$  with a radius of  $0.2\pi$ . The circular scalar field will be convected by the above velocity field for 2, 4, 8 and 16 seconds, and then the velocity field is reversed for the same time. Theoretically, the circular volume fraction distribution will not be deformed in the above calculation process. Errors of the solution can be defined as (5.1) and are discussed in the situation that Courant number equals 0.25 and 0.75. The results, which solve the VOF equation with HRIC, CICSAM, the composite of MUSCL and SUPERBEE, and the composite of modified BDS and modified MUSCL schemes, before reversing and at the end of calculation show in Fig 5.14 to 5.29. Solution errors of above schemes together with results from [43] are presented in Fig. 5.30 to 5.33.

In the shear flow, CICSAM scheme is a more accurate one on the quadrilateral mesh when the Courant number equals to 0.25, but it can not be simulated in high Courant number due to large errors. HRIC scheme maintains the sharpness of the interfaces by the high compression. This will cause the shape of interface deformed significantly. The composite of MUSCL and SUPERBEE scheme results in too much numerical diffusion which smears the interface and can not present a sharp interface. Therefore, the composite of modified MUSCL

and modified MUCSL can present the best results of these methods, even on triangular meshes. It can be used in high and low Courant number and reach less errors. In following cases, we will use this scheme to simulate the broken dame and filling process in an open tank and compare with other schemes.



## 5.4 Broken dam

The broken dam case is usually used to demonstrate the accuracy of the numerical model in the two-fluid flow because the initial flow distribution is very simple. In our thesis, this case will be used to test our numerical model and the composite scheme called the composite of modified MUSCL and modified BDS scheme. Many numerical models about broken dam have been proposed in many literatures. Some experiment data of the broken dam have been presented by Martin and Moyce [44]. In order to measure the speed of the leading edge and the reduction of the column height, one accurate experiment has been posed by Koshizuka [45]. In the experiment, the tank is a space with a base length of 0.584m. The water column with the height of 0.292m and the base length of 0.146m is confined between a vertical wall and the gate (shown in Fig. 34). The gate is suddenly remove at  $t=0$ . The water column starts to collapse and moves to the right wall. When the leading edge hits the right wall, the flow starts to fall back due to the gravity. The experimental result of [45] is shown in Fig. 5.18.

Our computational domain is a rectangle with a base length of 0.584m and a height of 0.340m. Three kinds of meshes are employed in our calculation. The first is the uniform and quadrilateral mesh with  $48 \times 28$  and  $120 \times 70$  grids. The second is the non-uniform and quadrilateral mesh with  $56 \times 36$  grids (Fig. 36). The third is the triangular mesh with 4506 and 12354 cells (Fig. 37 and Fig. 38). Non-slip boundary conditions are applied to the bottom and sides of the tank. The top boundary is set as a fixed pressure outlet. For the fluid 1, the density is 1000 and the viscosity is 0.001. For the fluid 2, the density is 1 and the viscosity is 0.00001. The two-dimensional section with interface profile, the volume fraction contour and the velocity field is shown in Fig. 5.39 to 5.43. The dimensionless positions of leading edge and reduction of column height are plotted as functions of the dimensionless times in Fig. 5.44 and Fig. 5.45, and compared with the experiment. The numerical diffusion will occur when the flow returns. The numerical diffusion causes the front of wave smearing. The phenomena of  $48 \times 28$  mesh is more serious than  $120 \times 70$  mesh. In general, the broken

case solved by our scheme on the quadrilateral or triangular mesh can present a result which maintains the sharp interface. In the Fig. 5.44, the speed of the leading edge in fine mesh is faster than coarse mesh. However, the situation is not very obvious. In Fig. 5.45, the results are quite close to the experiment data and the simulation of CICSAM of Ubbink.



## 5.5 Filling process in an open tank

A filling process in an open tank will be simulated by the composite of modified MUSCL and modified BDS scheme in this section. The tank is a square and vertical plate with a gate at the bottom. Initially, the tank is filled with air (Fig. 46). The water enters the tank through the gate and fills the tank as the time pass by.

The computational domain of the tank in our simulation is a square space with side length of 0.152m. The height of the gate is 0.038m. The flow is considered to be two-dimensional with the assumption of a laminar and incompressible flow under the body and surface tension force. The properties of the fluids are shown as:

$$\begin{aligned}
 \rho_w &= 998 \text{ kg/m}^3 & \rho_a &= 1.205 \text{ kg/m}^3 \\
 \mu_w &= 0.99 \times 10^{-3} \text{ kg/ms} & \mu_a &= 1.81 \times 10^{-5} \text{ kg/ms} \\
 \sigma &= 0.072 \text{ nt/m} \\
 g &= 9.808 \text{ m/s}^2
 \end{aligned} \tag{5.3}$$

The inlet velocity of the gate is given by some approximation from [46]. The volume of the water inside the tank can be evaluated from the photographs by using the curve fitting method. The volume inside the tank can be written as a function depended on time, shown as:

$$\begin{aligned}
 Q(t) &= at + bt^2 \\
 \text{where } a &= 3.207 \times 10^{-2}, \quad b = -6.678 \times 10^{-3}
 \end{aligned} \tag{5.4}$$

which implies:

$$\frac{dQ(t)}{dt} = U_{in}(t) \times A \tag{5.5}$$

and

$$U_{in}(t) = 0.844 - 0.351t \tag{5.6}$$

where A can be considered as the height of the gate in two-dimension, Q is the volume inside the tank, t is the calculational time, and  $U_{in}$  is the inlet velocity depended on t.

The boundary conditions of walls are treated as non-slip condition and the top of the tank is a pressure fixed outlet. The meshes used in the calculation involve the uniform and

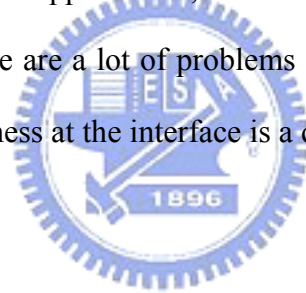
quadrilateral mesh with  $28 \times 28$ ,  $40 \times 40$  and  $80 \times 80$  grids and the triangular mesh with 902, 2024 and 3584 cells (Fig. 47, Fig. 48 and Fig. 49).

Fig 5.50 to 5.55 shows the volume fraction distribution with time evolution. The counter is 0.05 to 0.95 with 10 levels. The results show that the flow with the particular velocity enters the tank as a wall jet along the bottom. When the front of the flow touches the right wall, the high pressure gradient will be introduced into the vicinity of stagnation point. This effect will make the flow jump along the vertical wall. To continue, the flow falls back and forms a gravity wave in the x-direction. The front of flow goes to the left wall along the x-axis and jumps again when the front touches the vertical wall. The tank will be filled by degrees. The volume fraction distribution in the  $28 \times 28$  and  $40 \times 40$  mesh produces more numerical diffusions on the interface. The interface in the  $80 \times 80$  mesh is sharper than them. It shows that the finer mesh can present well results for the filling process of two-fluid flow. The results also show that our code can do well on the triangular mesh. The position of the leading edge at the bottom on the quadrilateral and triangular mesh is plotted in Fig 56.

Then, the figure 5.57 shows the water volume inside the tank. It presents the data in quadrilateral and triangular meshes from our simulation and the data from the inlet condition which is mentioned in (5.6). This figure can demonstrate the accuracy of our numerical method which is applied in the filling process in an open tank and show that our numerical result is very close to the data in [46].

## Chapter6 Conclusion and Future Work

A method for capturing the interface of two-fluid flow has been present. The interface movement is solved by an indicator function of the volume fraction. The composite scheme is used to solve the advection equation of the volume fraction. The aim of this study is to develop a composite scheme with switching function in volume-of-fluid method for two-fluid flow. The scheme switches smoothly between the modified MUSCL and modified bounded downwind scheme. Its results of test cases have compared with the results of other schemes. It can not only maintain the sharpness at the interface but also enhances the accuracy, even on the triangular mesh. In the future work, there are two missions in order to improve our numerical method. First, the volume-of-fluid method is usually used in three-dimension system because many actual applications, such as casting process, are applied in three-dimensions. Second, there are a lot of problems about the heat transfer in the two-fluid flow. How to remain the sharpness at the interface is a quite significant problem.



## Chapter7 Reference

- [1] Azcueta, R., Hadzic, I., Muzaferija, S. and Peric, M., “Computation of flows with free surface”, MARNET-CFD First Workshop – Barcelona, 1999.
- [2] Pericleous, K. A., Chan, K. S. and Cross, M., “Free surface flow and heat transfer in cavities: the SEA algorithm”, Numerical Heat Transfer, Part B, v27, pp.487-507, 1995.
- [3] Yang, Z., Peng, X. F. and Ye, P., “Numerical and experiment investigation of two phase flow during boiling in coiled tube”, Int. J. of Heat and Mass transfer, v51, pp.1003-1016, 2008.
- [4] Wang, Y., Basu, S. and Wang, C. Y., “Modeling two-phase flow in PEM fuel cell channels”, J. of Power Source, v179, pp.603-617, 2008.
- [5] Muzaferija, S. and Peric, M., “Nonlinear water waves interaction, computational mechanics publications”, in: Mahrenholtz O. and Markiewicz M. (Eds.), Computation of free surface flows using interface tracking and interface capturing methods. Chap.2, 1998.
- [6] Floryan, J. M. and Rasmussen, H., “Numerical methods for viscous flows with moving boundaries”, Appl. Mech. Rev., v42, pp.323-341, 1989.
- [7] Hayes, R. E., “Numerical Simulation of Mold Filling in Reaction Injection Molding”, Polym. Eng. Sci., v31, pp.842-848, 1991.
- [8] Muzaferija, S. and Peric, M., “Computation of free-surface flows using the finite-volume method and moving grids”, Numerical Heat Transfer, Part B, v32, pp. 369-384, 1997.
- [9] Tryggvasson, G., “A front tracking method for the computations of multiphase flow”, J. Comput. Phys., v169, pp.708–759, 2001.
- [10] Osher, S. and Sethian, J. A., “Fronts propagating with curvature-dependent speed: algorithms based on Hamilton Jacobi formulations”, J. Comput. Phys., v79, pp.12–49, 1988.
- [11] Li, X.L., “Study of three-dimensional Rayleigh-Taylor instability compressible fluids through level set method and parallel computation”, Phys. Fluids A, v5, pp.1904-1913, 1993.
- [12] Harlow, F. H. and Welch, J. E., “Numerical calculation of time-dependent viscous incompressible flow of fluid with free surface”, Phys. Fluids, v8, No.12, pp. 2182-2189, 1965.
- [13] Patel, N. R. and Briggs, D. G., “Mac Scheme In Bound Ary-Fitted Curvilinear Coordinates”, Numerical Heat Transfer, v6, n4, , pp.383-394, Oct-Dec, 1983.
- [14] Chen, S., Juhnson, D. B. and Radd, P. E., “Velocity boundary conditions for the simulation of free surface fluid flow”, J. Comput. Phys., v116, n2, pp. 262-276, 1995.
- [15] Noh, W. F. and Woodward, P. R., “SLIC (Simple Line Interface Method)”, Lecture Note in Physics, v59, pp. 330-340, 1976.
- [16] Chorin, A. P., “Flame advection and propagation algorithms”, J. Comput. Phys., v35, pp.1-11, 1980.
- [17] Youngs, D. L. “Time-dependent multi-material flow with large fluid Distortion”, in: K.W. Morton, M.J. Baines (Eds.), Numerical Methods for Fluid Dynamics, Academic Press,



New York, pp. 273–285, 1982.

[18] Ramshaw, J. D. and Trapp, J.A., “A numerical technique for low-speed homogeneous two-phase flow with sharp interfaces”, J. Comput. Phys., v21, pp.438-453, 1976.

[19] Hirt, C. W. and Nichols, B. D., “Volume of fluid (VOF) method for the dynamics of free boundaries”, J. Comput. Phys., v39, pp. 201-225, 1981.

[20] Shyy, W., Thakur, S. and Wright, J., “Second-order upwind and central difference schemes for recirculating flow computation”, AIAA Journal, v30, pp. 923-932, 1992.

[21] Leonard, B. P., “A stable and accurate convective modeling procedure based on quadratic interpolation”, Computer Methods in Applied Mechanics and Engineering, v.19, pp.56-98, 1979.

[22] Zalesak, S. T. , “Fully multi-dimensional flux corrected transport algorithms for fluid flow”, J. Comput. Phys., v31, pp.335-362, 1979.

[23] Harten, A. “High resolution schemes for hyperbolic conservation laws”, J. Comput. Phys., v49, pp. 357-393, 1983.

[24] Leonard, B. P., “Simple high-accuracy resolution program for convective modeling of discontinuities”, In. J. Numer. Methods Fluids, v8, pp.1291-1318, 1988

[25] Van Leer, B., “Towards the ultimate conservative difference scheme. II. Monotonicity and conservation combined in a second-order scheme”, J. Comput. Phys., v14, pp.361-370 1974.

[26] Sweby, P. K., “High resolution schemes using flux limiters for hyperbolic conservation laws”, SIAM J. Numer. Analysis., v21, No.5, pp. 995-1011, 1984.

[27] Gaskell, P. H. and Lau, A. K. C., ”Curvature-compensated convective transport: SMART, a new boundedness-preserving transport algorithm.” Int. J. Numer. Meth. Fluids, v8, pp. 617-641, 1988.

[28] Jasak, H., Weller, H. G. and Gosman, A. D., “High Resolution NVD Differencing Scheme for Arbitrary Unstructured Meshes”, Int. J. for Numer. Meth. Fluids, v31, pp.431-449,

1999.

[29] Roe, P. L., "Large scale computations in fluid mechanics, Part2", In Lectures in Applied Mathematics, Vol. 22, pp. 163-193, 1985.

[30] Darwish, M. S., "A new high-resolution scheme based on the normalized variable formulation", Numer. Heat Trans, Part B, v24, pp. 353-371, 1993.

[31] Van Leer, B., "Towards the Ultimate Conservative Difference Scheme V. A Second-Order Sequel to Godunov's Method", J. Comput. Phys., v135, No.2, pp. 229-248, 1997.

[32] Ubbink, O. and Issa, R. I., "A method for capturing sharp fluid interfaces on arbitrary meshes," J. Comput. Phys., v153, pp.26-50, 1999.

[33] Muzafferija, S., Peric, M., Sames, P. and Schellin, T., "A Two-Fluid Navier-Stokes Solver to Simulate Water Entry", Twenty-Second Symp. On Naval Hydrodynamics, Washington, D.C., pp.638-649, 1998.

[34] Darwish, M. and Moukalled, F., "Convective schemes for capturing interfaces of free-surface flows on unstructured grids," Numer. Heat Trans., Part B, v49, pp.19-42, 2006.

[35] Ubbink, O., "Numerical prediction of two fluid systems with sharp interfaces," thesis submitted from Department of Mechanical Engineering Imperial College of Science, Technology & Medicine, January 1997.

[36] 鄭東庭,「利用流體體積法之雙流體計算」,國立交通大學機械所,碩士論文,2007。

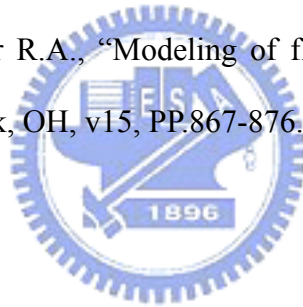
[37] Brackbill, J.U. et al., "A continuum method for modeling surface tension", J. Comput. Phys., v100, PP.335-354, 1967.

[38] Batchelor, G. K., "An introduction to fluid dynamics," Cambridge: Cambridge University Press, 1967.

[39] Adamson, A. W., "Physical chemistry of surfaces," New York: John Wiley & Sons, 1976.

[40] Orlanski, "A simple boundary condition for unbounded hyperbolic flows", J. Computational Physics, v21,pp.251-269,1976.

- [41] Issa, R. I., "Solution of the implicitly discretised fluid flow equations by operator-splitting," J. Comput. Phys, v62, pp. 40-65, 1985.
- [42] Leonard, B. P., "Bounded higher-order upwind multi-dimensional finite-volume convection-diffusion algorithm", in: W. J. Minkowycz, Editor, Advances in Numerical Heat Transfer, Taylor and Francis, 1997.
- [43] Rudman, M., "Volume-tracking methods for interfacial flow calculations", Int. J. Numer. Methods Fluids, v24, pp.671-691, 1997.
- [44] Martin, J. C. and Moyce, W. J., "An experimental study of the collapse of liquid columns on a rigid horizontal plane," Philos. Trans. Roy. Soc. London, vA244, pp.312-324, 1952.
- [45] Koshizuka, S., Tamako, H. and Oka, Y., "A particle method for incompressible viscous flow with fluid fragmentation," Comput. Fluid Dynamics JOURNAL, v4(1), pp.29-46, 1995.
- [46] Hwang, W.-S. and Stoehr R.A., "Modeling of fluid flow", Metal Handbook, 9th Ed., ASM International, Metals Park, OH, v15, PP.867-876.



	NVD form	Flux limiter function
UDS	$\tilde{\alpha}_f = \tilde{\alpha}_D$	$\gamma(r) = 0$
DDS	$\tilde{\alpha}_f = 1$	$\gamma(r) = 2$
CDS	$\tilde{\phi}_f = \frac{1}{2}(1 + \tilde{\alpha}_D)$	$\gamma(r) = 1$
QUICK	$\tilde{\alpha}_f = \frac{3}{4}\tilde{\alpha}_D + \frac{3}{8}$	$\gamma(r) = \frac{1}{4}r + \frac{3}{4}$
CUS	$\tilde{\alpha}_f = \frac{5}{6}\tilde{\alpha}_D + \frac{1}{3}$	$\gamma(r) = \frac{1}{3}r + \frac{2}{3}$
Formm	$\tilde{\alpha}_f = \tilde{\alpha}_D + \frac{1}{4}$	$\gamma(r) = \frac{1}{2}(r+1)$
LUS	$\tilde{\alpha}_f = \frac{3}{2}\tilde{\alpha}_D$	$\gamma(r) = r$
SMART	$\tilde{\alpha}_D \geq 1$ or $\tilde{\alpha}_D \leq 0, \tilde{\alpha}_f = \tilde{\alpha}_D$ $\frac{1}{6} \geq \tilde{\alpha}_D > 0, \tilde{\alpha}_f = 3\tilde{\alpha}_D$ $\frac{5}{6} \geq \tilde{\alpha}_D > \frac{1}{6}, \tilde{\alpha}_f = \frac{3}{4}\tilde{\alpha}_D + \frac{3}{8}$ $1 > \tilde{\alpha}_D > \frac{5}{6}, \tilde{\alpha}_f = 1$	$\gamma(r) = \max\{0, \min(2, \frac{1}{4}r + \frac{3}{4}, 4r)\}$
MUSCL	$\tilde{\alpha}_D \geq 1$ or $\tilde{\alpha}_D \leq 0, \tilde{\alpha}_f = \tilde{\alpha}_D$ $\frac{1}{4} \geq \tilde{\alpha}_D > 0, \tilde{\phi}_f = 2\tilde{\alpha}_D$ $\frac{3}{4} \geq \tilde{\alpha}_D > \frac{1}{4}, \tilde{\alpha}_f = \tilde{\alpha}_D + \frac{1}{4}$ $1 > \tilde{\alpha}_D > \frac{3}{4}, \tilde{\alpha}_f = 1$	$\gamma(r) = \max\{0, \min(2, \frac{1}{2}r + \frac{1}{2}, 2r)\}$

<p>SUPERBE E</p>	$\tilde{\alpha}_D \geq 1 \text{ or } \tilde{\alpha}_D \leq 0, \tilde{\alpha}_f = \tilde{\alpha}_D$ $\frac{1}{3} \geq \tilde{\alpha}_D > 0, \quad \tilde{\alpha}_f = 2\tilde{\alpha}_D$ $\frac{1}{2} \geq \tilde{\alpha}_D > \frac{1}{3}, \quad \tilde{\alpha}_f = \frac{1}{2}(\tilde{\alpha}_D + 1)$ $\frac{2}{3} \geq \tilde{\alpha}_D > \frac{1}{2}, \quad \tilde{\alpha}_f = \frac{3}{2}\tilde{\alpha}_D$ $1 > \tilde{\alpha}_D > \frac{2}{3}, \quad \tilde{\alpha}_f = 1$	$\gamma(r) = \max\{0, \min(r, 2), \min(2r, 1)\}$
<p>STOIC</p>	$\tilde{\alpha}_D \geq 1 \text{ or } \tilde{\alpha}_D \leq 0, \tilde{\alpha}_f = \tilde{\alpha}_D$ $\frac{1}{5} \geq \tilde{\alpha}_D > 0, \quad \tilde{\alpha}_f = 3\tilde{\alpha}_D$ $\frac{1}{2} \geq \tilde{\alpha}_D > \frac{1}{5}, \quad \tilde{\alpha}_f = \frac{1}{2}(\tilde{\alpha}_D + 1)$ $\frac{5}{6} \geq \tilde{\alpha}_D > \frac{1}{2}, \quad \tilde{\alpha}_f = \frac{3}{4}\tilde{\alpha}_D + \frac{3}{8}$ $1 > \tilde{\alpha}_D > \frac{5}{6}, \quad \tilde{\alpha}_f = 1$	$\gamma(r) = \max\{0, \min[2, 4r, \max(1, \frac{1}{4}r + \frac{3}{4})]\}$
<p>OSHER</p>	$\tilde{\alpha}_D \geq 1 \text{ or } \tilde{\alpha}_D \leq 0, \tilde{\alpha}_f = \tilde{\alpha}_D$ $\frac{2}{3} \geq \tilde{\alpha}_D > 0, \quad \tilde{\alpha}_f = \frac{3}{2}\tilde{\alpha}_D$ $1 > \tilde{\alpha}_D > \frac{2}{3}, \quad \tilde{\alpha}_f = 1$	$\gamma(r) = \max\{0, \min(r, 2)\}$
<p>BDS</p>	$\tilde{\alpha}_D \geq 1 \text{ or } \tilde{\alpha}_D \leq 0, \tilde{\alpha}_f = \tilde{\alpha}_D$ $\frac{1}{2} \geq \tilde{\alpha}_D > 0, \quad \tilde{\alpha}_f = 2\tilde{\alpha}_D$ $1 > \tilde{\alpha}_D > \frac{1}{2}, \quad \tilde{\alpha}_f = 1$	$\gamma(r) = \max\{0, \min(2r, 2)\}$
<p>Van Leer</p>	$\tilde{\alpha}_D \geq 1 \text{ or } \tilde{\alpha}_D \leq 0, \tilde{\alpha}_f = \tilde{\alpha}_D$ $1 > \tilde{\alpha}_D > 0, \quad \tilde{\alpha}_f = 2\tilde{\alpha}_D - \tilde{\alpha}_D^2$	$\gamma(r) = \frac{r +  r }{r + 1}$
<p>CHARM</p>	$\tilde{\alpha}_D \geq 1 \text{ or } \tilde{\alpha}_D \leq 0, \tilde{\alpha}_f = \tilde{\alpha}_D$ $1 \geq \tilde{\alpha}_D > 0,$ $\tilde{\alpha}_f = \tilde{\alpha}_D(\tilde{\alpha}_D^2 - 2.5\tilde{\alpha}_D + 2.5)$	$\gamma(r) = \frac{r(r+3)}{(r+1)^2}, \quad r > 0$ $\gamma(r) = 0, \quad r \leq 0$

M-BDS	$\tilde{\alpha}_D \geq 1$ or $\tilde{\alpha}_D \leq 0, \tilde{\alpha}_f = \tilde{\alpha}_D$ $\frac{1}{2} \geq \tilde{\alpha}_D > 0, \quad \tilde{\alpha}_f = 3\tilde{\alpha}_D$ $1 > \tilde{\alpha}_D > \frac{1}{2}, \quad \tilde{\alpha}_f = 1$	$\gamma(r) = \max\{0, \min(4r, 2)\}$
M-MUSCL	$\tilde{\alpha}_D \geq 1$ or $\tilde{\alpha}_D \leq 0, \tilde{\alpha}_f = \tilde{\alpha}_D$ $\frac{1}{4} \geq \tilde{\alpha}_D > 0, \quad \tilde{\phi}_f = 3\tilde{\alpha}_D$ $\frac{3}{4} \geq \tilde{\alpha}_D > \frac{1}{4}, \quad \tilde{\alpha}_f = \tilde{\alpha}_D + \frac{1}{4}$ $1 > \tilde{\alpha}_D > \frac{3}{4}, \quad \tilde{\alpha}_f = 1$	$\gamma(r) = \max\{0, \min(2, \frac{1}{2}r + \frac{1}{2}, 4r)\}$

Table 4.1 The NVD equation and flux limiter function of linear and non-linear difference schemes



Scheme	Hollow circle	Hollow square
UDS	1.2274	1.2568
CUS	0.4223	0.5156
DDS	0.3245	0.2074
BDS	0.2362	0.3399
CDS	0.6027	0.6933
MUSCL	0.4943	0.5802
SUPERBEE	0.3123	0.4271
M-MUSCL	0.4623	0.5520
M-BDS	0.1283	0.1544

Table 5.1 Errors of different schemes in  $Co = 0.25$  (quadrilateral mesh)

Scheme	Hollow circle	Hollow square
UDS	1.2281	1.2566
CUS	0.5392	0.5971
DDS	0.7116	0.6572
BDS	0.2258	0.3523
CDS	0.7011	0.7599
MUSCL	0.5190	0.5935
SUPERBEE	0.3171	0.4476
M-MUSCL	0.4957	0.5639
M-BDS	0.2818	0.2408

Table 5.2 Errors of different schemes in  $Co = 0.75$  (quadrilateral mesh)

Scheme	Hollow circle	Hollow square
UDS	1.0846	1.0418
CUS	0.3469	0.3402
DDS	0.2587	0.2415
BDS	0.1797	0.1806
CDS	0.4305	0.4169
MUSCL	0.3460	0.3388
SUPERBEE	0.2282	0.2246
M-MUSCL	0.3419	0.3349
M-BDS	0.1745	0.1635

Table 5.3 Errors of different schemes in  $Co = 0.25$  (triangular mesh)

Scheme	Hollow circle	Hollow square
UDS	1.0846	1.0417
CUS	0.3809	0.3732
DDS	0.5324	0.5618
BDS	0.1787	0.1828
CDS	0.4653	0.4472
MUSCL	0.3638	0.3565
SUPERBEE	0.2378	0.2342
M-MUSCL	0.3596	0.3528
M-BDS	0.1819	0.1684

Table 5.4 Errors of different schemes in  $Co = 0.75$  (triangular mesh)

Scheme	Hollow circle	Hollow square
CICSAM	0.1267	0.1280
HRIC	0.3259	0.3714
SUPERBEE+MUSCL	0.3812	0.4429
M-BDS+M-MUSCL	0.1173	0.1666

Table 5.5 Errors of different composite schemes in  $Co = 0.25$  (quadrilateral mesh)

Scheme	Hollow circle	Hollow square
CICSAM	1.0000	1.0041
HRIC	0.2276	0.2438
SUPERBEE+MUSCL	0.4031	0.4612
M-BDS+M-MUSCL	0.1889	0.2521

Table 5.6 Errors of different composite schemes in  $Co = 0.75$  (quadrilateral mesh)

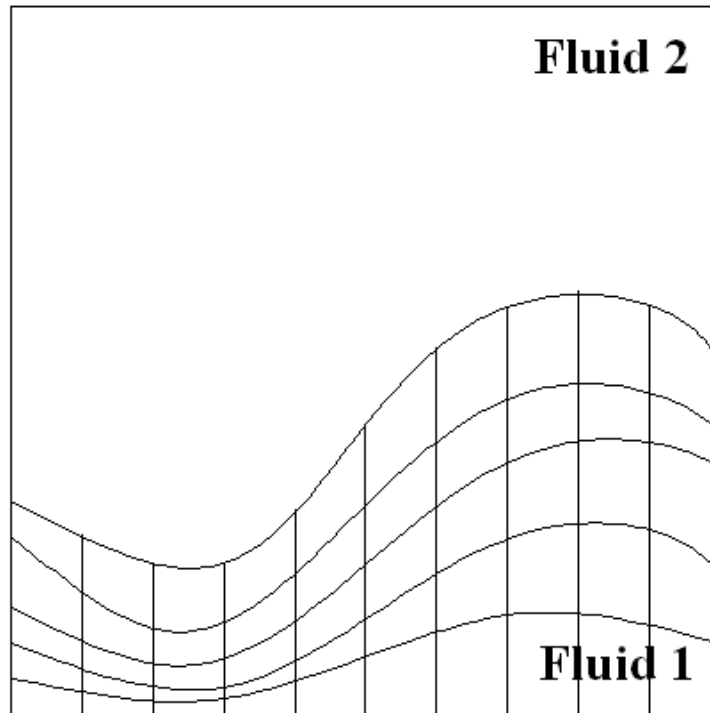
Scheme	Hollow circle	Hollow square
CICSAM	0.1556	0.1514
HRIC	0.1813	0.1869
SUPERBEE+MUSCL	0.2697	0.2660
M-BDS+M-MUSCL	0.1652	0.1641

Table 5.7 Errors of different composite schemes in  $Co = 0.25$  (triangular mesh)

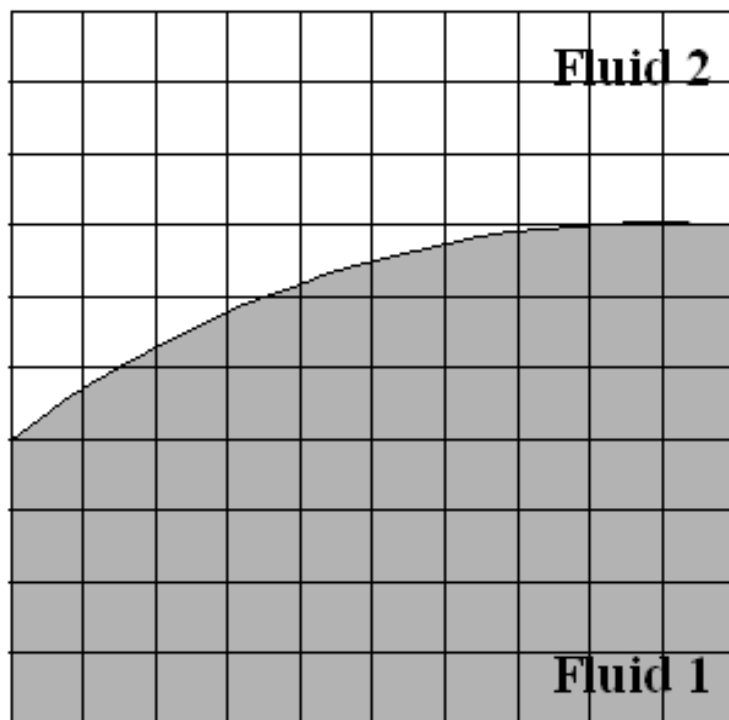
Scheme	Hollow circle	Hollow square
CICSAM	0.2090	0.2055
HRIC	0.2111	0.1793
SUPERBEE+MUSCL	0.2841	0.2824
M-BDS+M-MUSCL	0.1920	0.1734

Table 5.8 Errors of different composite schemes in  $Co = 0.75$  (triangular mesh)





(a)



(b)

Figure 1.1 The method of two-fluid flow (a) Lagrangian (b) Eulerian scheme

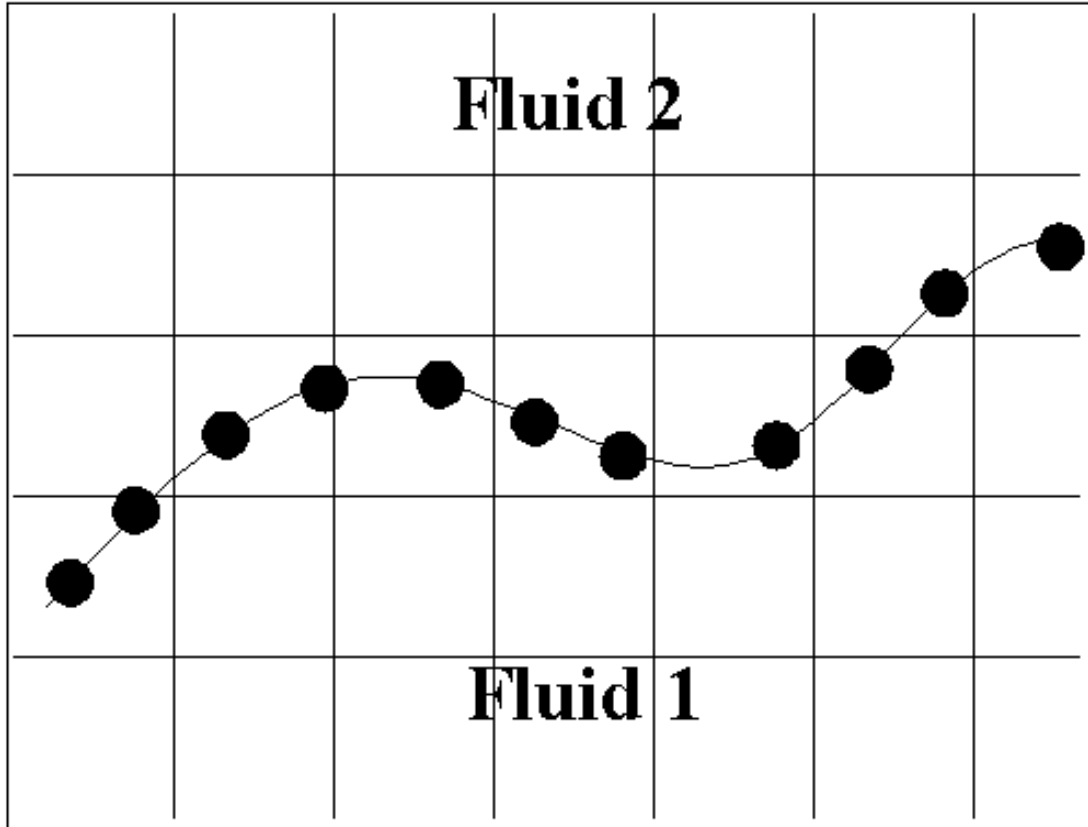


Figure 1.2 Front tracking method

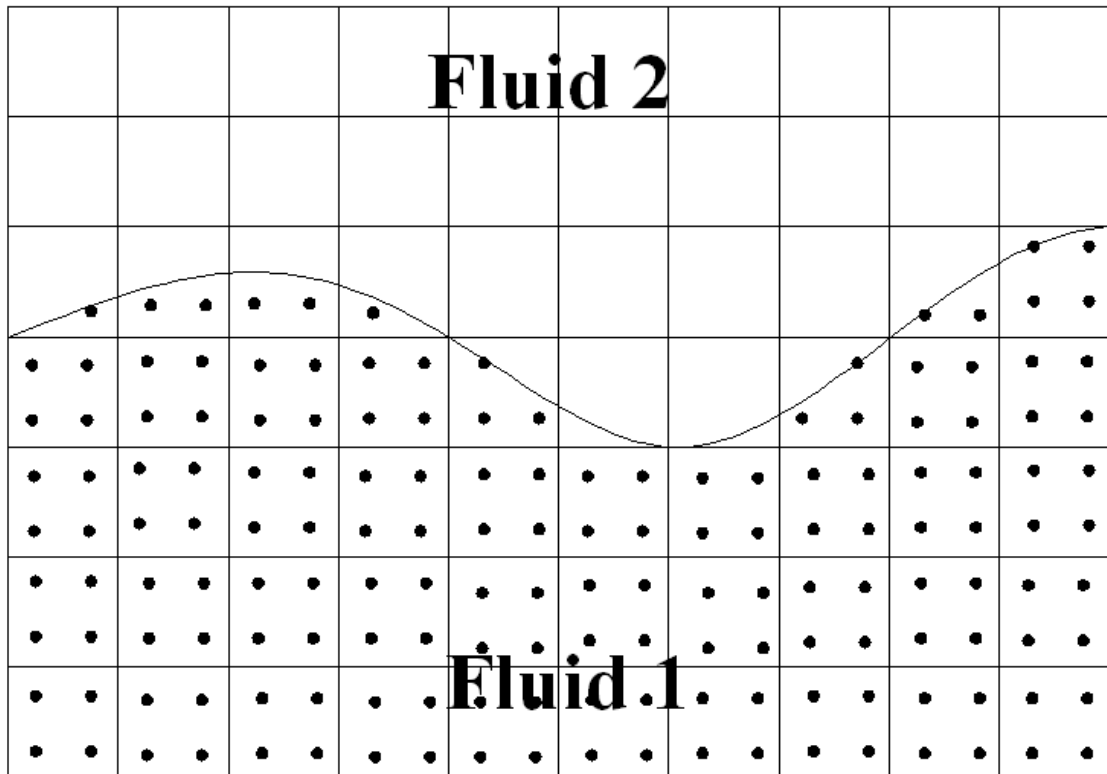
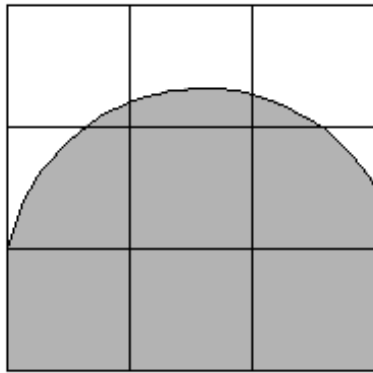
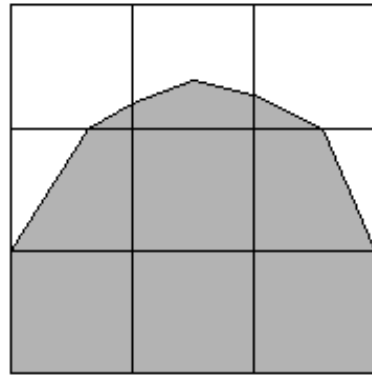


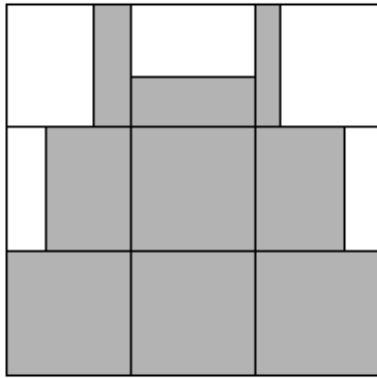
Figure 1.3 Marker and cell method



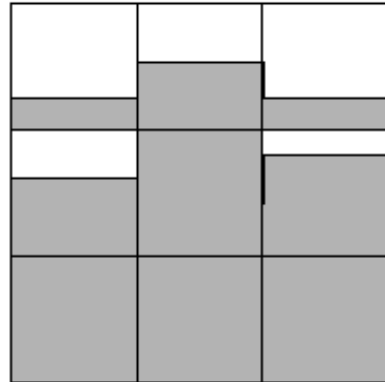
(a) original distribution



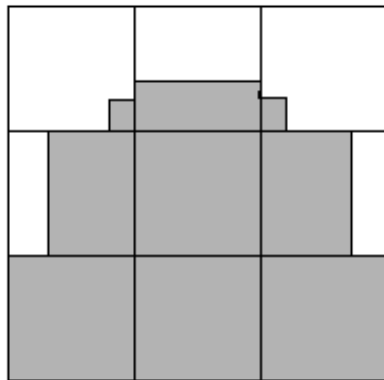
(b) Young' VOF



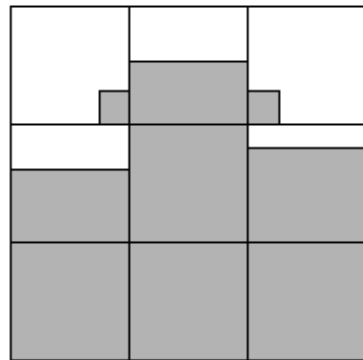
(c) SLIC with x-sweep



(d) SLIC with y-sweep



(e) Chorin with x-sweep



(f) Chorin SLIC with x-sweep

Figure 1.4 Line techniques

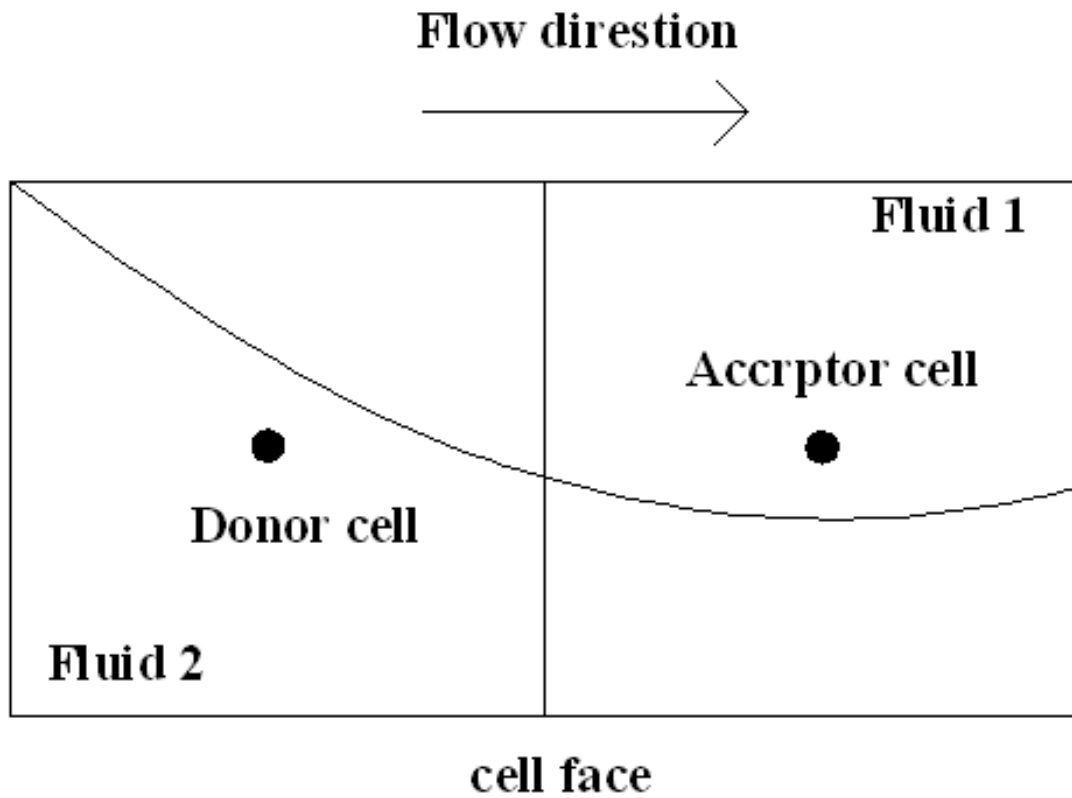


Figure 1.5 Donor and acceptor cell configuration



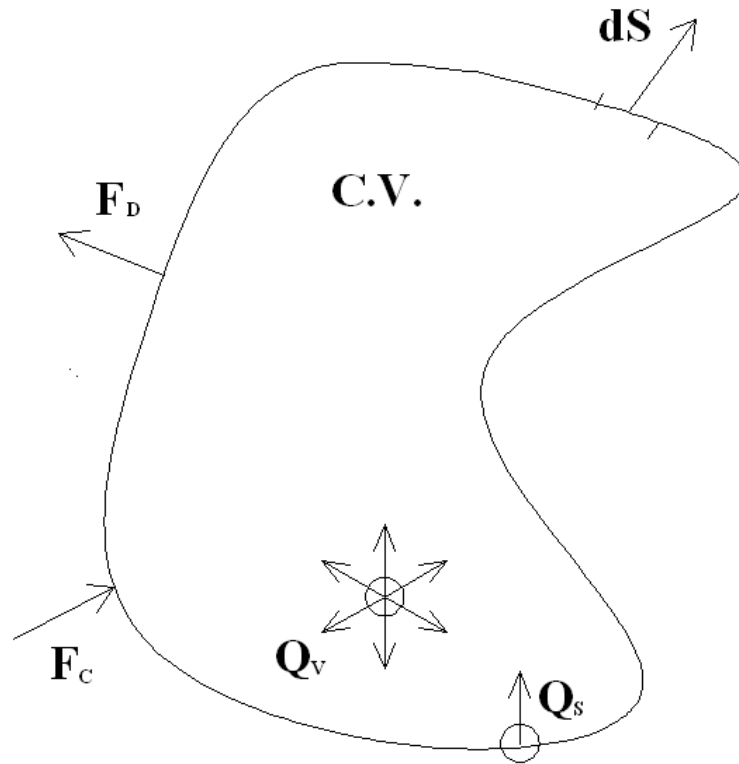


Figure 2.1 General form of the conservation law

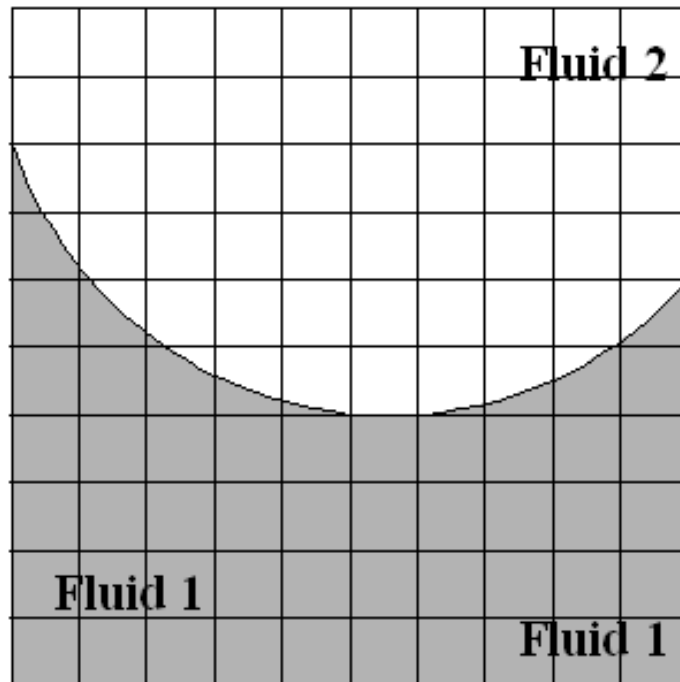


Figure 2.2 VOF method on the Eulerian grids

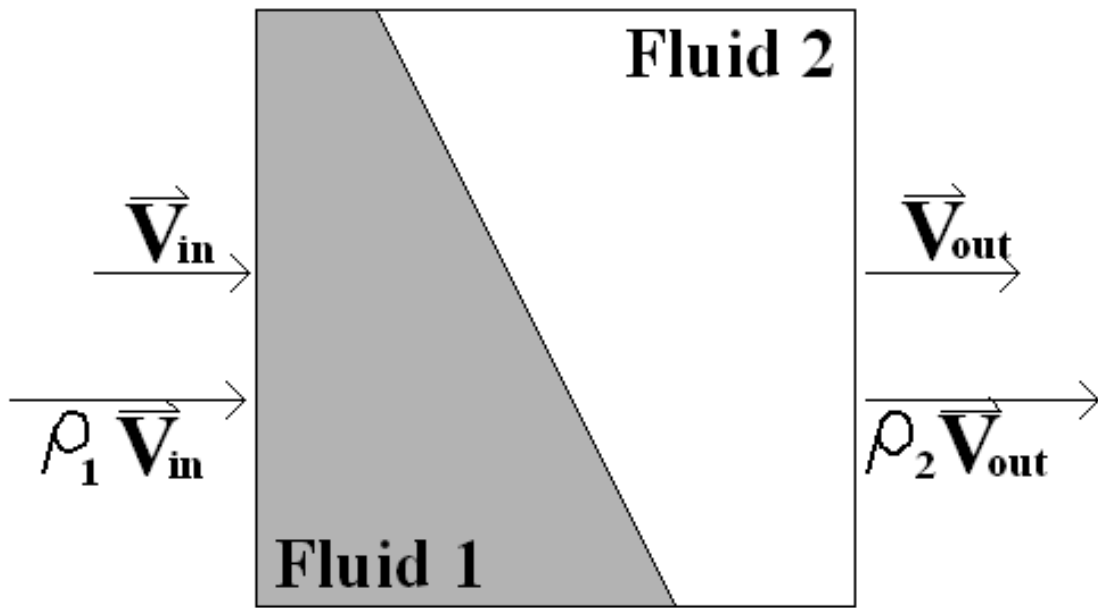


Figure 2.3 Continuity of the velocity and discontinuity of the momentum

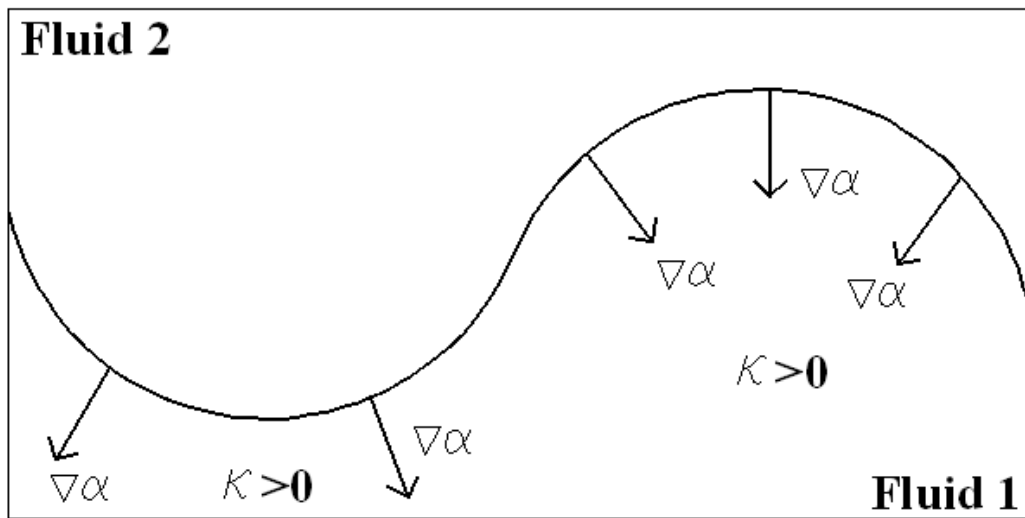


Figure 2.4 Fluid arrangements and the sign of the curvature

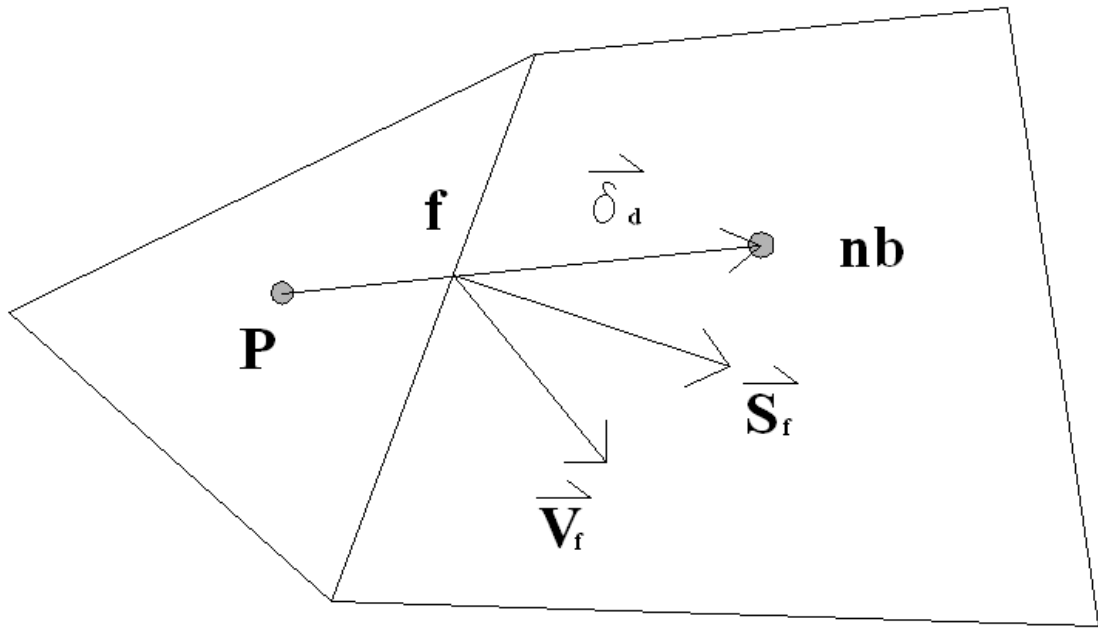


Figure 3.1 Illustration of the primary cell  $P$  and the neighbor cell  $nb$  with a considering face



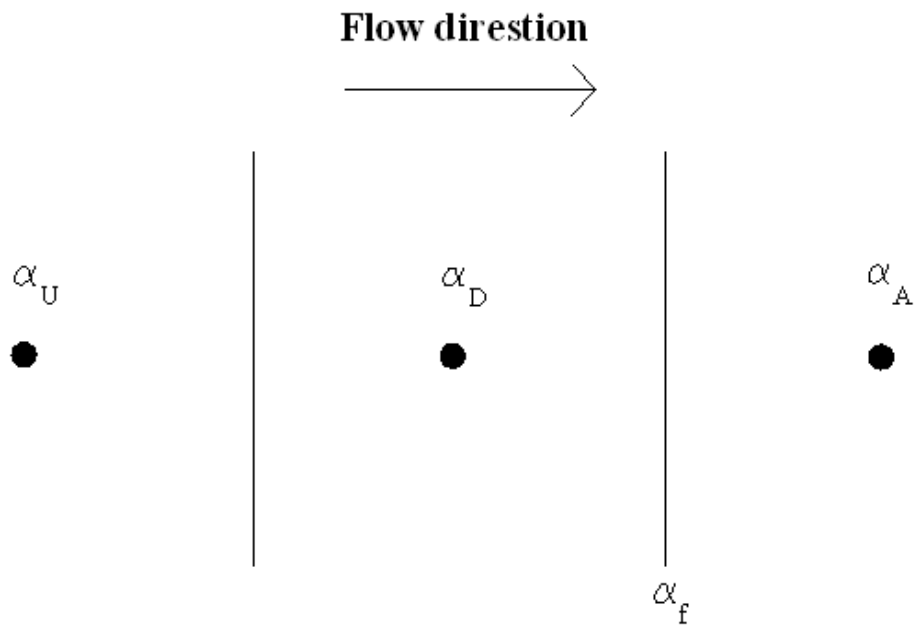


Figure 4.1 The relationship of a control volume and its neighbor cells

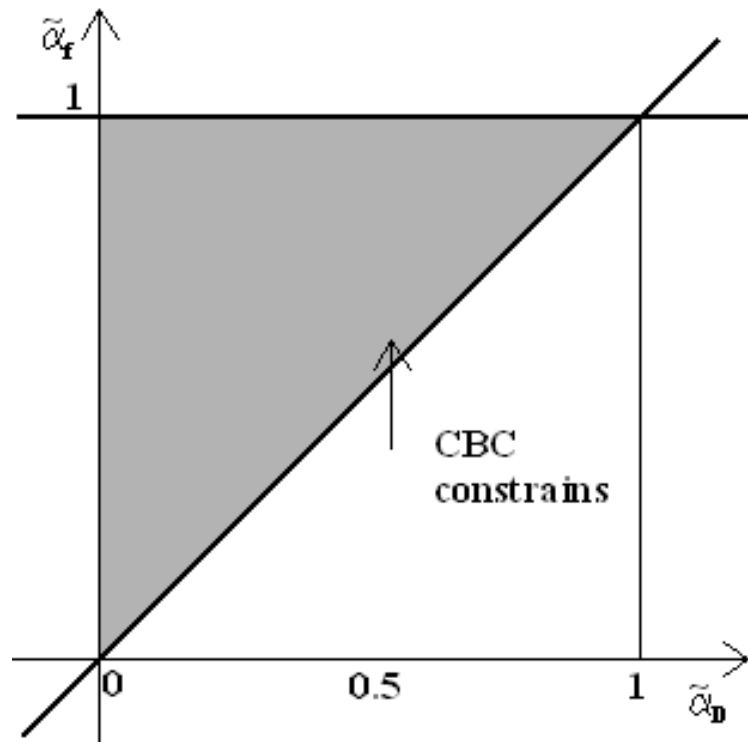


Figure 4.2 The CBC constraint in NVD



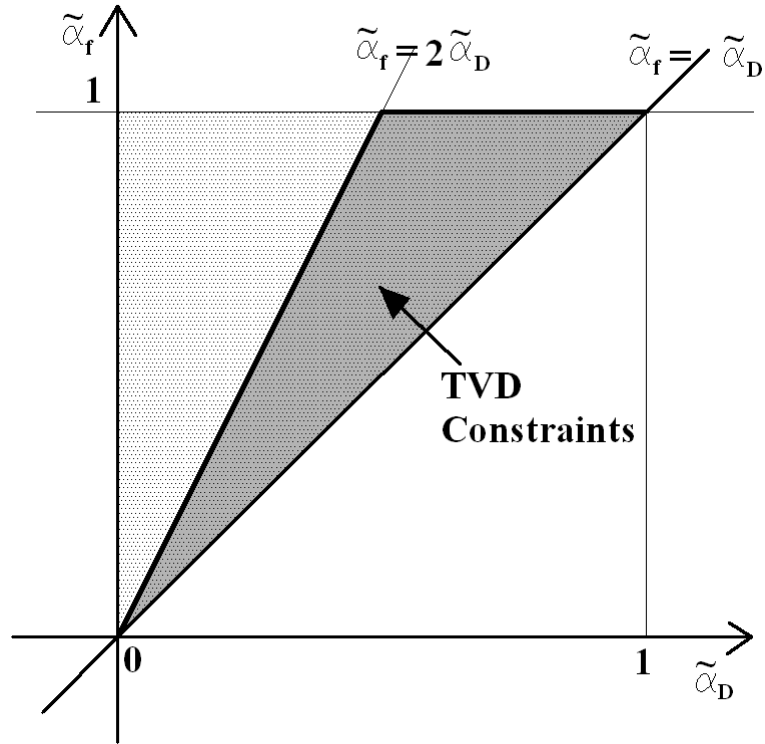


Figure 4.3 The CBC constraint in NVD

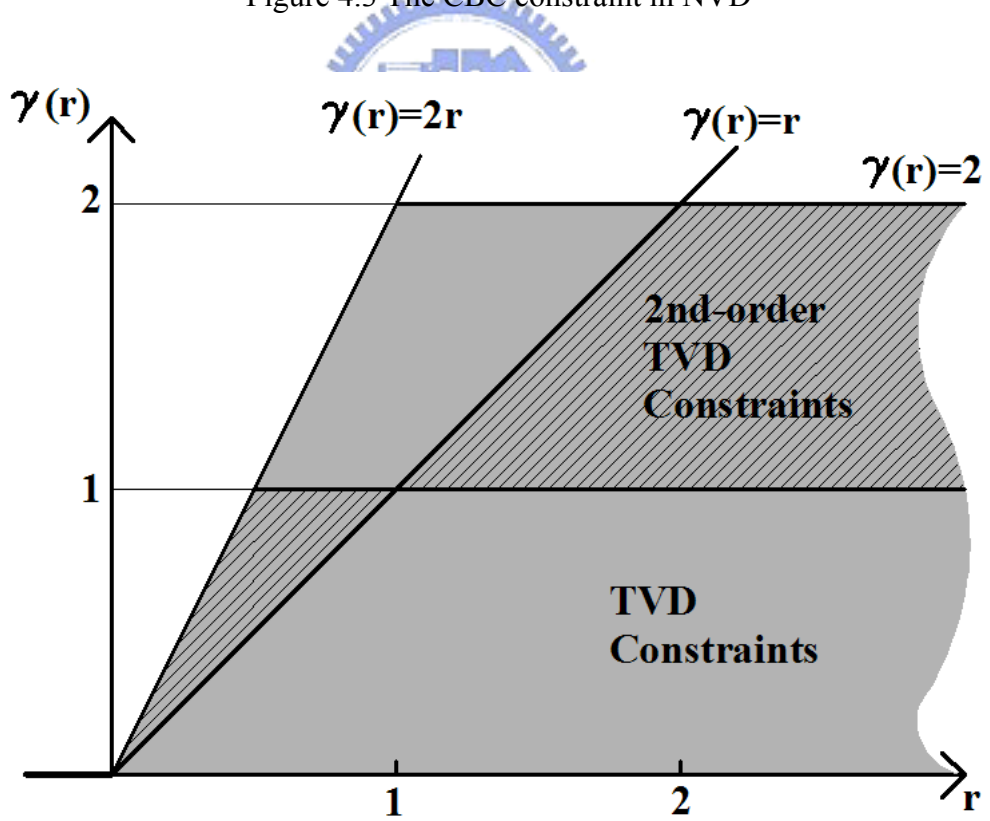


Figure 4.4 The TVD condition in TVD diagram

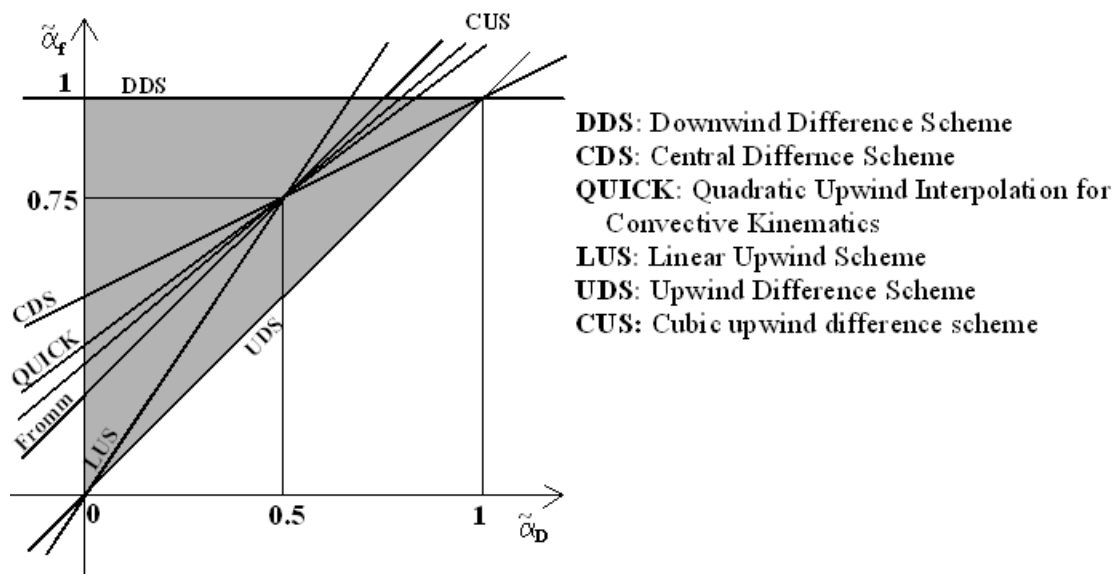


Figure4.5 Linear schemes in Normalized Variable Diagram

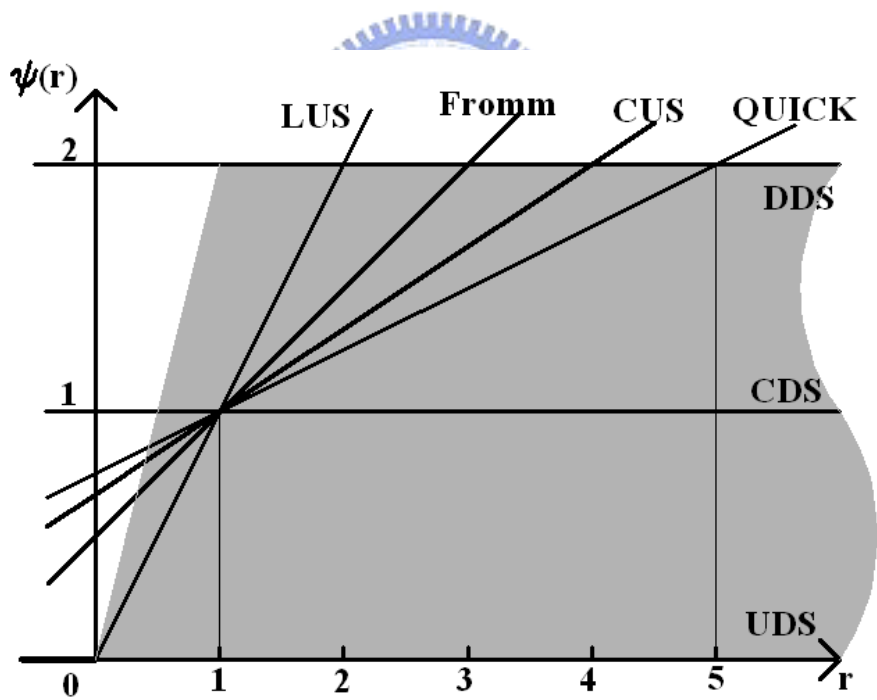


Figure4.6 Linear schemes in TVD Diagram

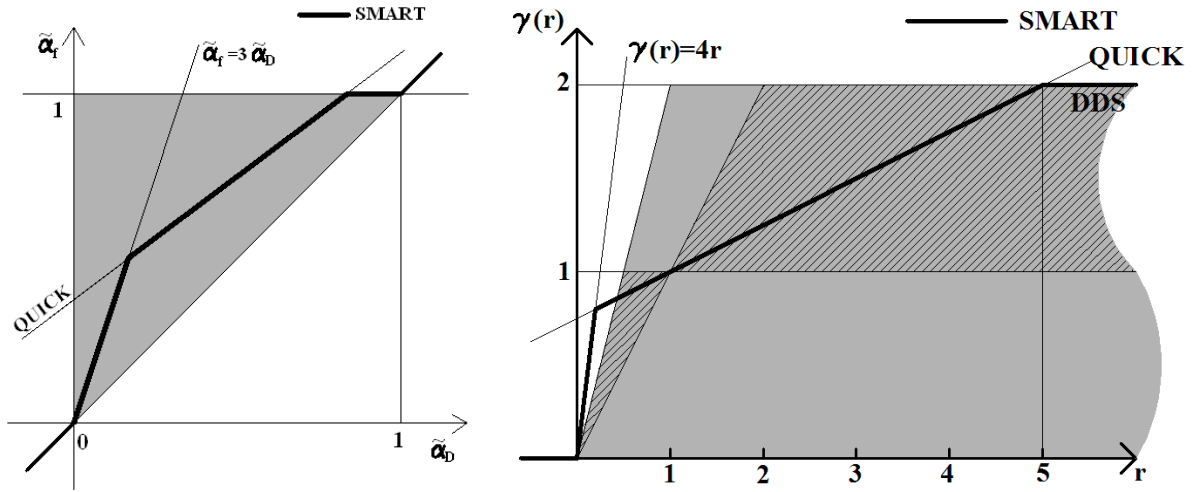


Figure 4.7 SMART

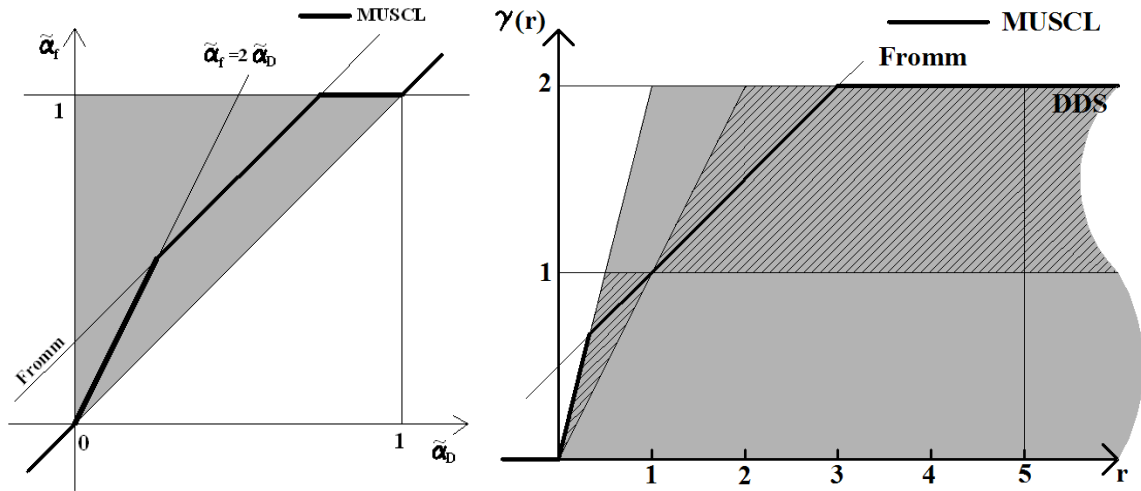


Figure 4.8 MUSCL

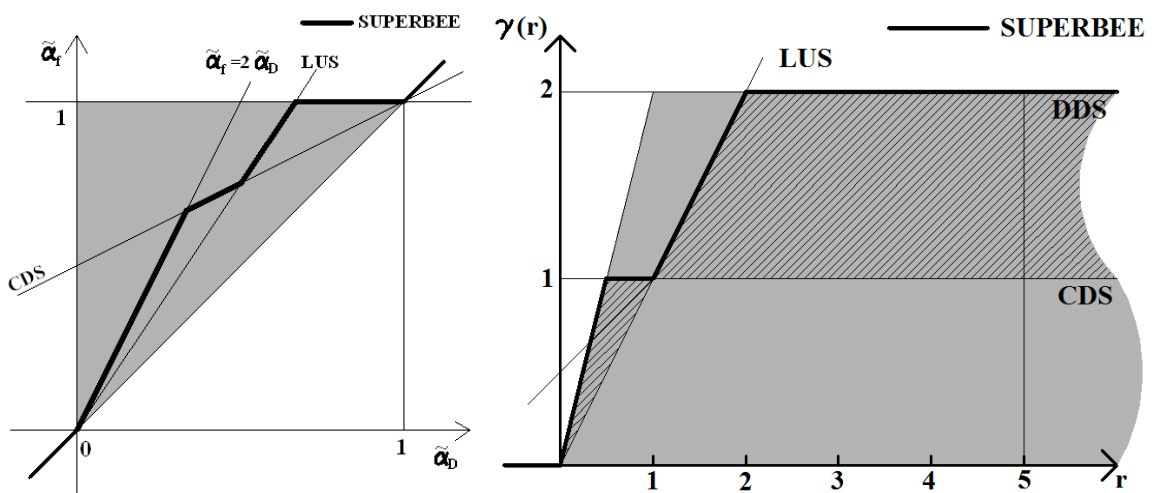


Figure 4.9 SUPERBEE

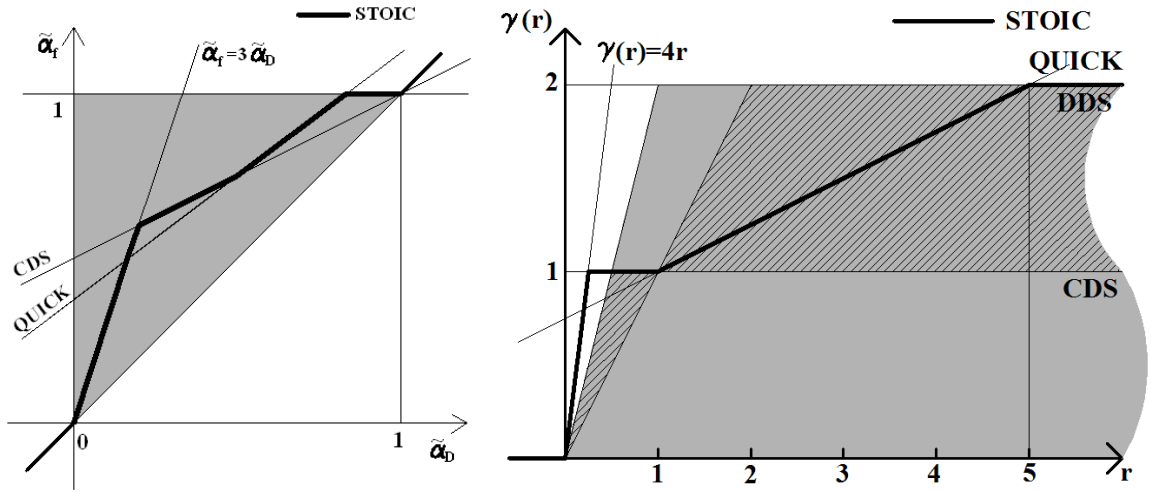


Figure 4.10 STOIC

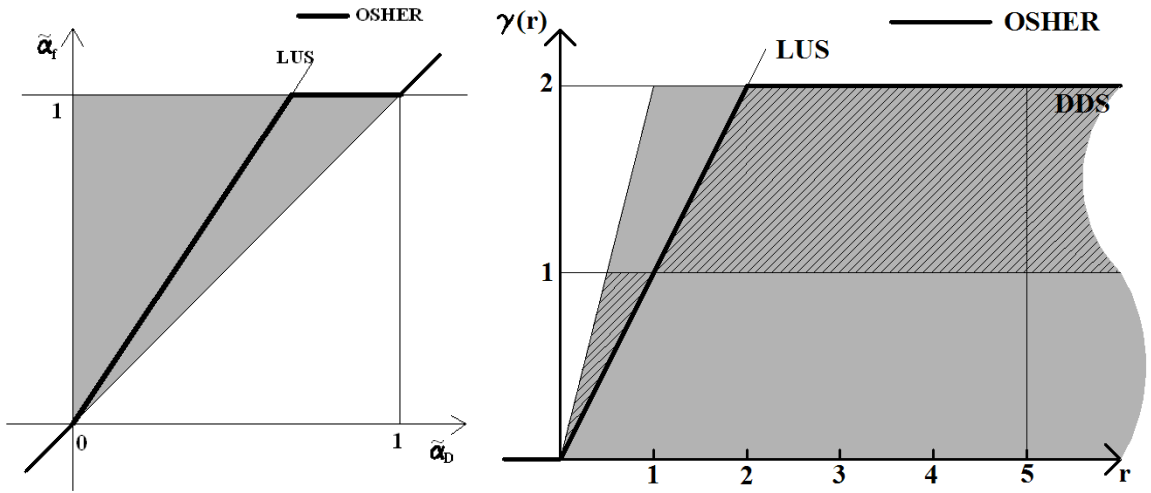


Figure 4.11 OSHER

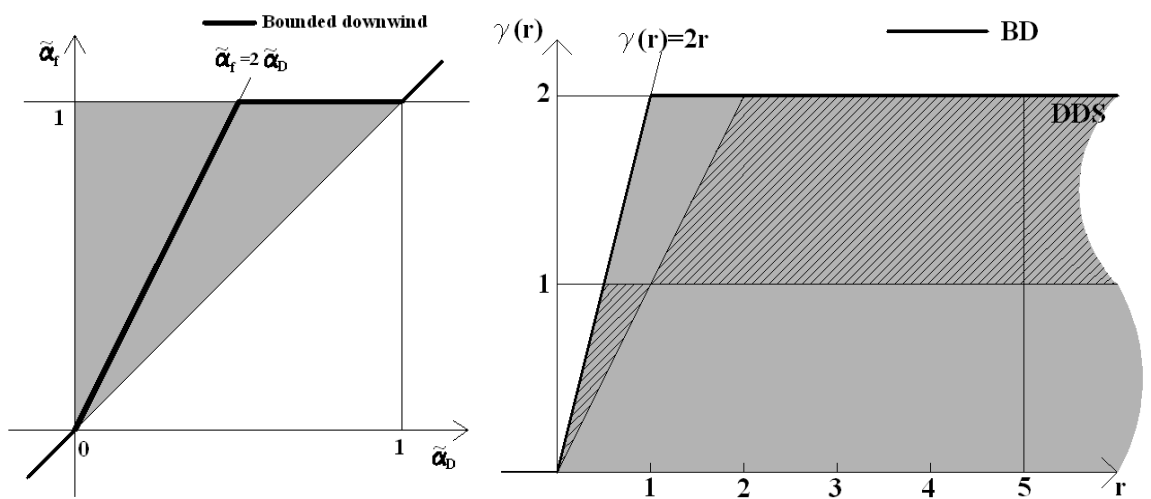


Figure 4.12 BDS

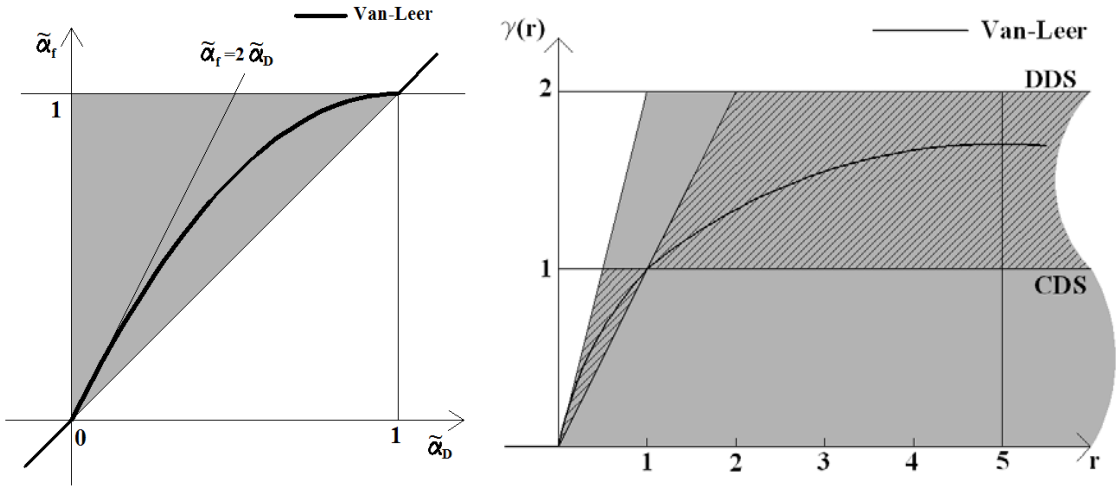


Figure 4.13 Van Leer

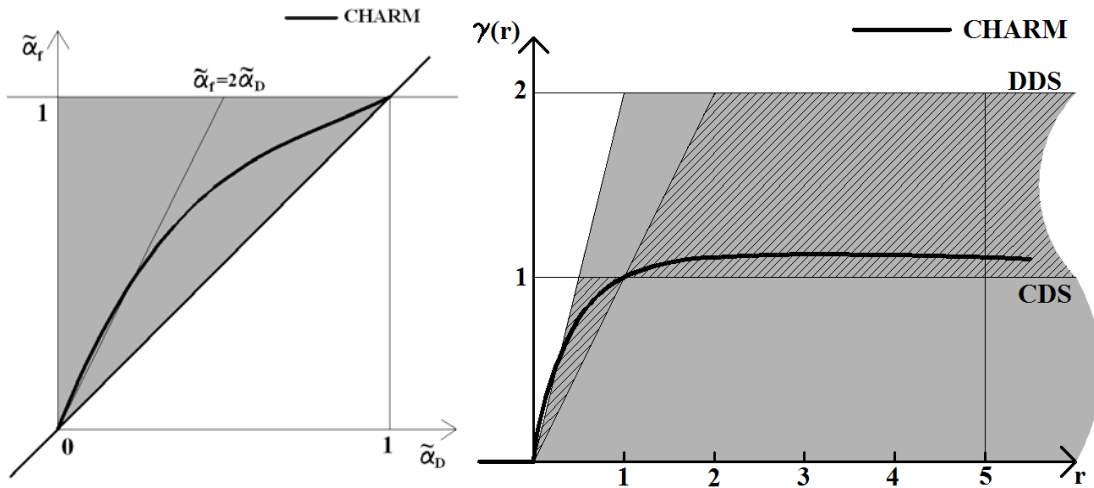


Figure 4.14 CHARM

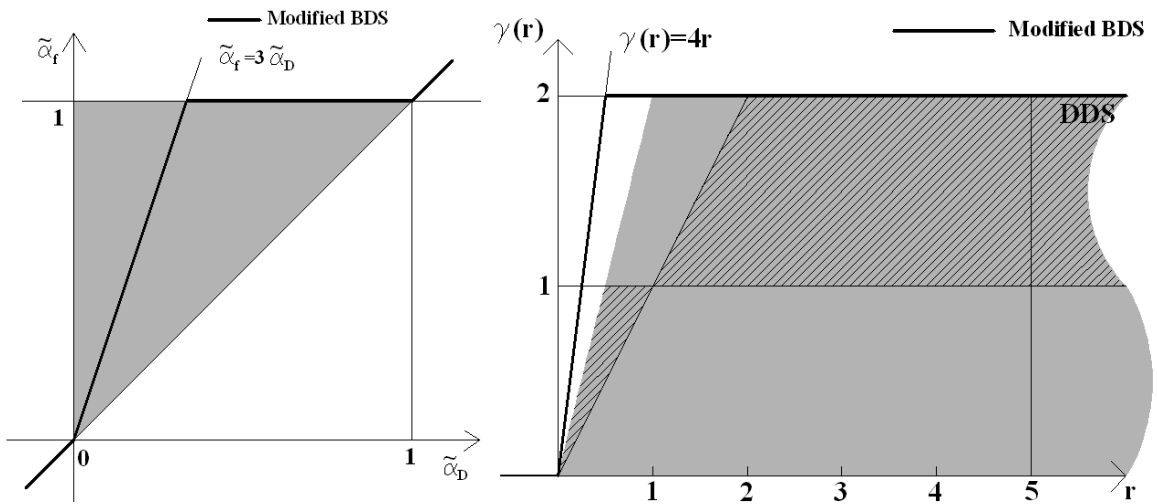


Figure 4.15 Modified BDS

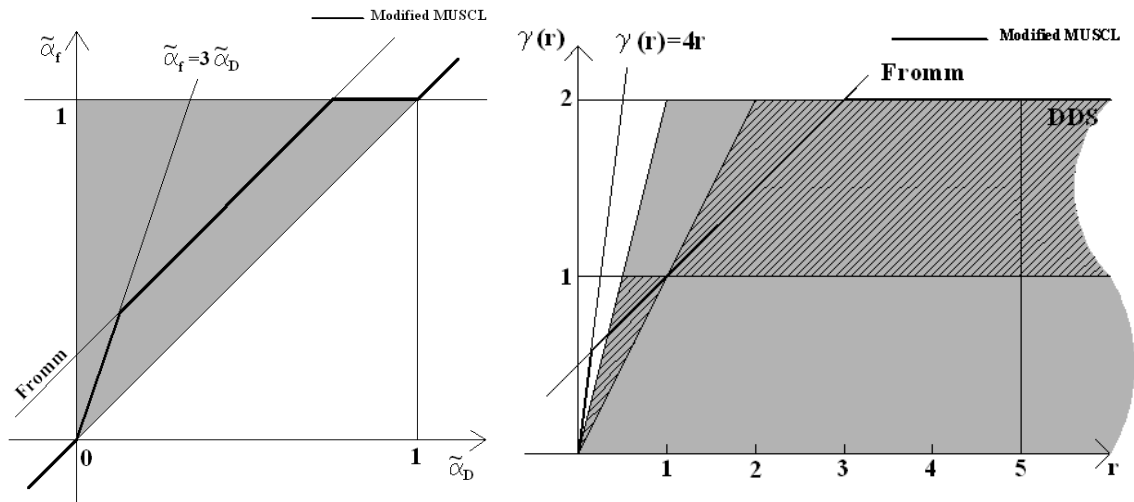


Figure 4.16 Modified MUSCL

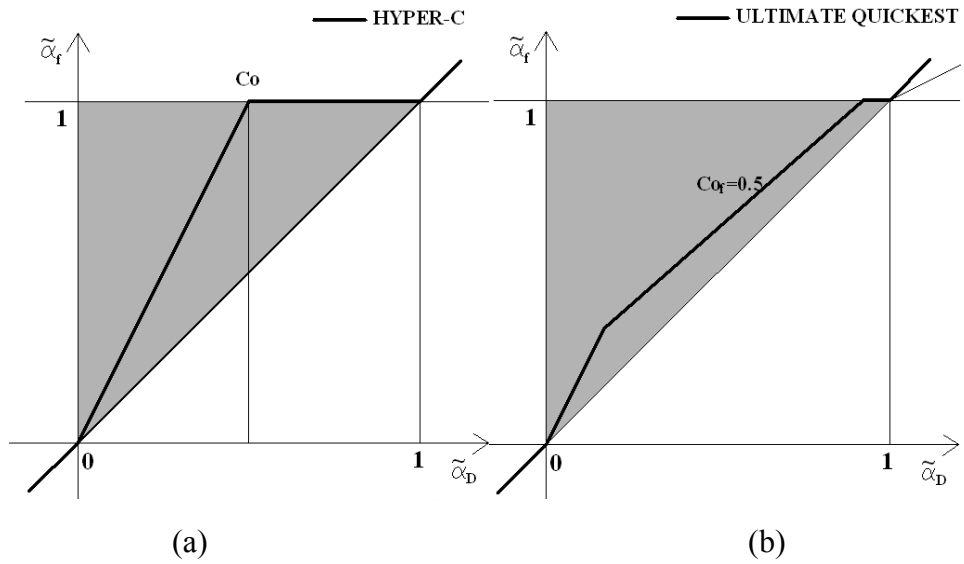


Figure 4.17 The NVD of (a) HYPER-C and (b) UQ ( $C_o = 0.5$ )

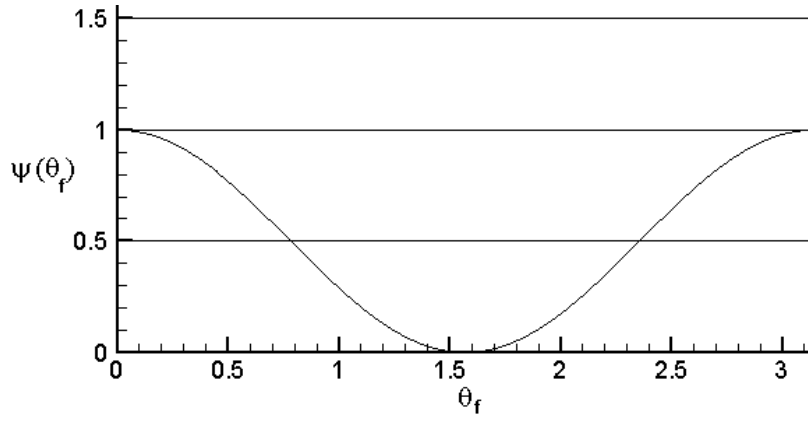


Figure 4.18 The switching function of CICSAM scheme

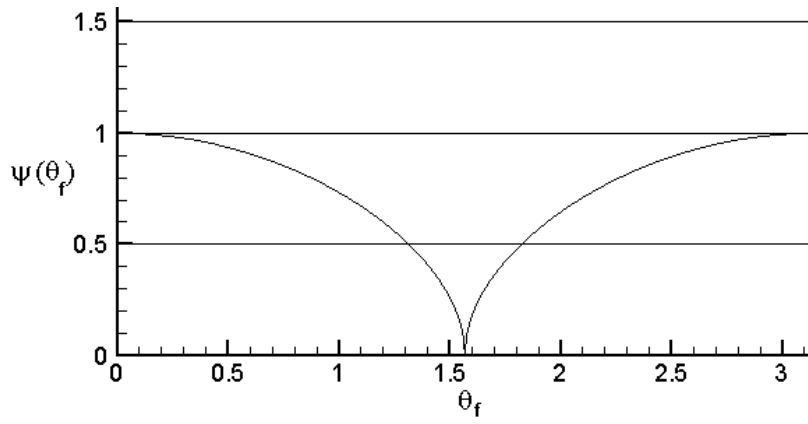


Figure 4.19 The switching function of HRIC scheme

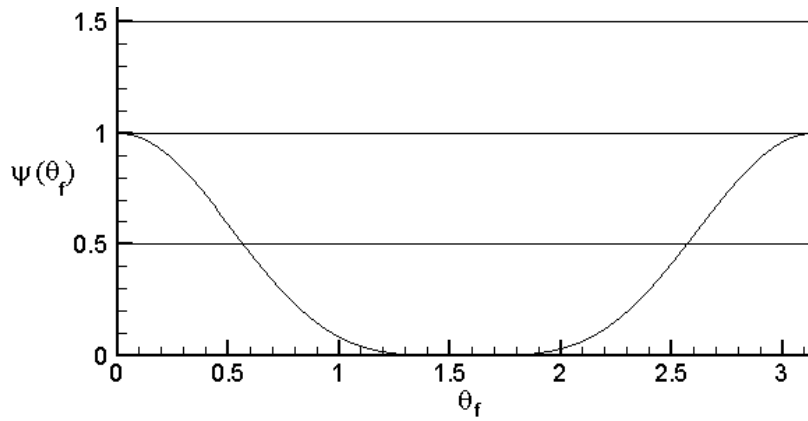


Figure 4.20 The switching function of the composite of M-MUSCL and M-BDS

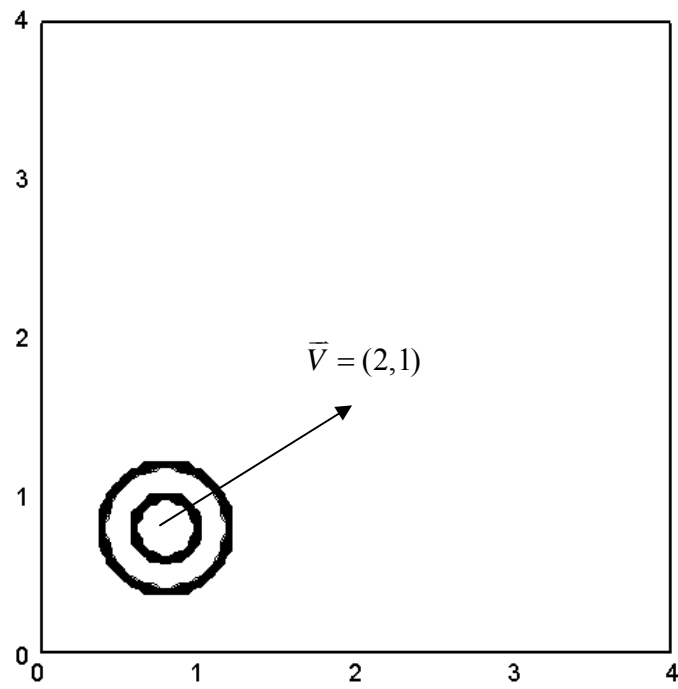


Figure 5.1 (a) The constant velocity field and initial position of hollow circle

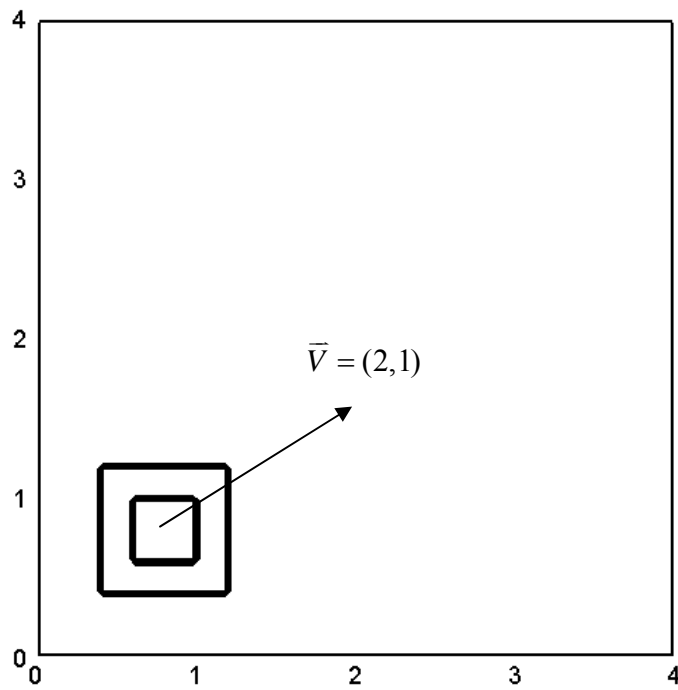


Figure 5.1 (b) The constant velocity field and initial position of hollow square



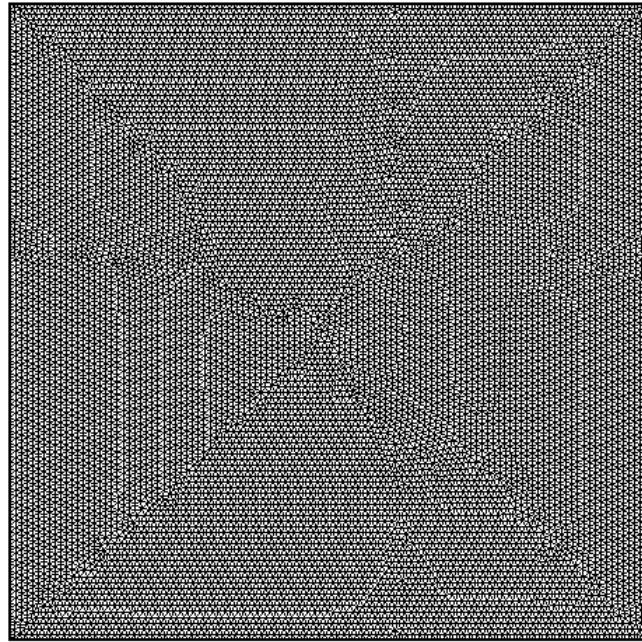


Figure 5.2 Triangular computational mesh in uniform density flow (22478 cells)



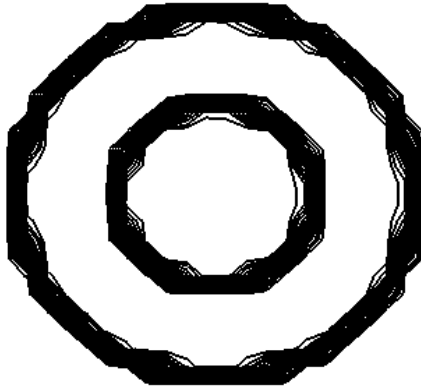


Figure 5.3 (a) The exact distribution of the hollow circle

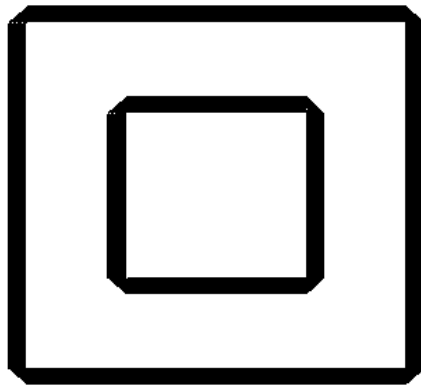


Figure 5.3 (b) The exact distribution of the hollow square

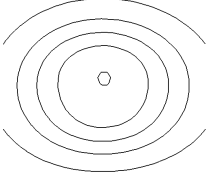
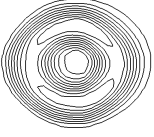

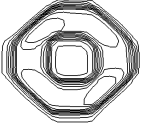
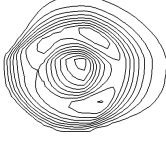
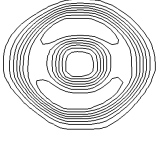
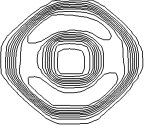
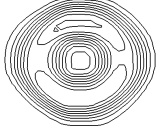
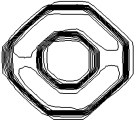
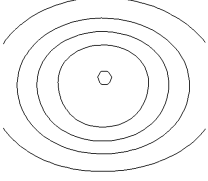


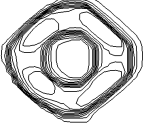

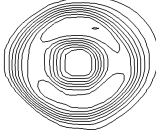
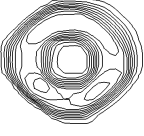
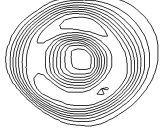
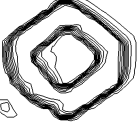
<b>Co=0.25</b>		
		
<b>Upwind Difference Scheme</b>	<b>Cubic Upwind Scheme</b>	<b>Downwind Difference Scheme</b>
		
<b>Bounded Downwind Scheme</b>	<b>Central Difference Scheme</b>	<b>MUSCL</b>
		
<b>SUPERBEE</b>	<b>Modified MUSCL</b>	<b>Modified BDS</b>
<b>Co=0.75</b>		
		
<b>Upwind Difference Scheme</b>	<b>Cubic Upwind Scheme</b>	<b>Downwind Difference Scheme</b>
		
<b>Bounded Downwind Scheme</b>	<b>Central Difference Scheme</b>	<b>MUSCL</b>
		
<b>SUPERBEE</b>	<b>Modified MUSCL</b>	<b>Modified BDS</b>

Figure 5.4 The final shape of hollow circle from different schemes in quadrilateral mesh

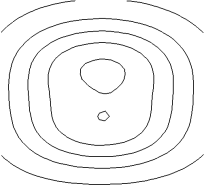
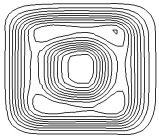
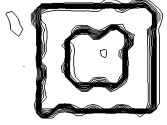


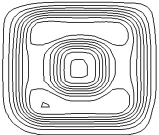
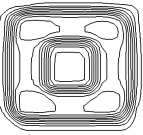
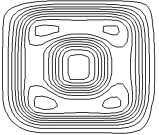

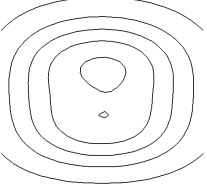




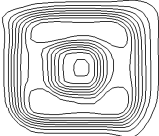
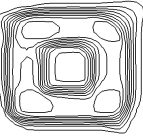
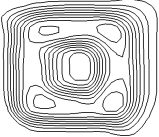
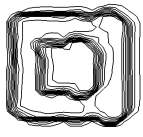
<b>Co=0.25</b>		
		
<b>Upwind Difference Scheme</b>	<b>Cubic Upwind Scheme</b>	<b>Downwind Difference Scheme</b>
		
<b>Bounded Downwind Scheme</b>	<b>Central Difference Scheme</b>	<b>MUSCL</b>
		
<b>SUPERBEE</b>	<b>Modified MUSCL</b>	<b>Modified BDS</b>
<b>Co=0.75</b>		
		
<b>Upwind Difference Scheme</b>	<b>Cubic Upwind Scheme</b>	<b>Downwind Difference Scheme</b>
		
<b>Bounded Downwind Scheme</b>	<b>Central Difference Scheme</b>	<b>MUSCL</b>
		
<b>SUPERBEE</b>	<b>Modified MUSCL</b>	<b>Modified BDS</b>

Figure 5.5 The final shape of hollow square from different schemes in quadrilateral mesh

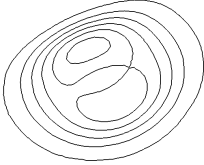
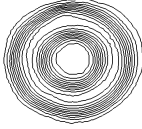



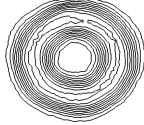
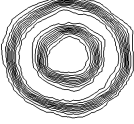
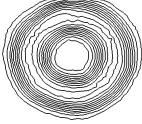
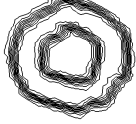
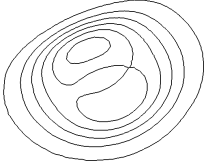
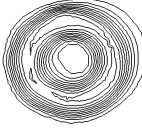

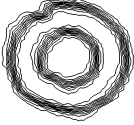


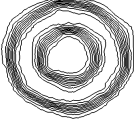
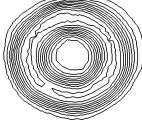
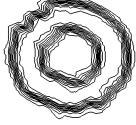
<b>Co=0.25</b>		
		
<b>Upwind Difference Scheme</b>	<b>Cubic Upwind Scheme</b>	<b>Downwind Difference Scheme</b>
		
<b>Bounded Downwind Scheme</b>	<b>Central Difference Scheme</b>	<b>MUSCL</b>
		
<b>SUPERBEE</b>	<b>Modified MUSCL</b>	<b>Modified BDS</b>
<b>Co=0.75</b>		
		
<b>Upwind Difference Scheme</b>	<b>Cubic Upwind Scheme</b>	<b>Downwind Difference Scheme</b>
		
<b>Bounded Downwind Scheme</b>	<b>Central Difference Scheme</b>	<b>MUSCL</b>
		
<b>SUPERBEE</b>	<b>Modified MUSCL</b>	<b>Modified BDS</b>

Figure 5.6 The final shape of hollow circle from different schemes in triangular mesh

<b>Co=0.25</b>		
		
<b>Upwind Difference Scheme</b>	<b>Cubic Upwind Scheme</b>	<b>Downwind Difference Scheme</b>
		
<b>Bounded Downwind Scheme</b>	<b>Central Difference Scheme</b>	<b>MUSCL</b>
		
<b>SUPERBEE</b>	<b>Modified MUSCL</b>	<b>Modified BDS</b>
<b>Co=0.75</b>		
		
<b>Upwind Difference Scheme</b>	<b>Cubic Upwind Scheme</b>	<b>Downwind Difference Scheme</b>
		
<b>Bounded Downwind Scheme</b>	<b>Central Difference Scheme</b>	<b>MUSCL</b>
		
<b>SUPERBEE</b>	<b>Modified MUSCL</b>	<b>Modified BDS</b>

Figure 5.7 The final shape of hollow square from different schemes in triangular mesh

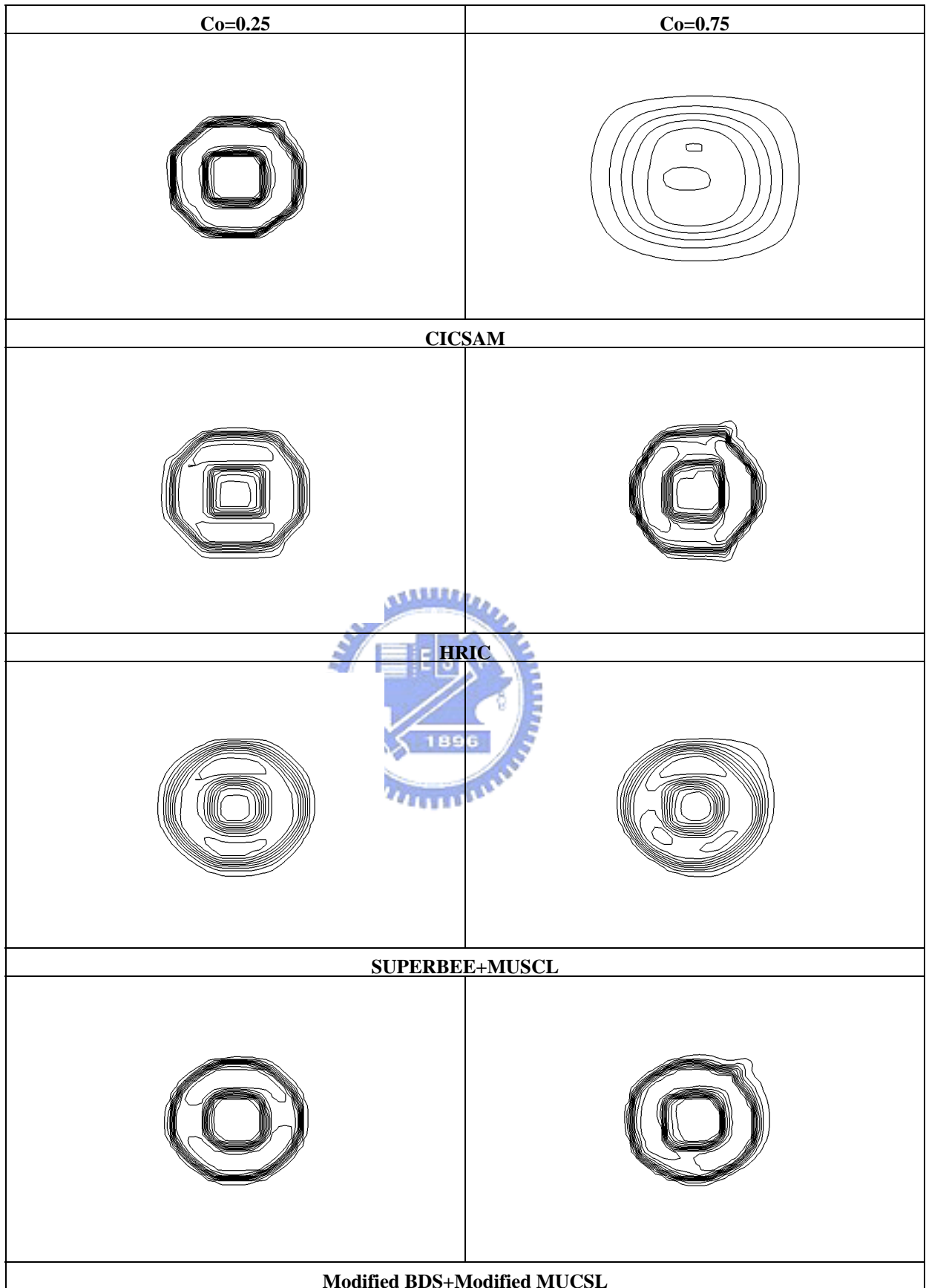


Figure 5.8 The final shape of hollow circle from different composite schemes in quadrilateral mesh

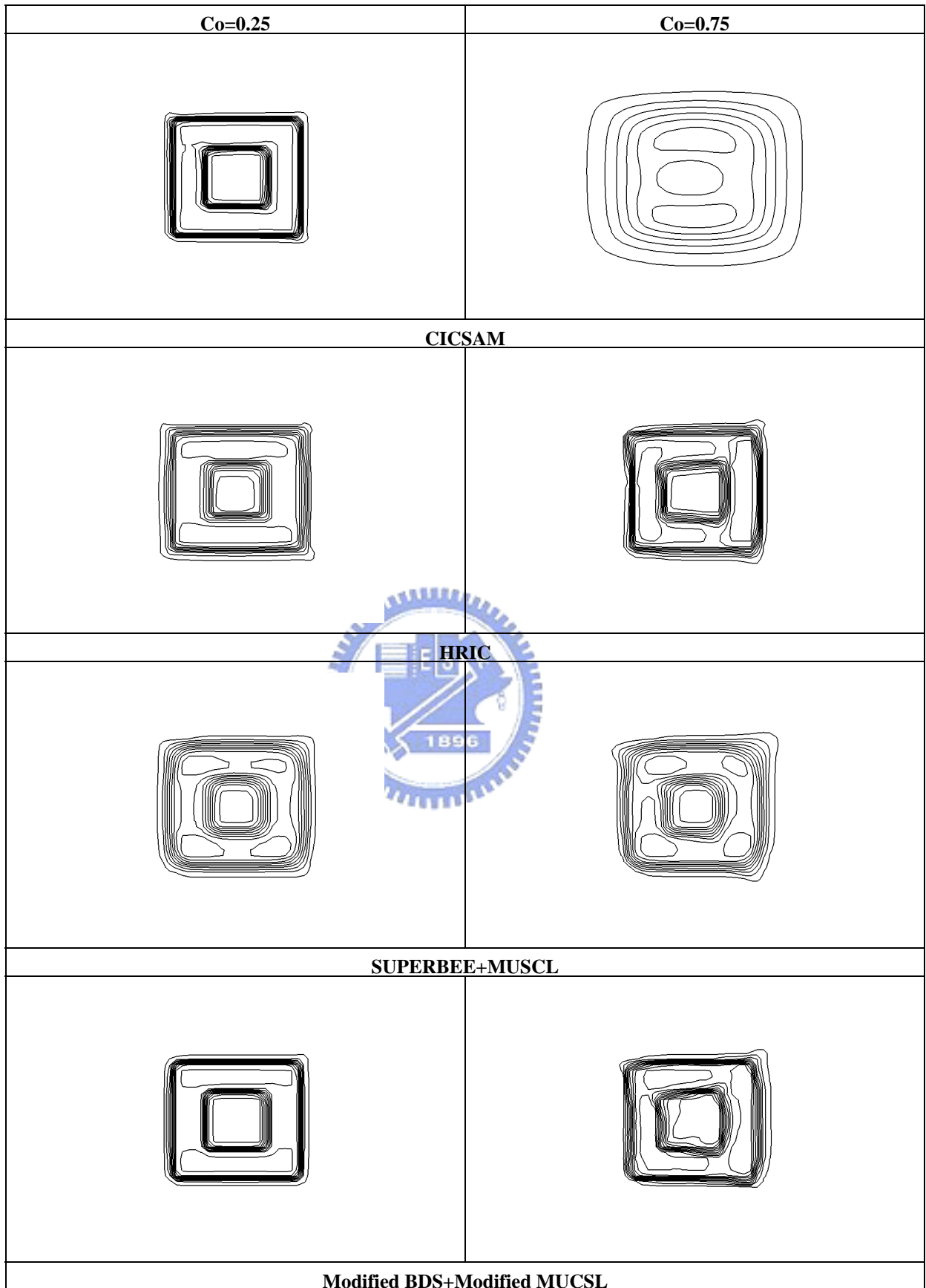


Figure 5.9 The final shape of hollow square from different composite scheme in quadrilateral mesh



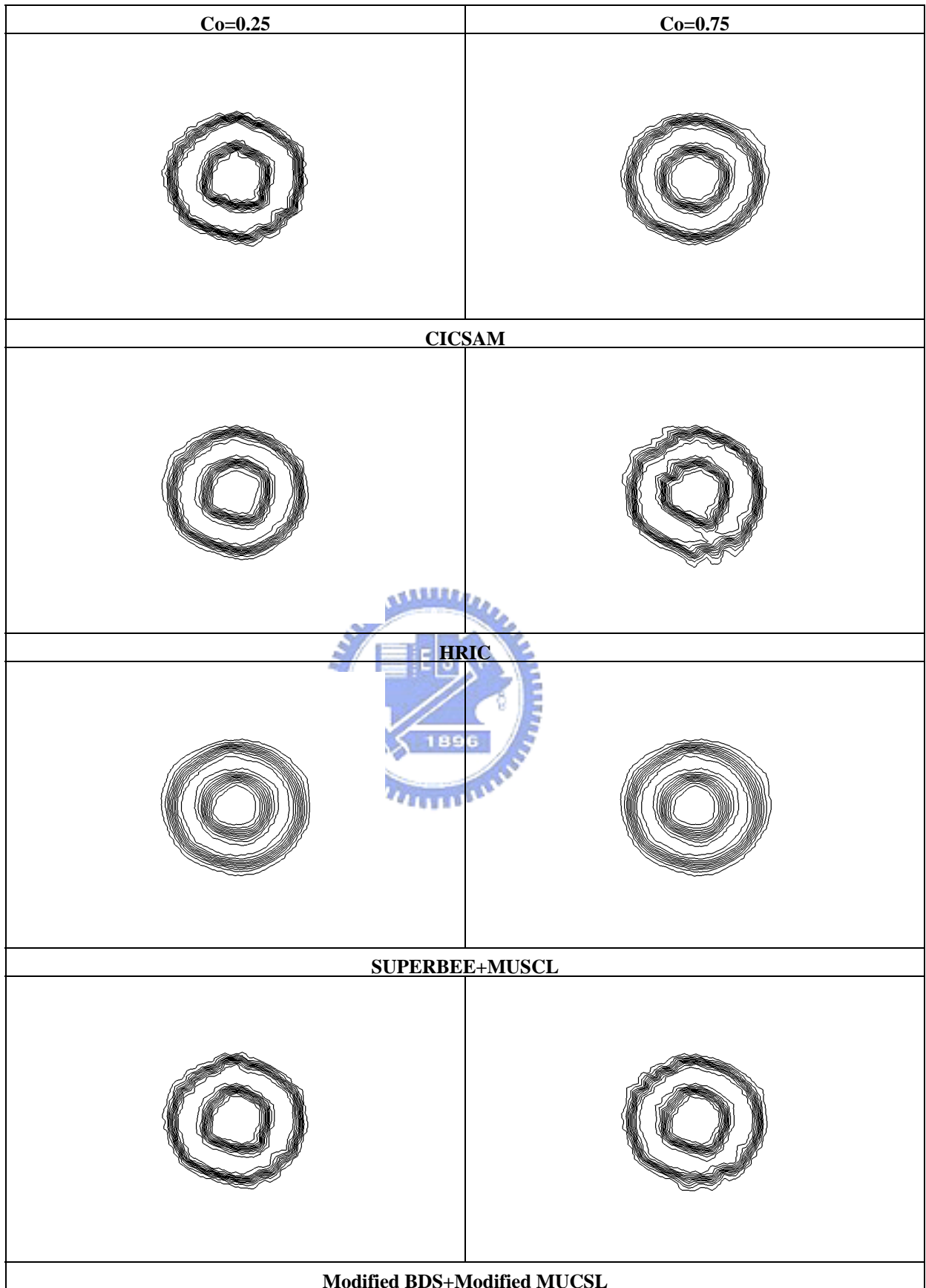


Figure 5.10 The final shape of hollow circle from different composite scheme in triangular mesh

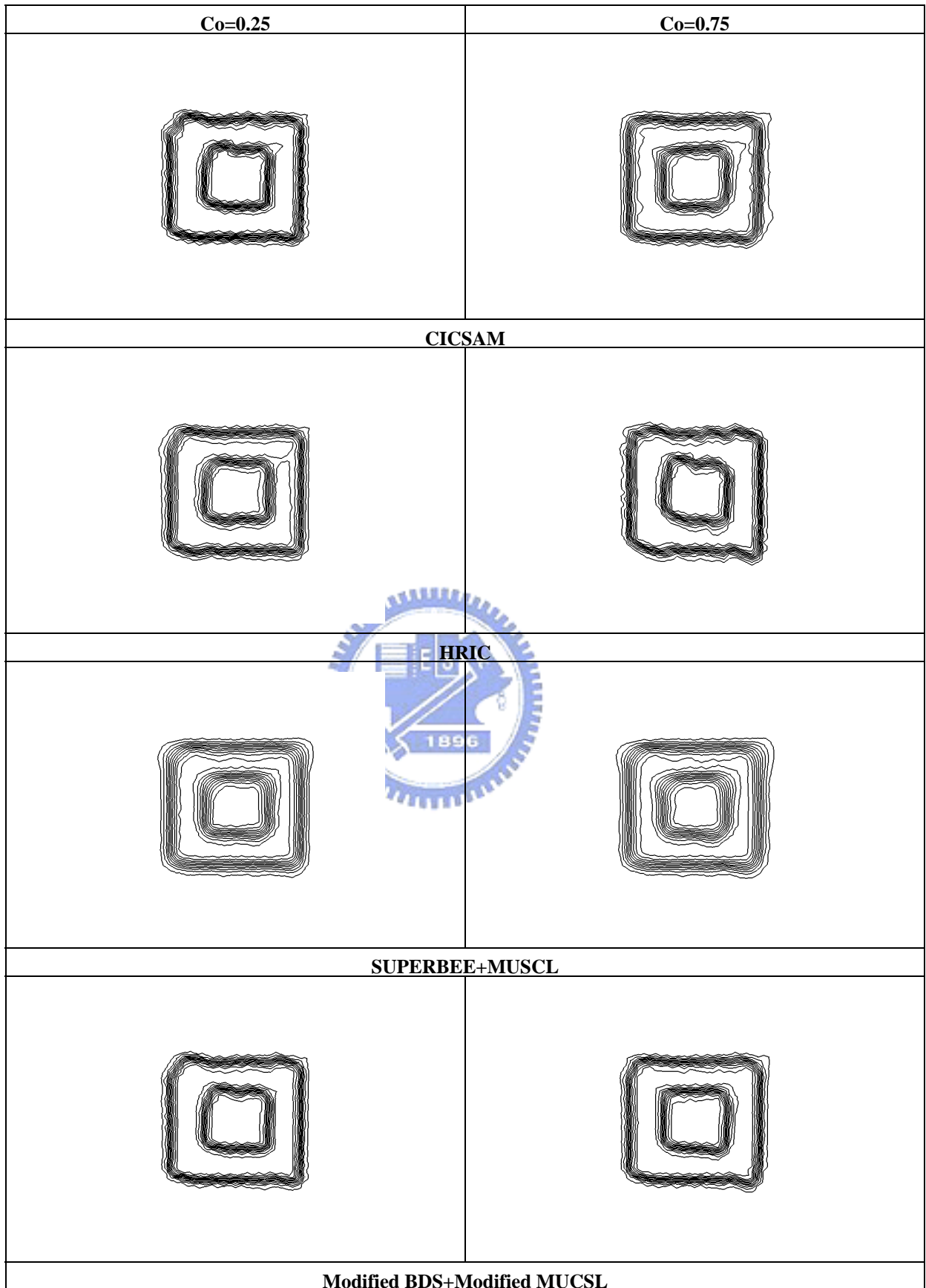


Figure 5.11 The final shape of hollow square from different composite scheme in triangular mesh

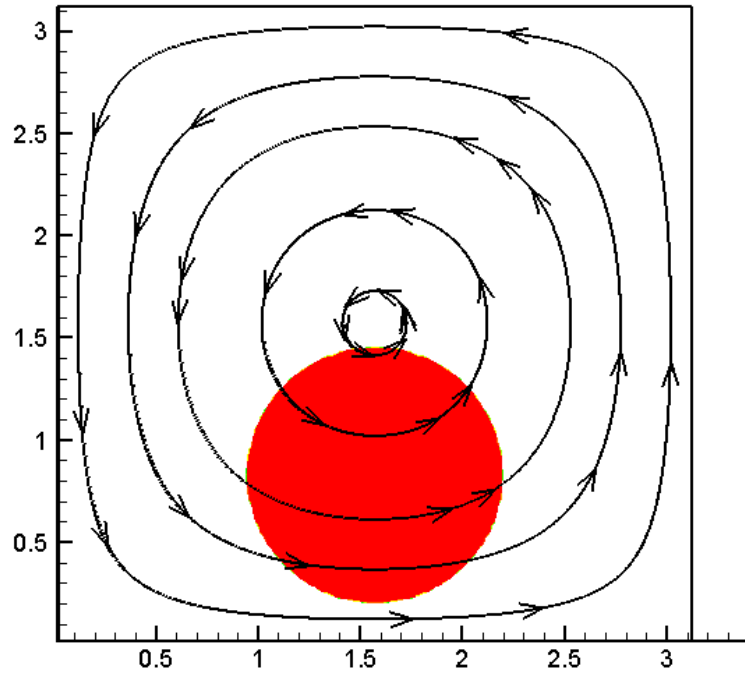


Figure 5.12 The volume fraction distribution in a shear flow field

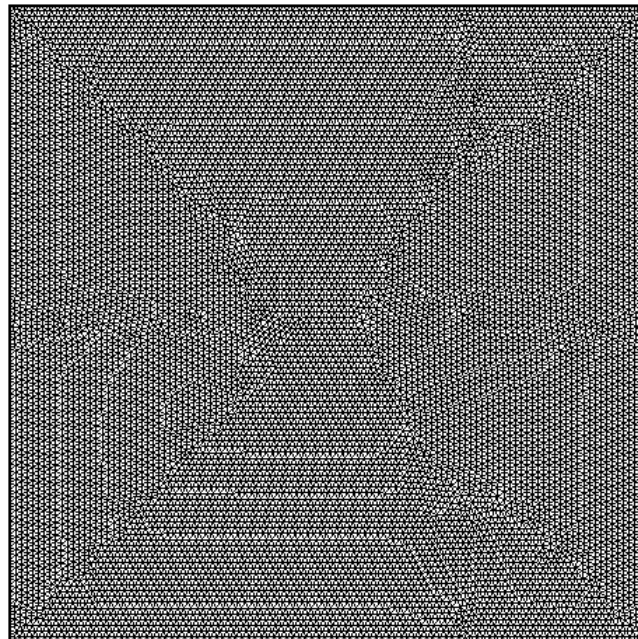


Figure 5.13 Triangular mesh in uniform density flow (22494 cells)

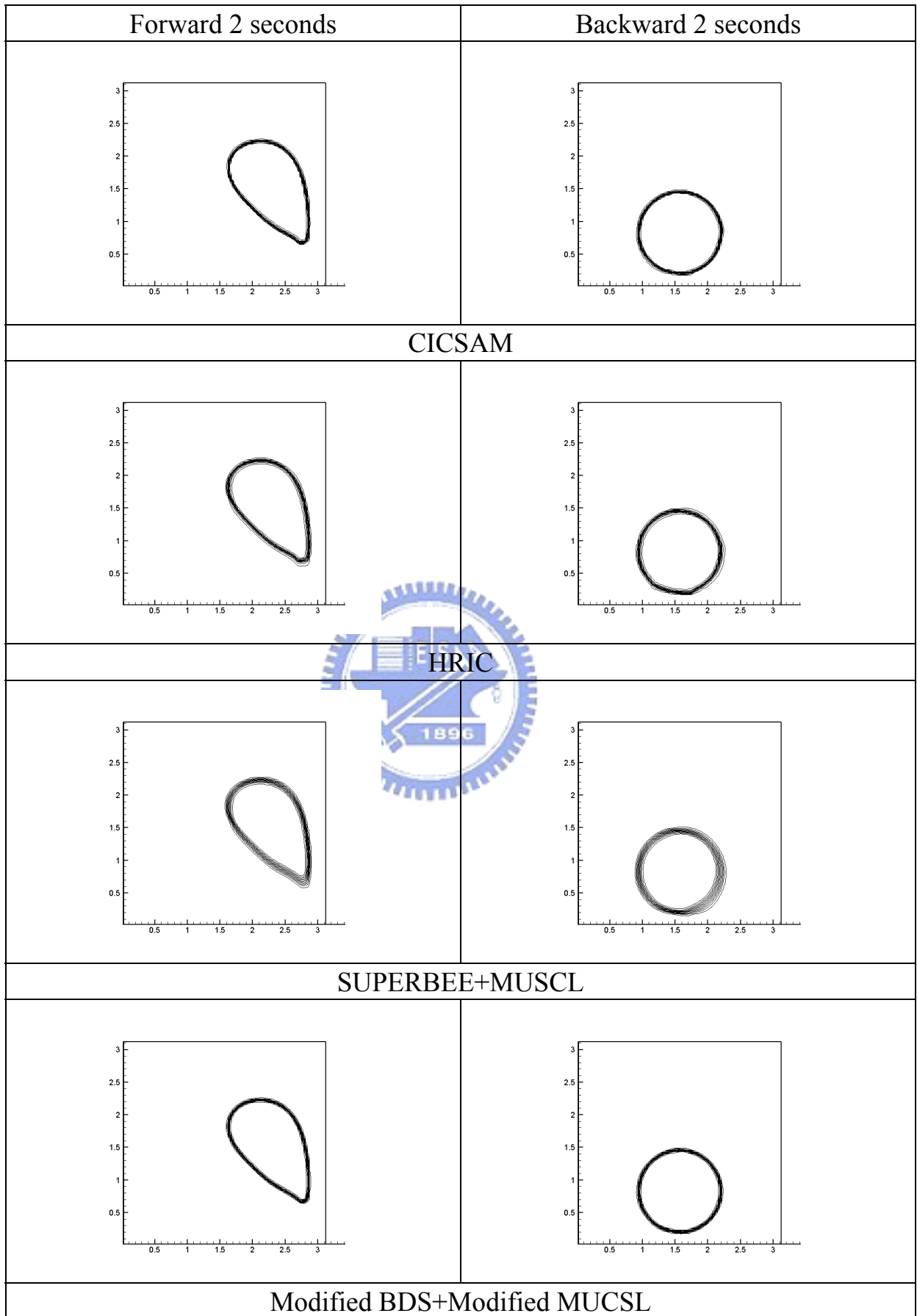


Figure 5.14 The volume fraction distribution in shear flow with  $Co=0.25$  (quadrilateral mesh)

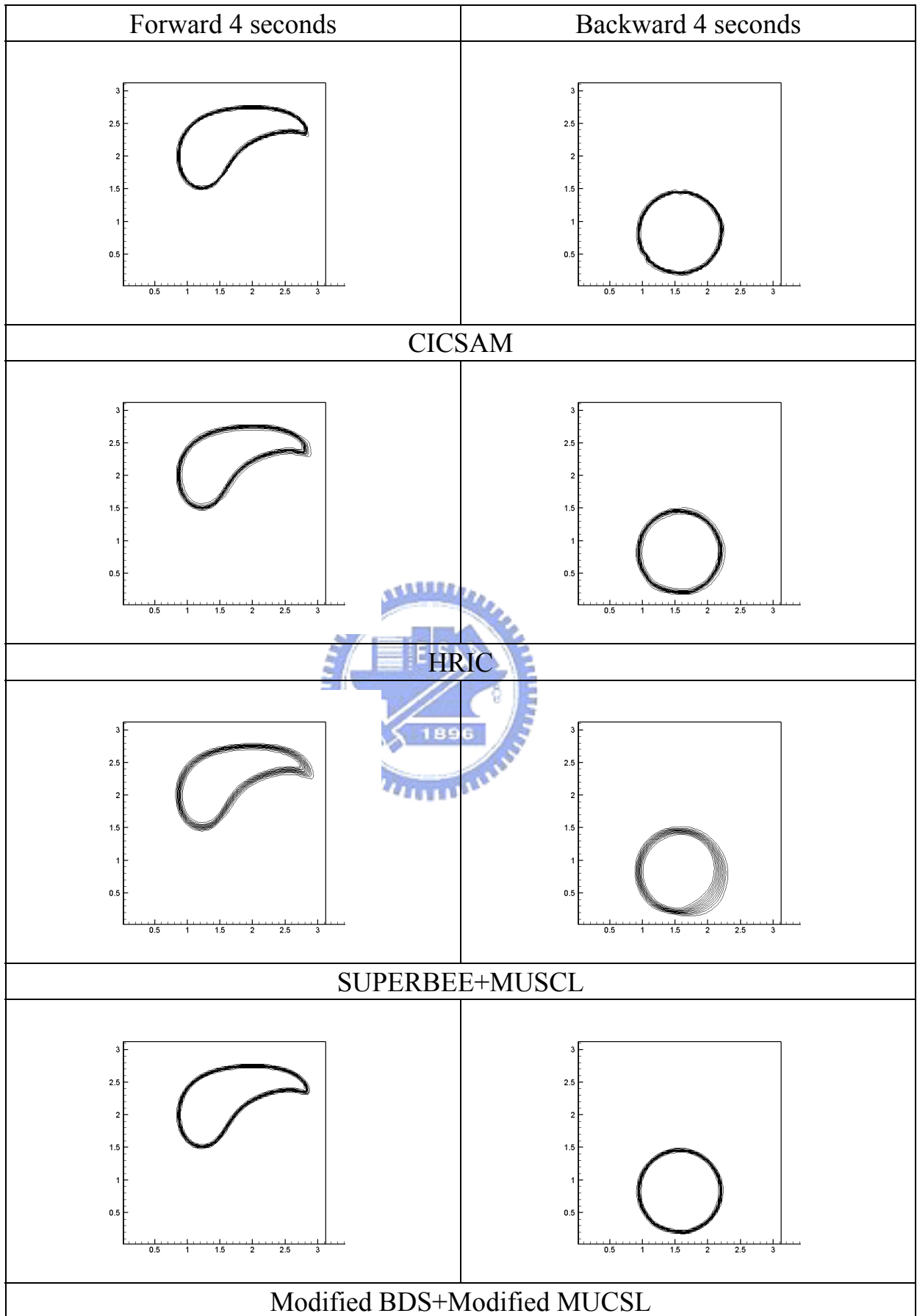


Figure 5.15 The volume fraction distribution in shear flow with  $Co=0.25$  (quadrilateral mesh)

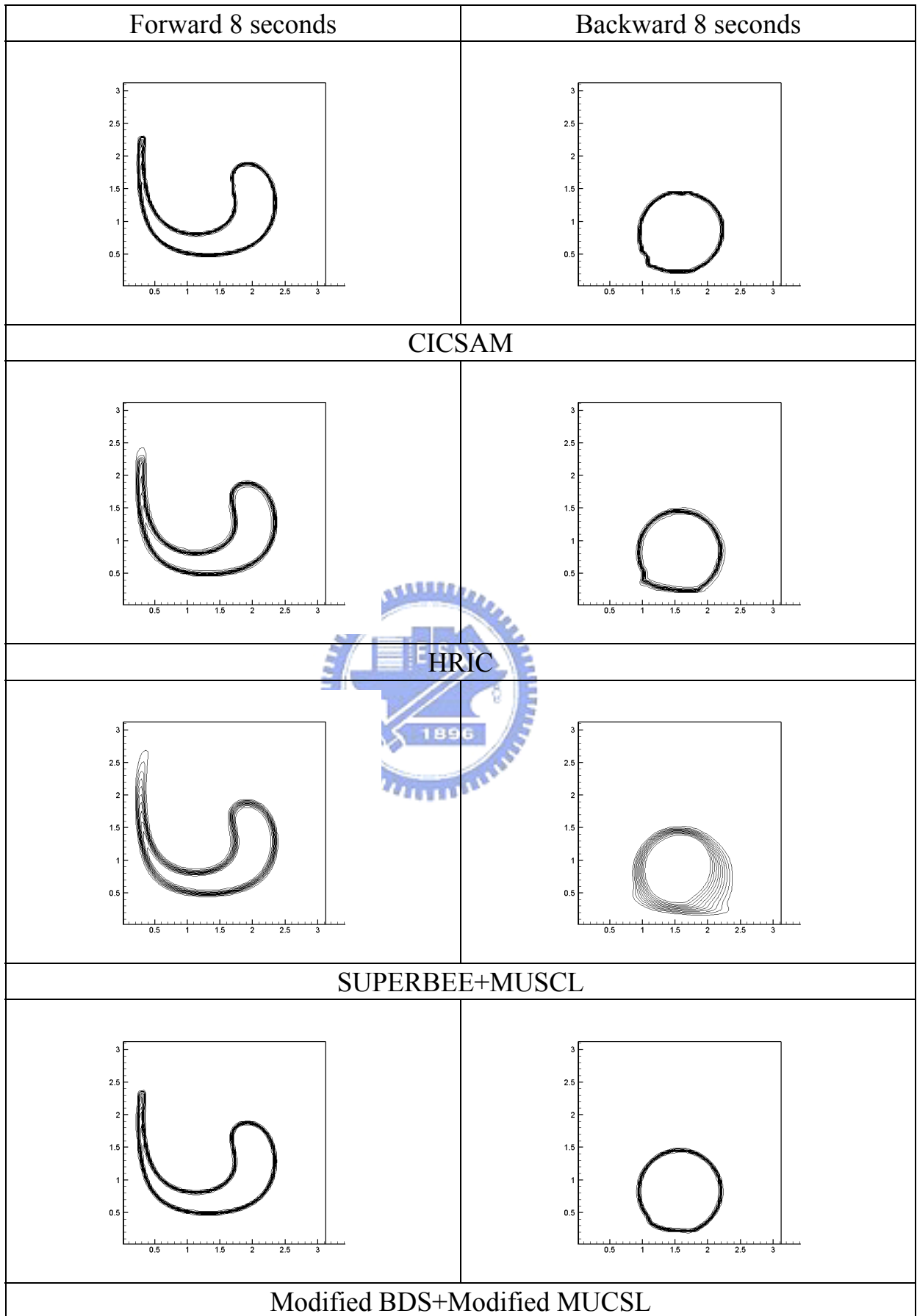


Figure 5.16 The volume fraction distribution in shear flow with  $Co=0.25$  (quadrilateral mesh)

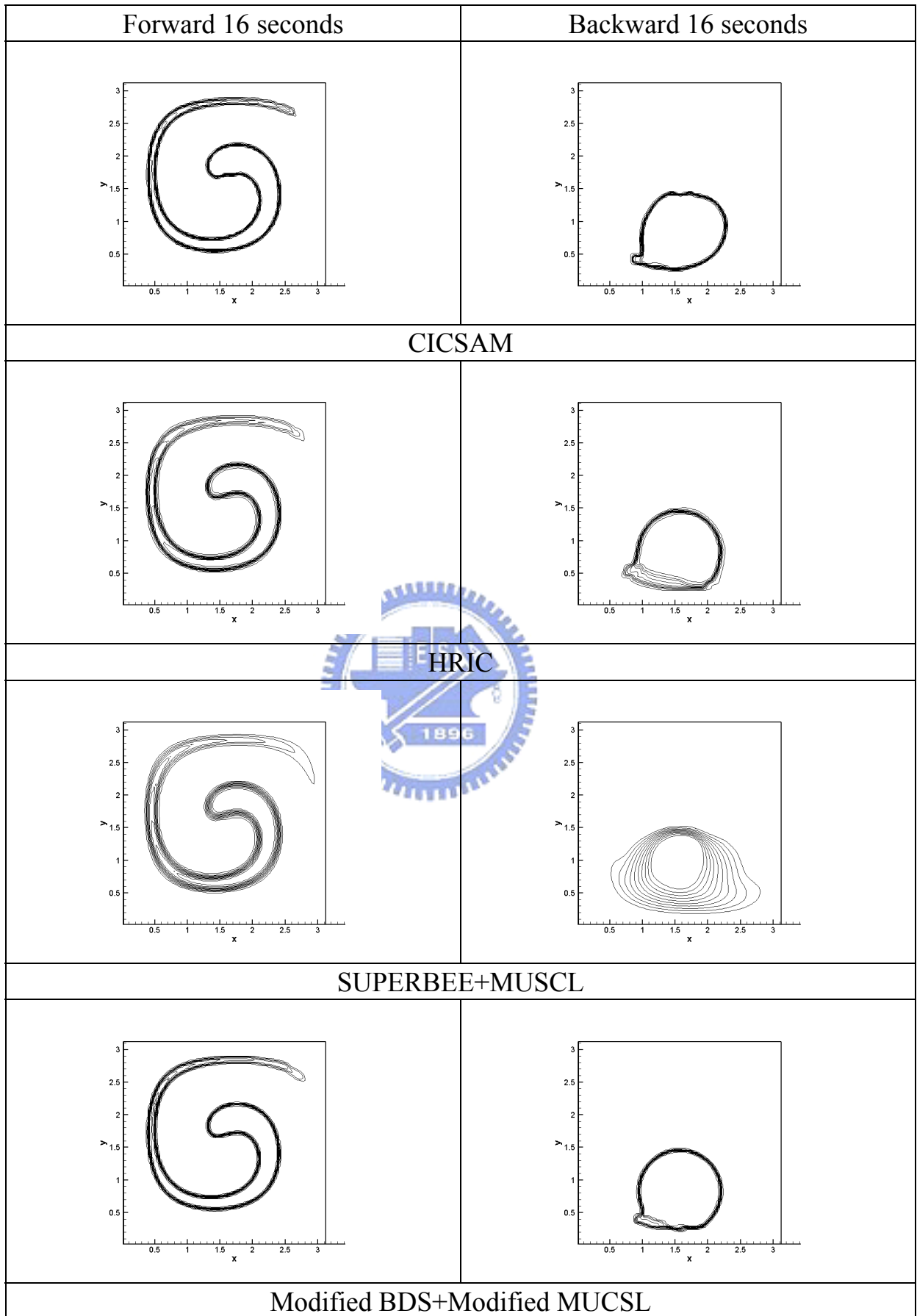


Figure 5.17 The volume fraction distribution in shear flow with  $Co=0.25$  (quadrilateral mesh)

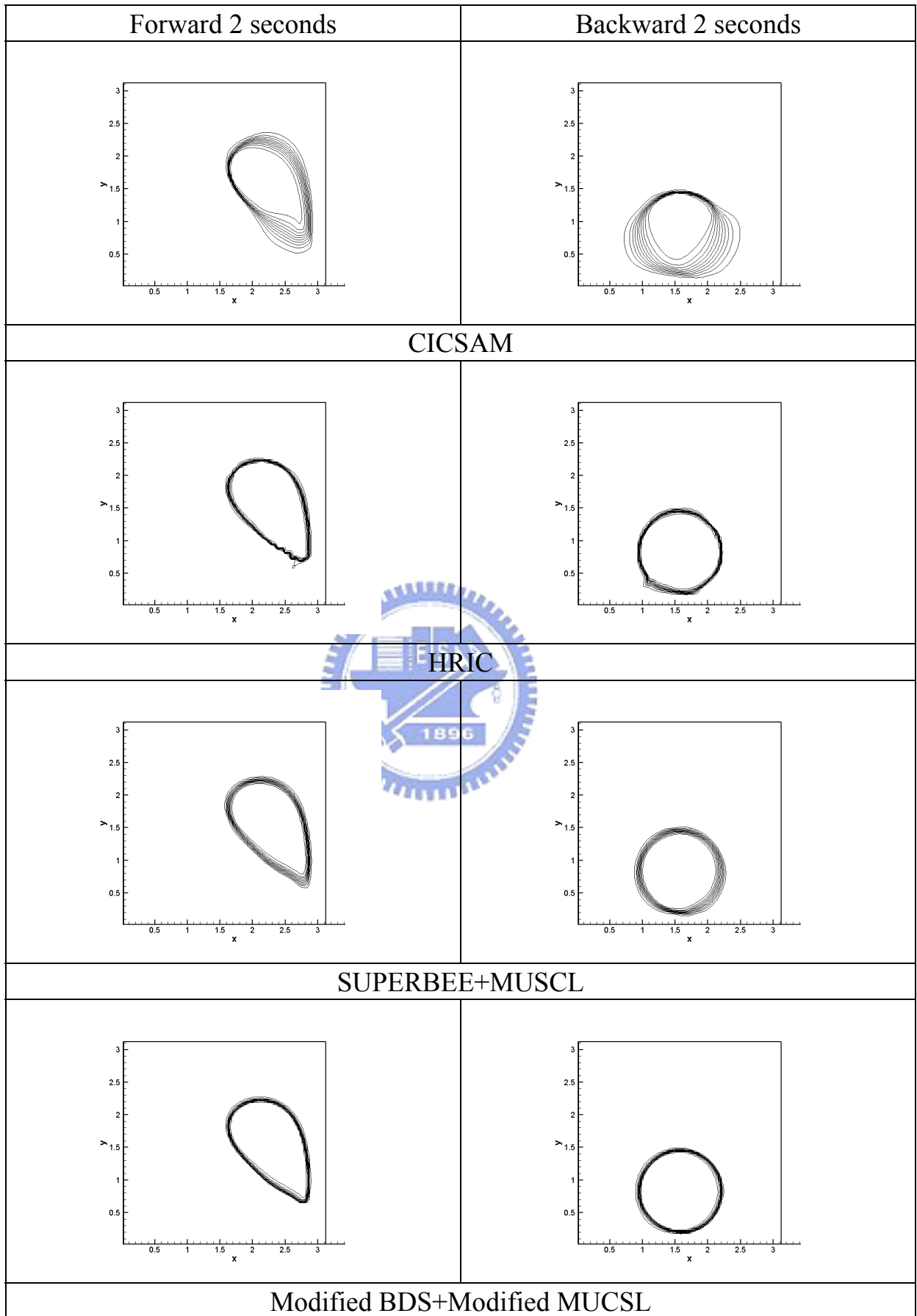


Figure 5.18 The volume fraction distribution in shear flow with  $Co=0.75$  (quadrilateral mesh)



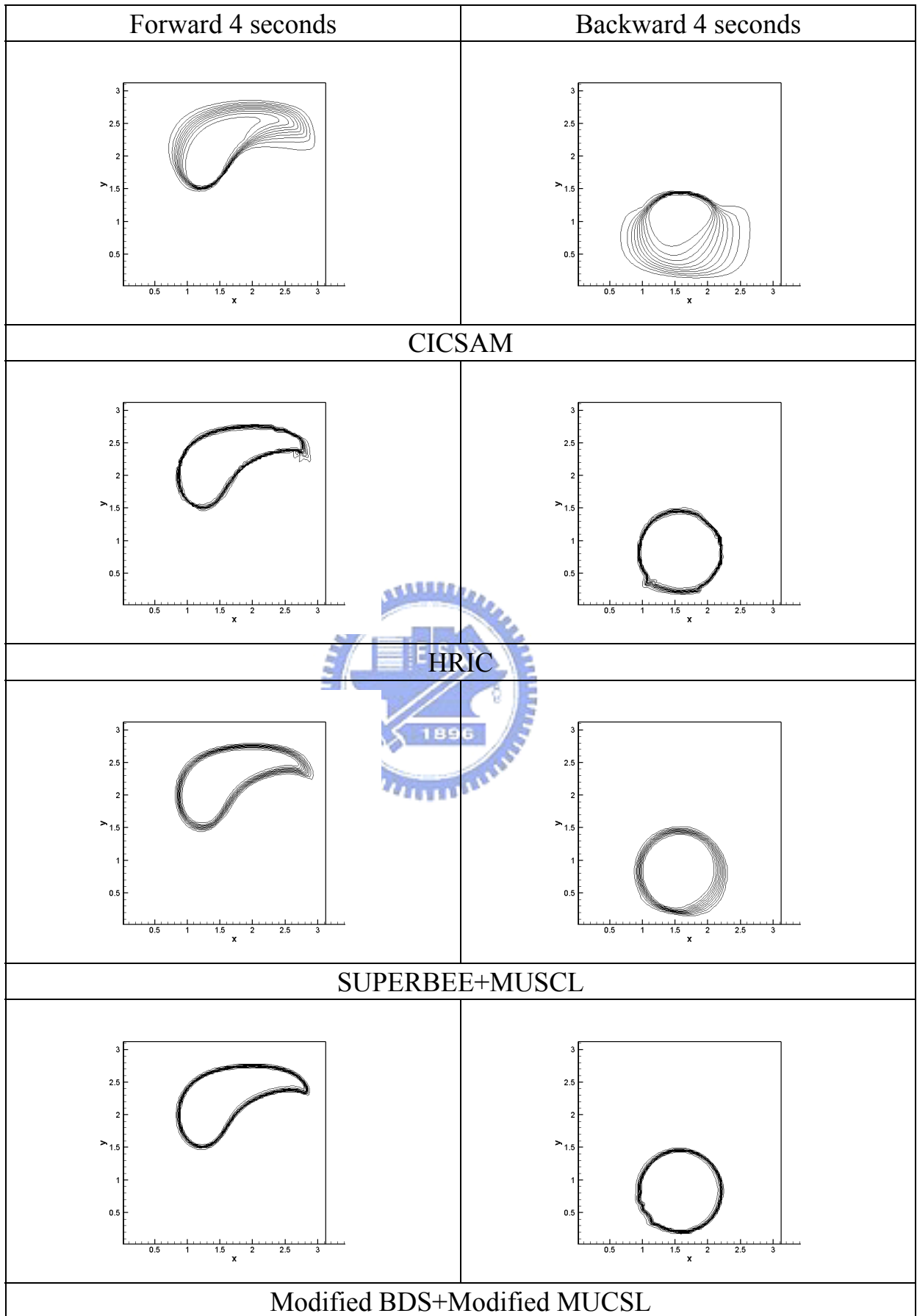


Figure 5.19 The volume fraction distribution in shear flow with  $Co=0.75$  (quadrilateral mesh)

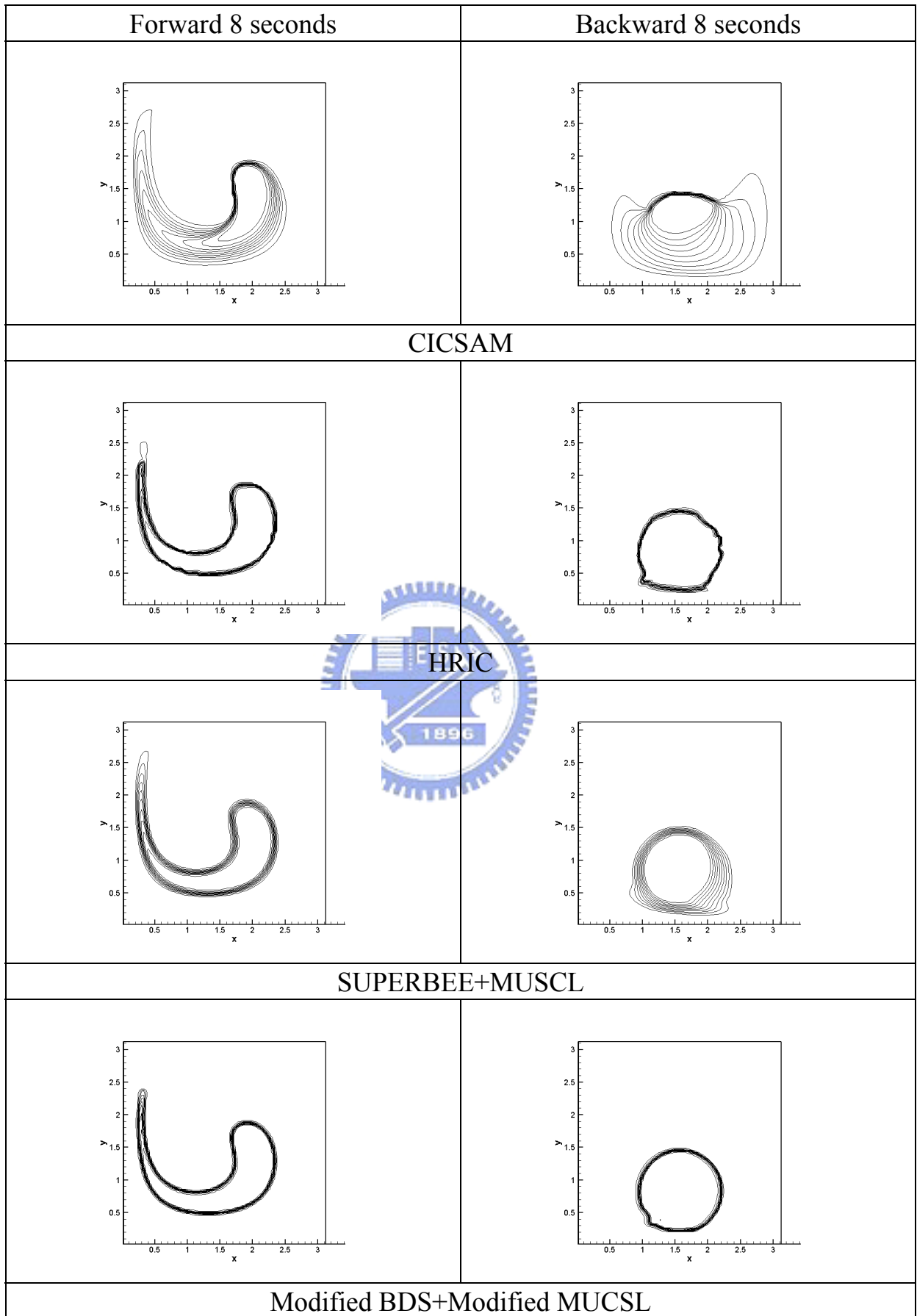


Figure 5.20 The volume fraction distribution in shear flow with  $Co=0.75$  (quadrilateral mesh)

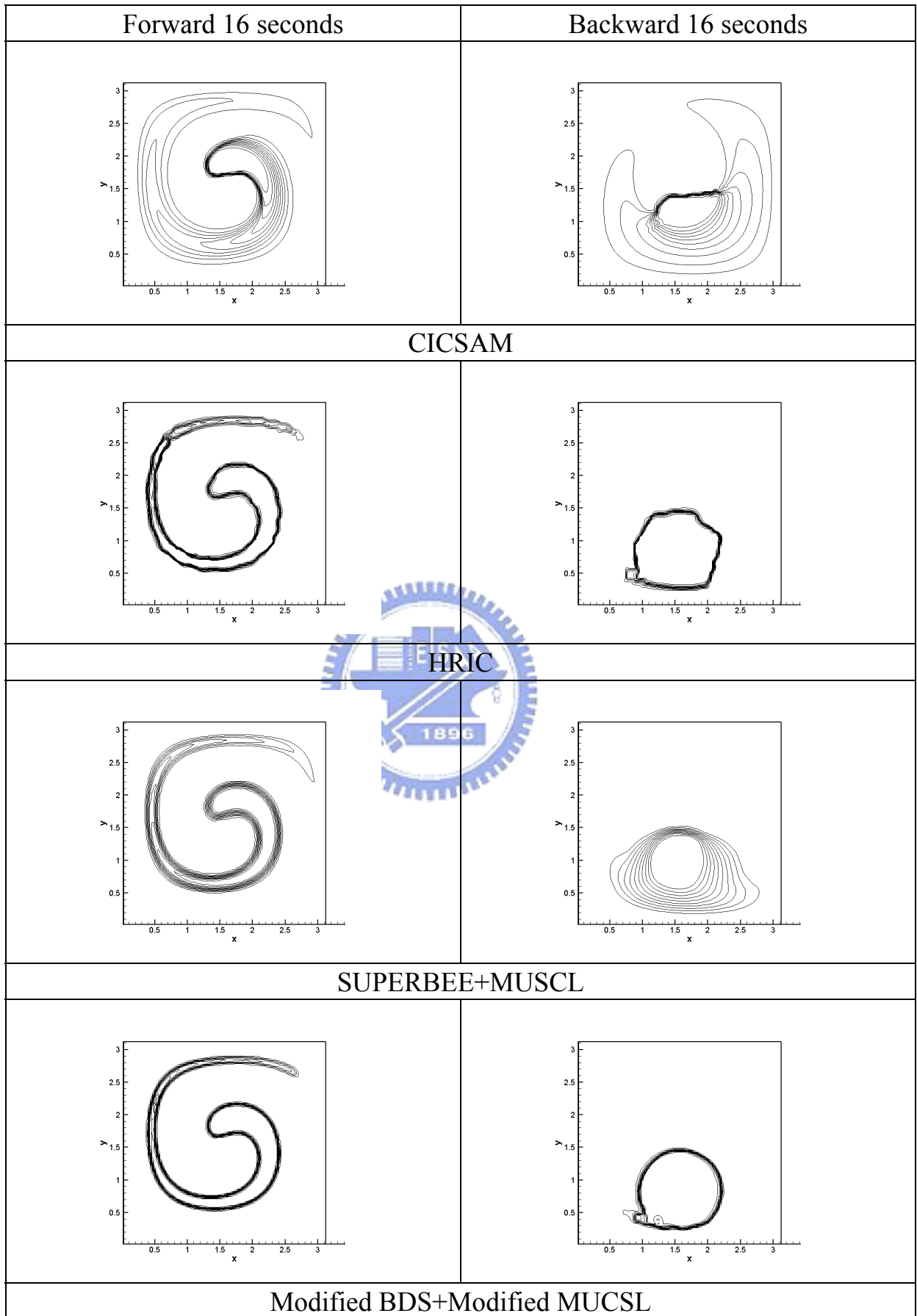


Figure 5.21 The volume fraction distribution in shear flow with  $Co=0.75$  (quadrilateral mesh)

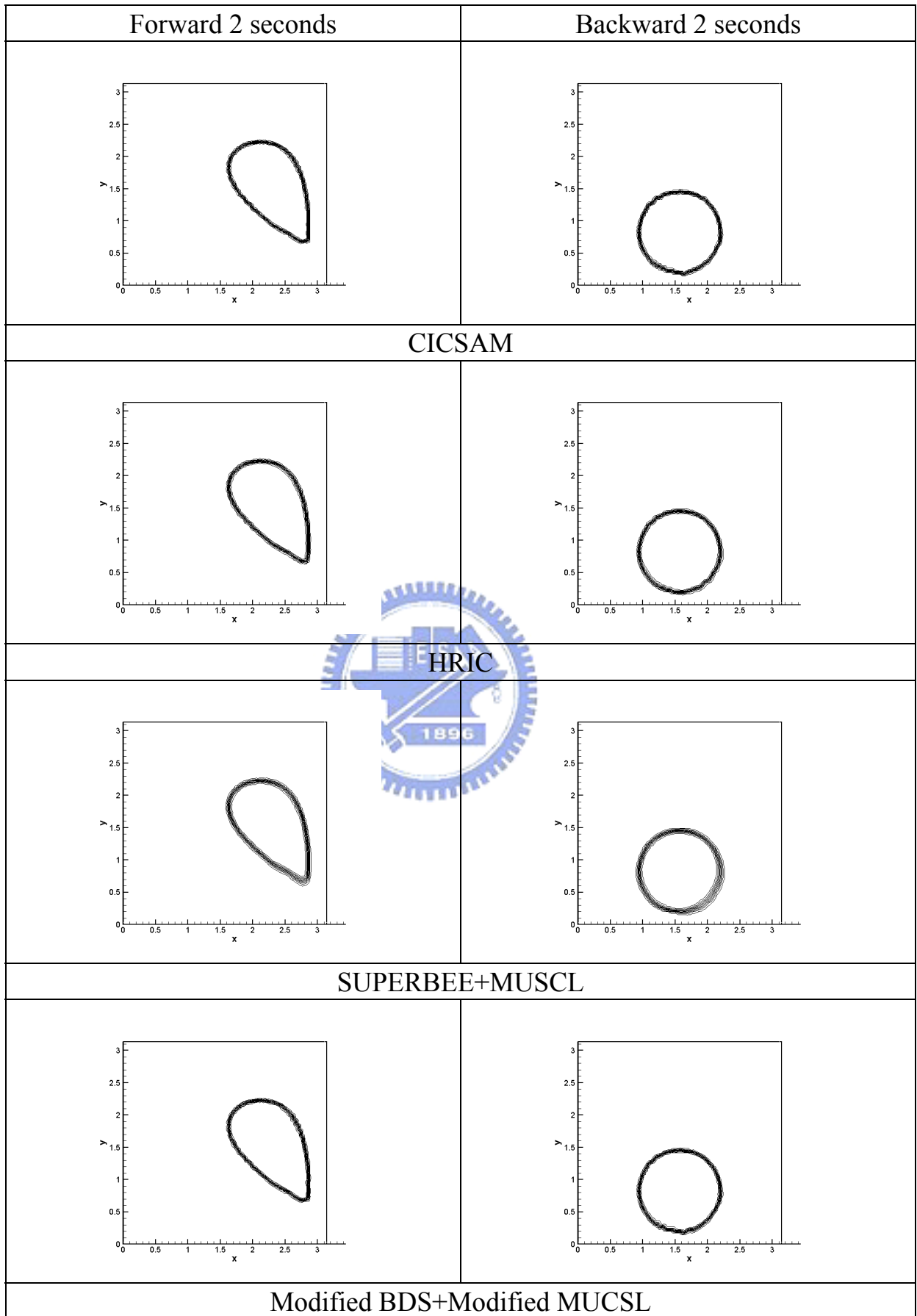


Figure 5.22 The volume fraction distribution in shear flow with  $Co=0.25$  (triangular mesh)

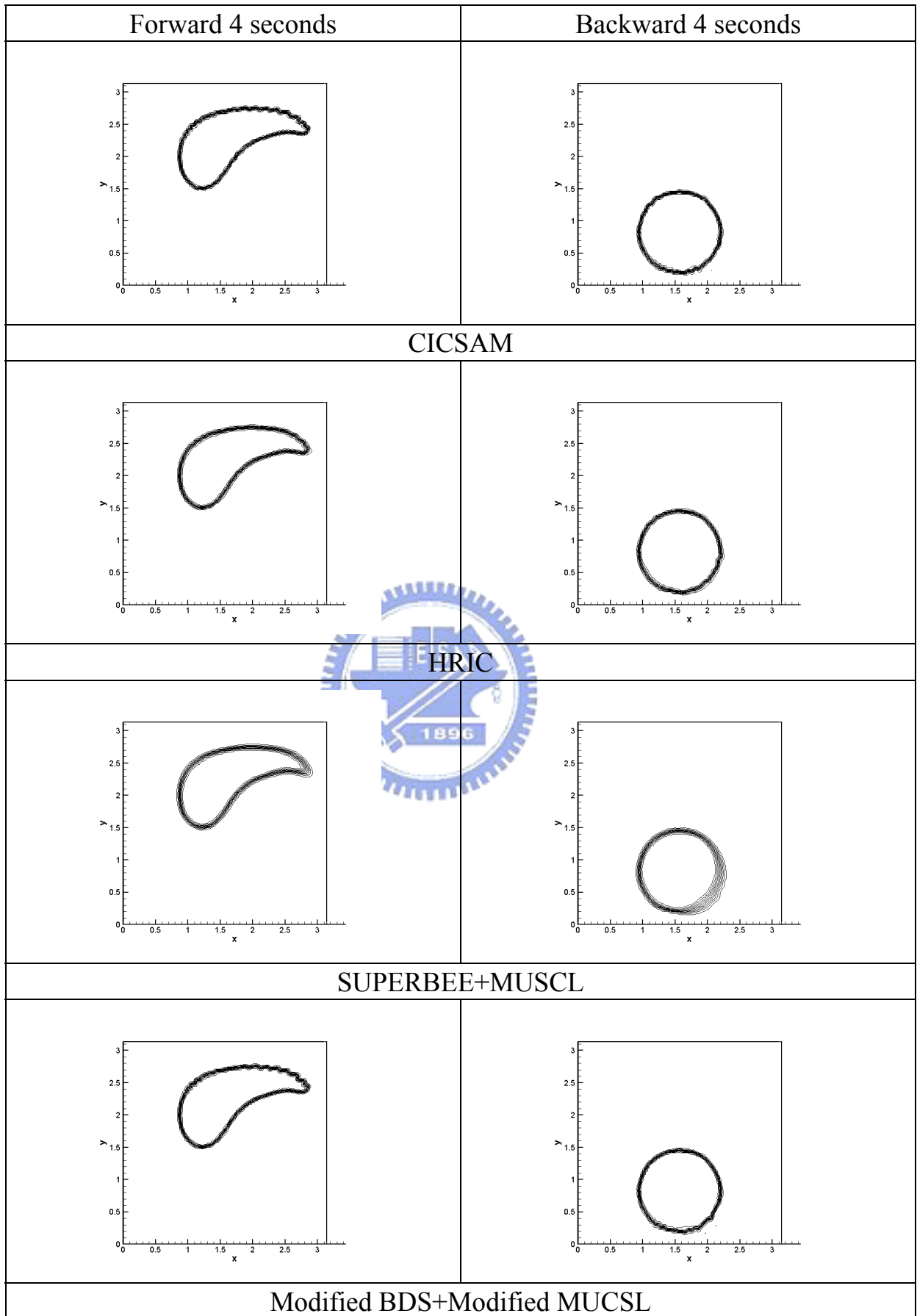


Figure 5.23 The volume fraction distribution in shear flow with  $Co=0.25$  (triangular mesh)

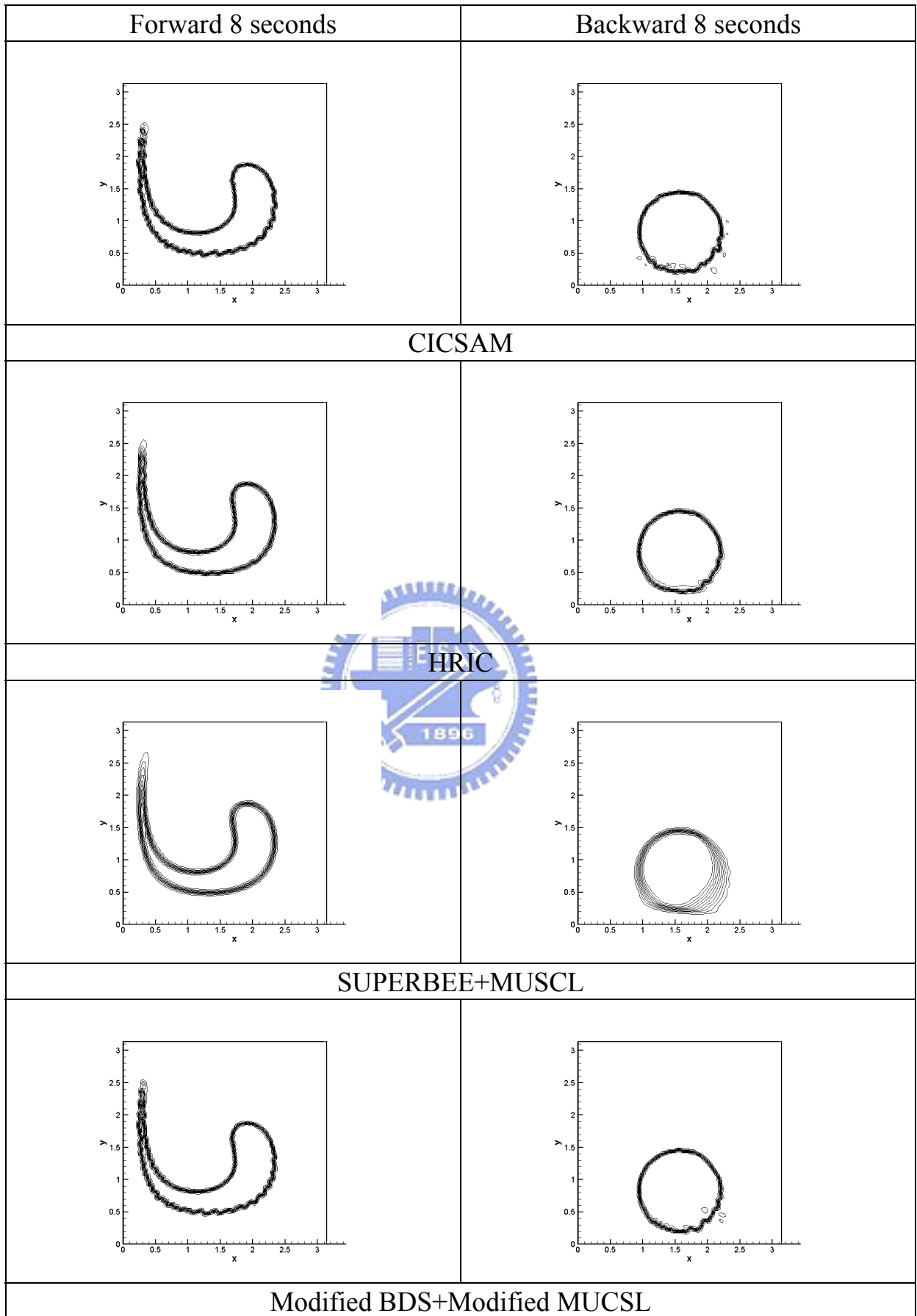


Figure 5.24 The volume fraction distribution in shear flow with  $Co=0.25$  (triangular mesh)

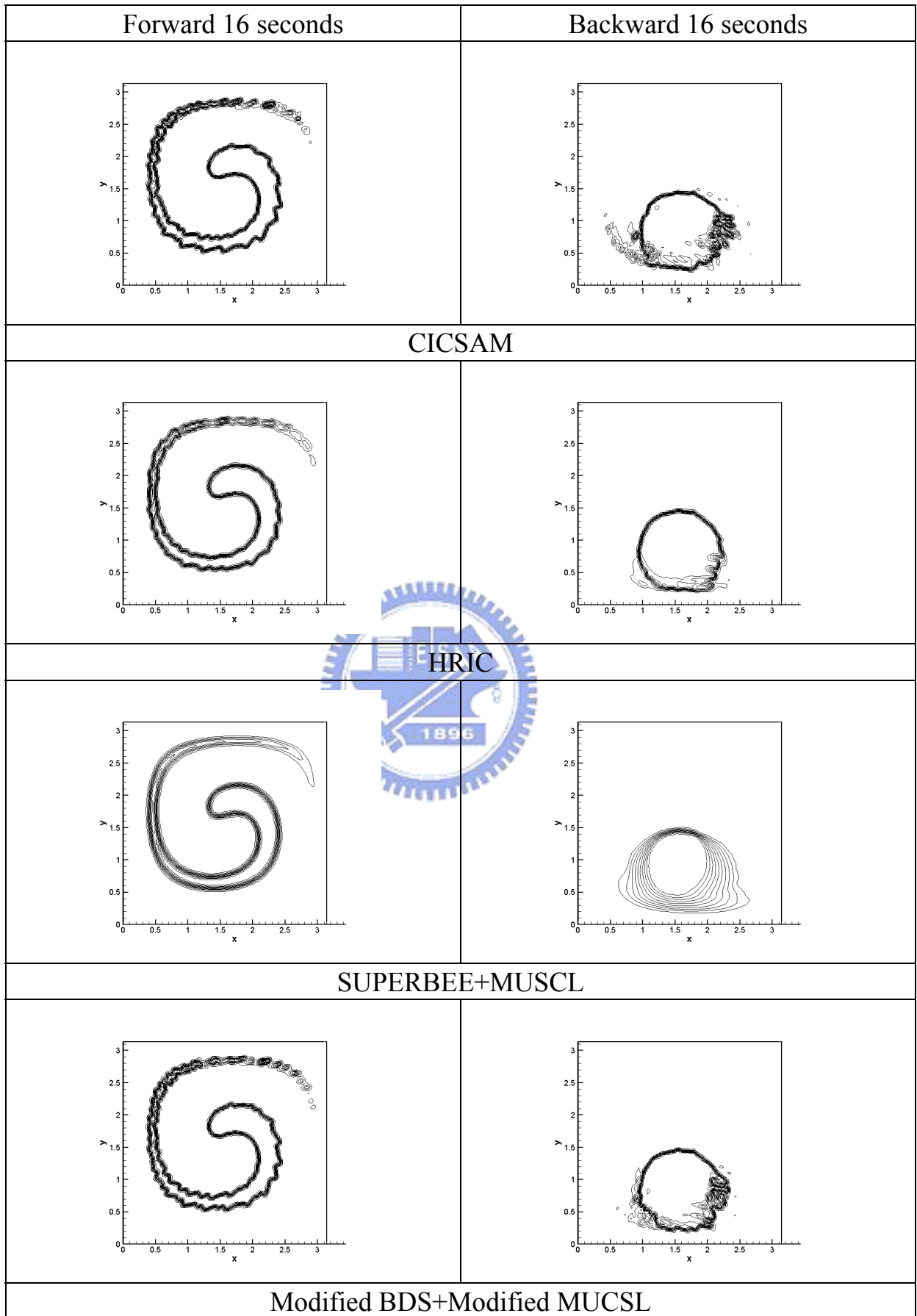


Figure 5.25 The volume fraction distribution in shear flow with  $Co=0.25$  (triangular mesh)

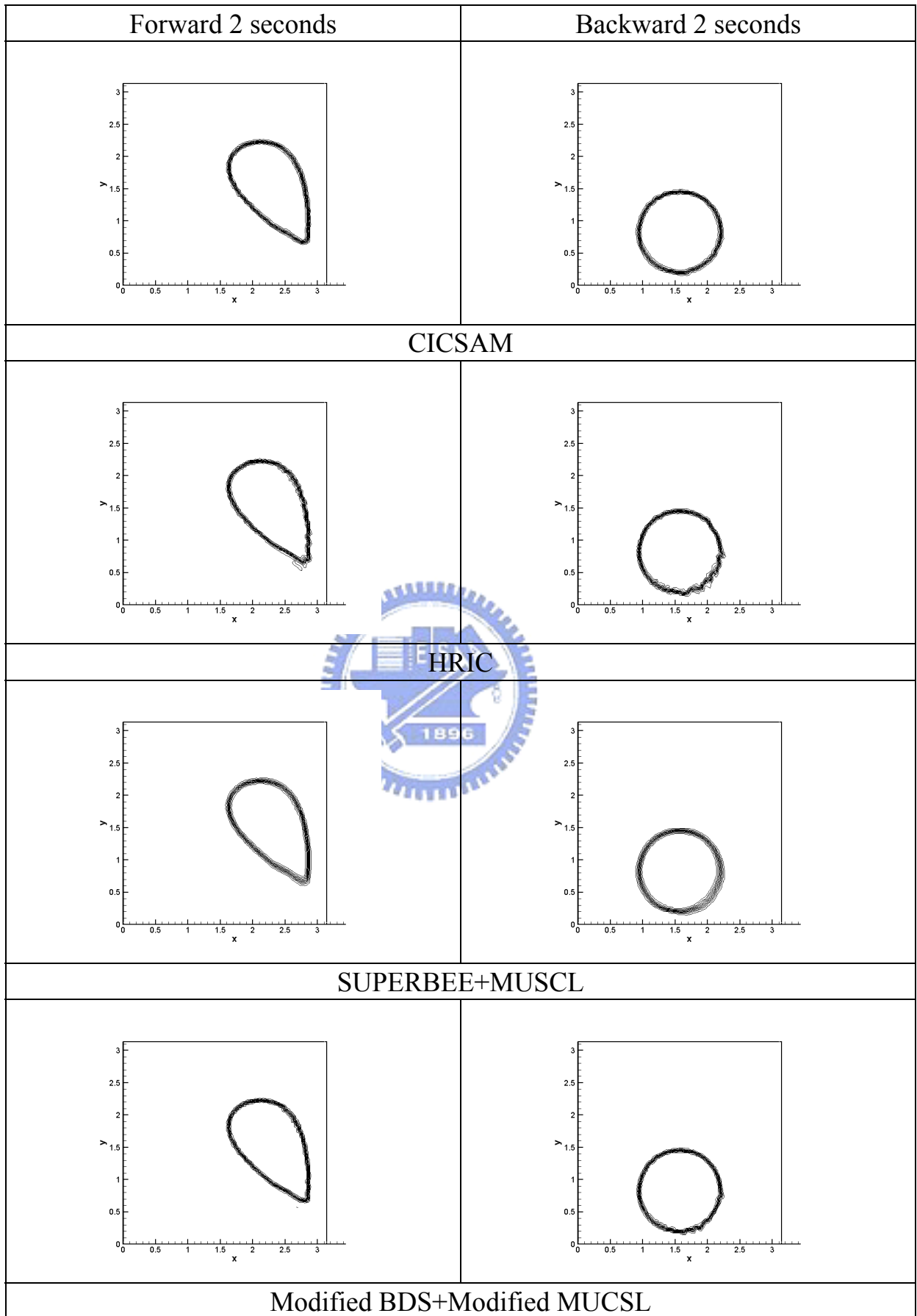


Figure 5.26 The volume fraction distribution in shear flow with  $Co=0.75$  (triangular mesh)



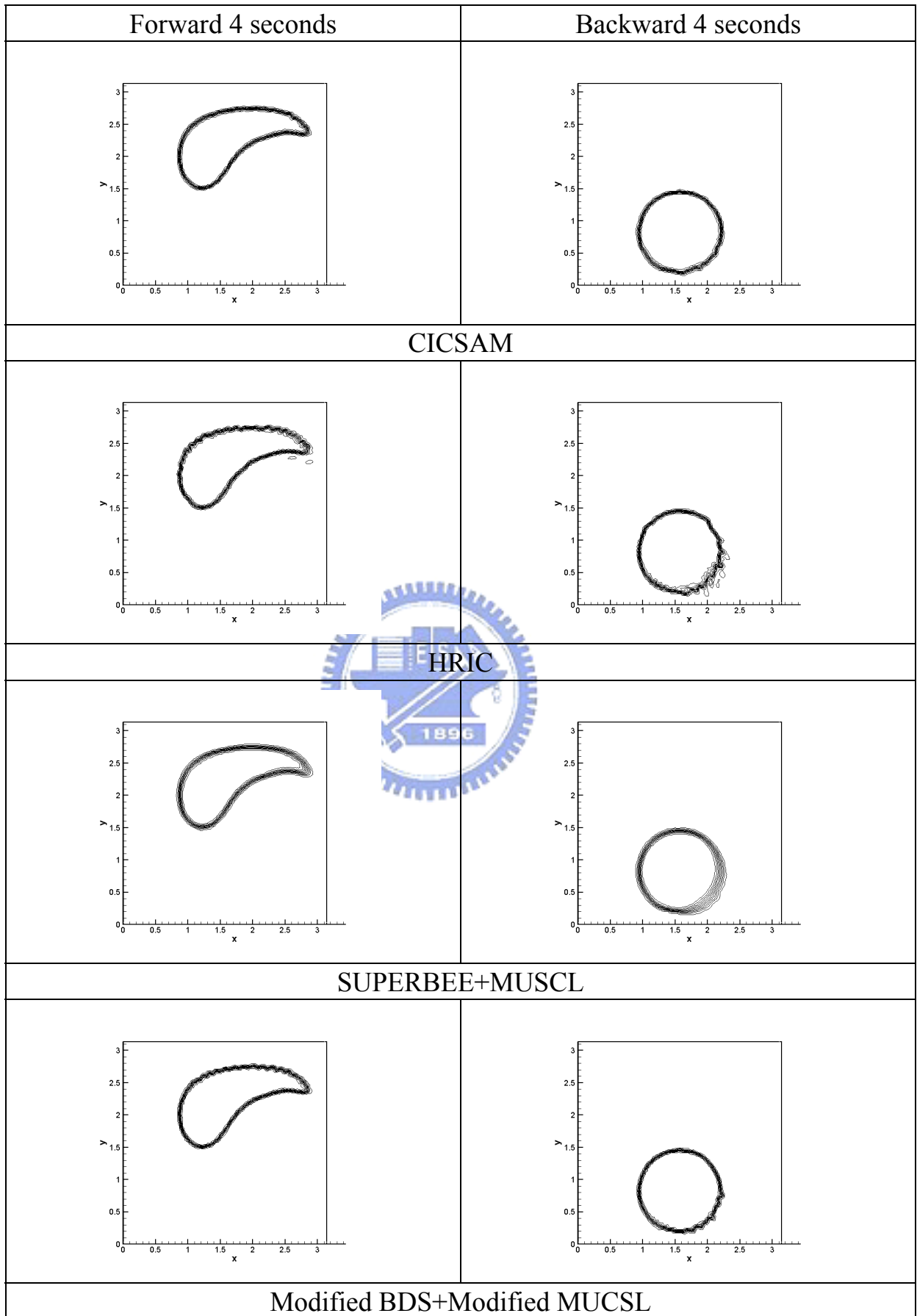


Figure 5.27 The volume fraction distribution in shear flow with  $Co=0.75$  (triangular mesh)

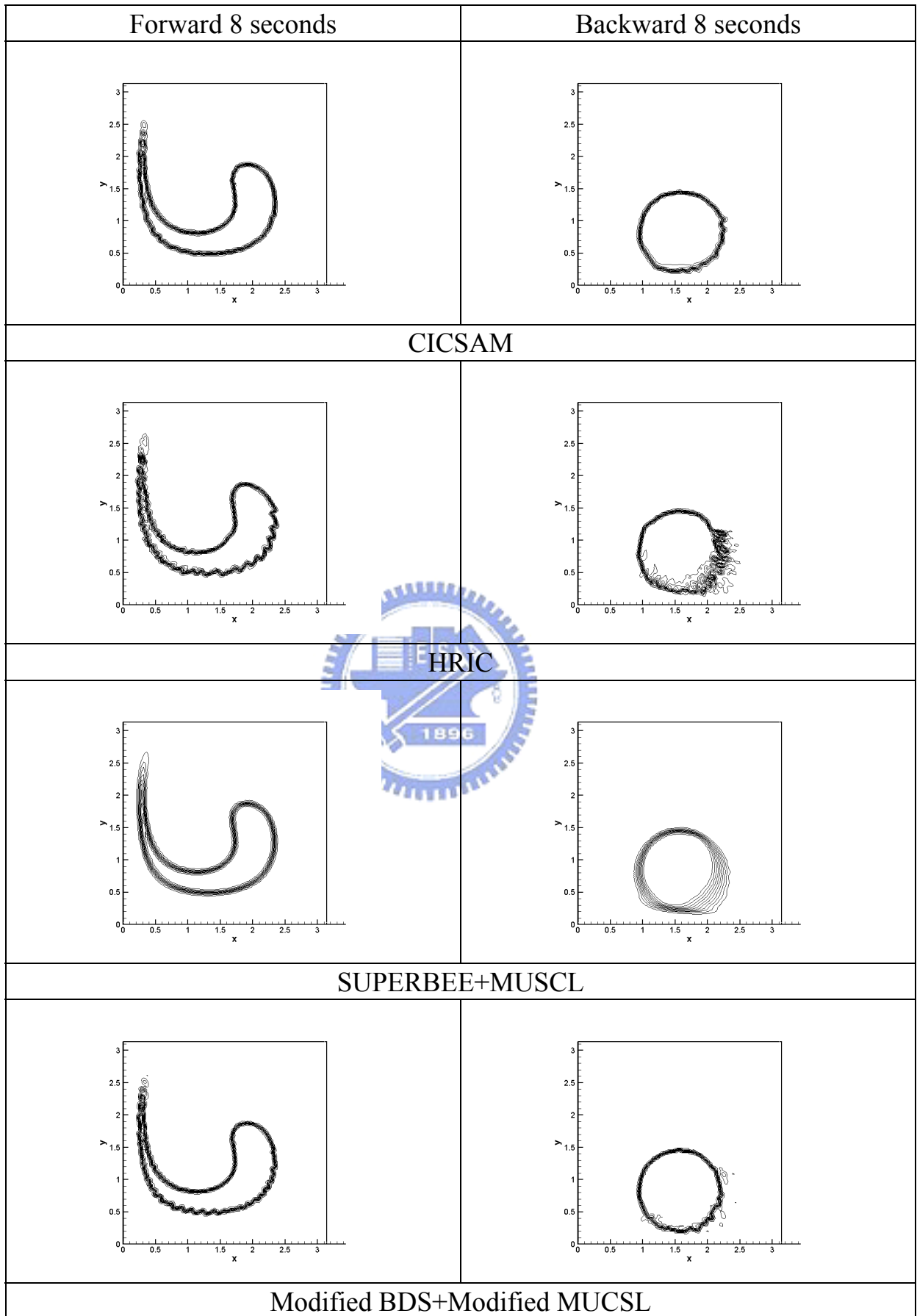


Figure 5.28 The volume fraction distribution in shear flow with  $Co=0.75$  (triangular mesh)

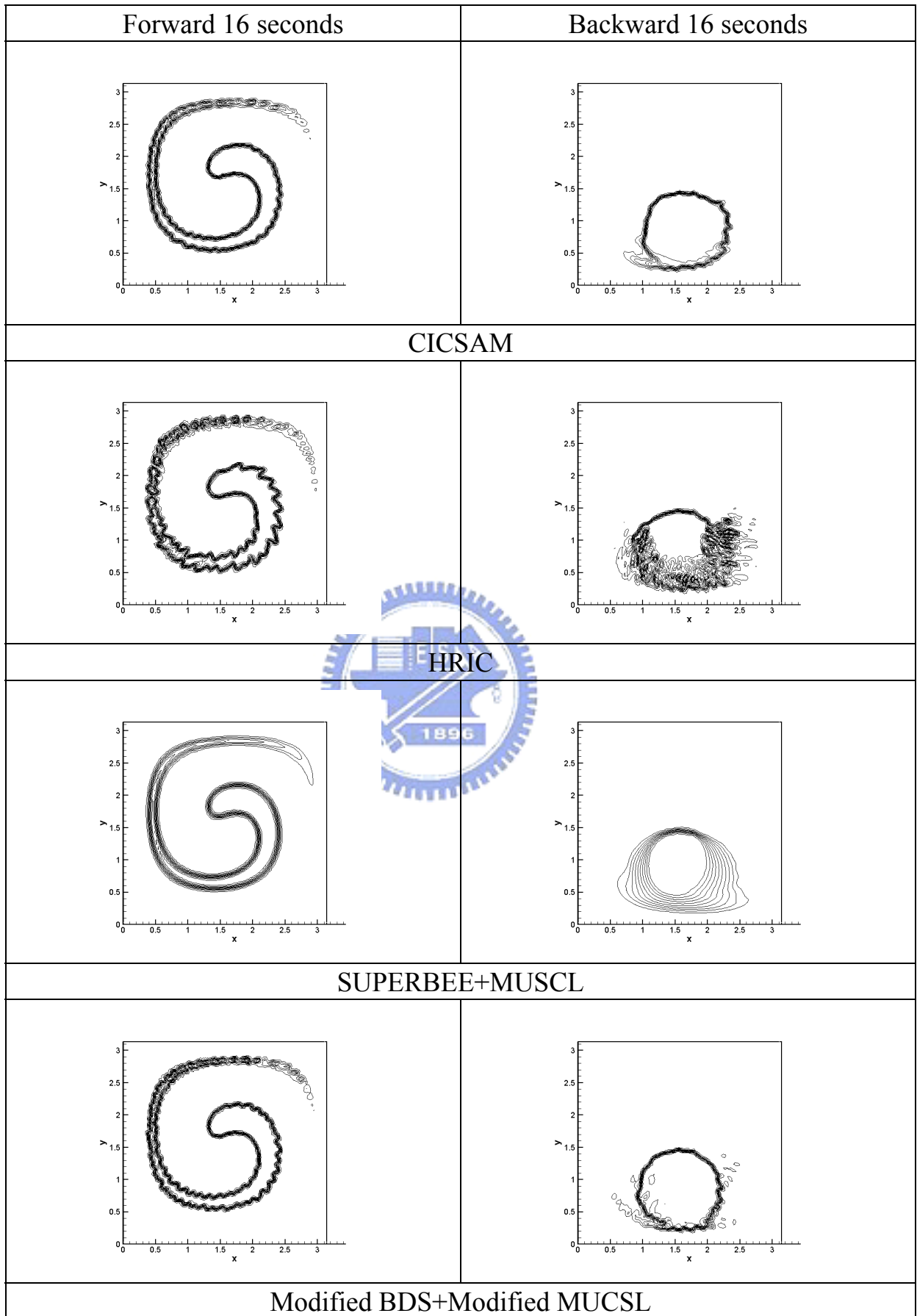


Figure 5.29 The volume fraction distribution in shear flow with  $Co=0.75$  (triangular mesh)

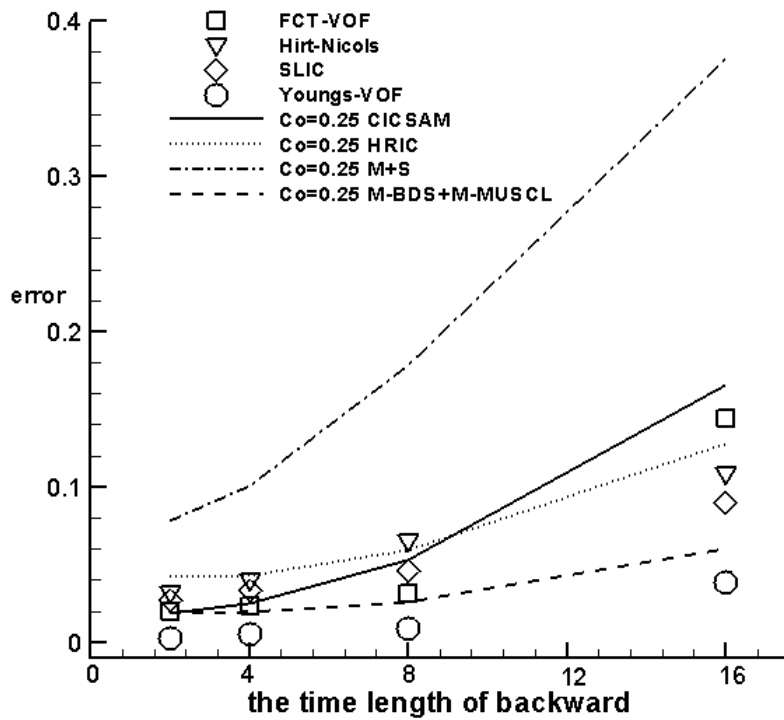


Figure 5.30 Comparison of errors in the shear flow with  $Co=0.25$  (quadrilateral mesh)

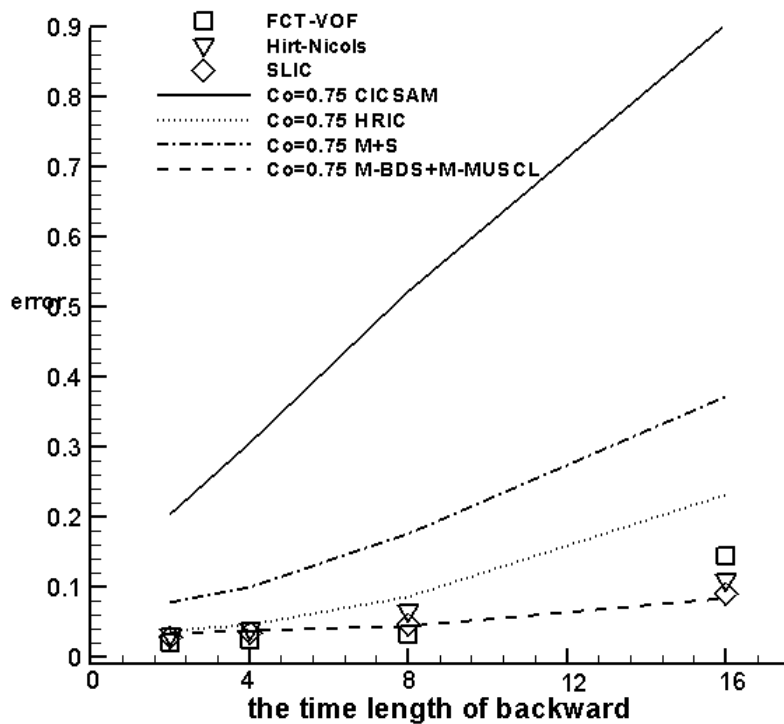


Figure 5.31 Comparison of errors in the shear flow with  $Co=0.75$  (quadrilateral mesh)

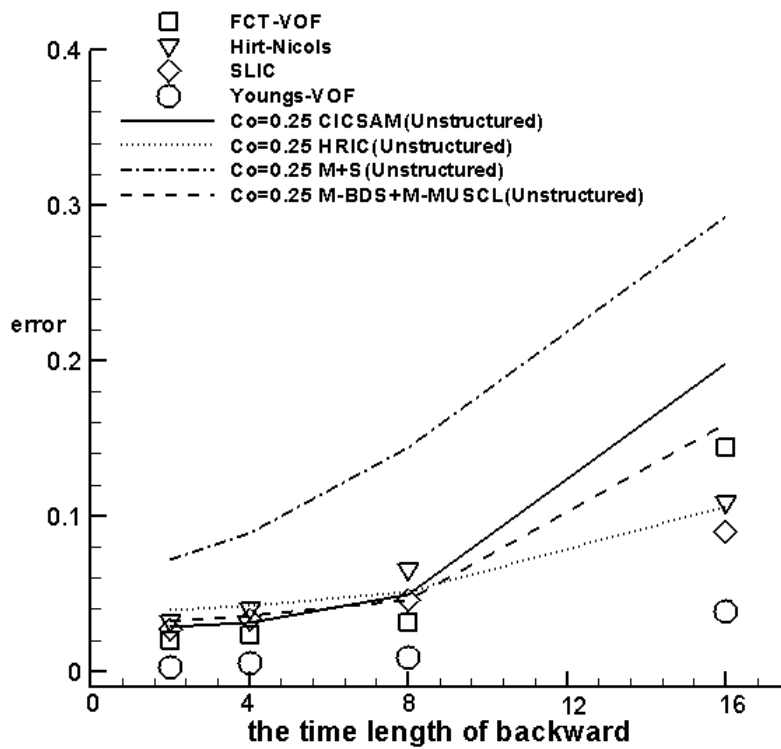


Figure 5.32 Comparison of errors in the shear flow with  $Co=0.25$  (triangular mesh)

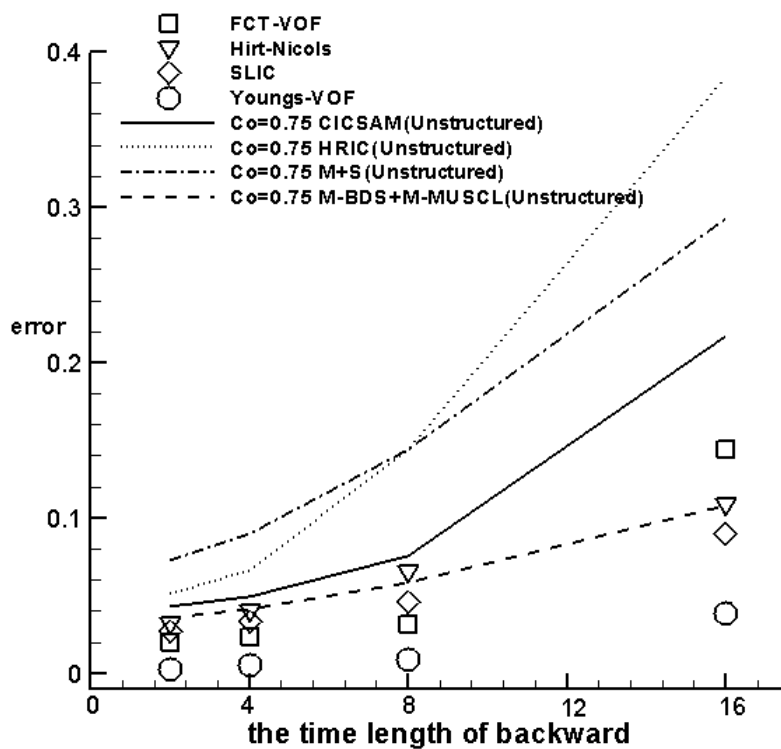


Figure 5.33 Comparison of errors in the shear flow with  $Co=0.75$  (triangular mesh)

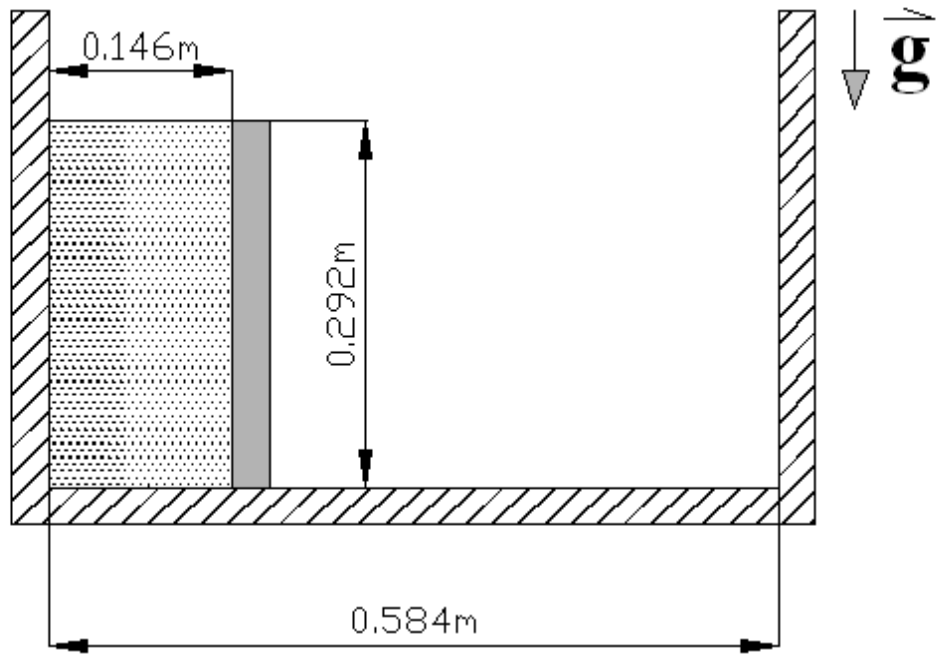


Figure 5.34 Schematic of the broken dam



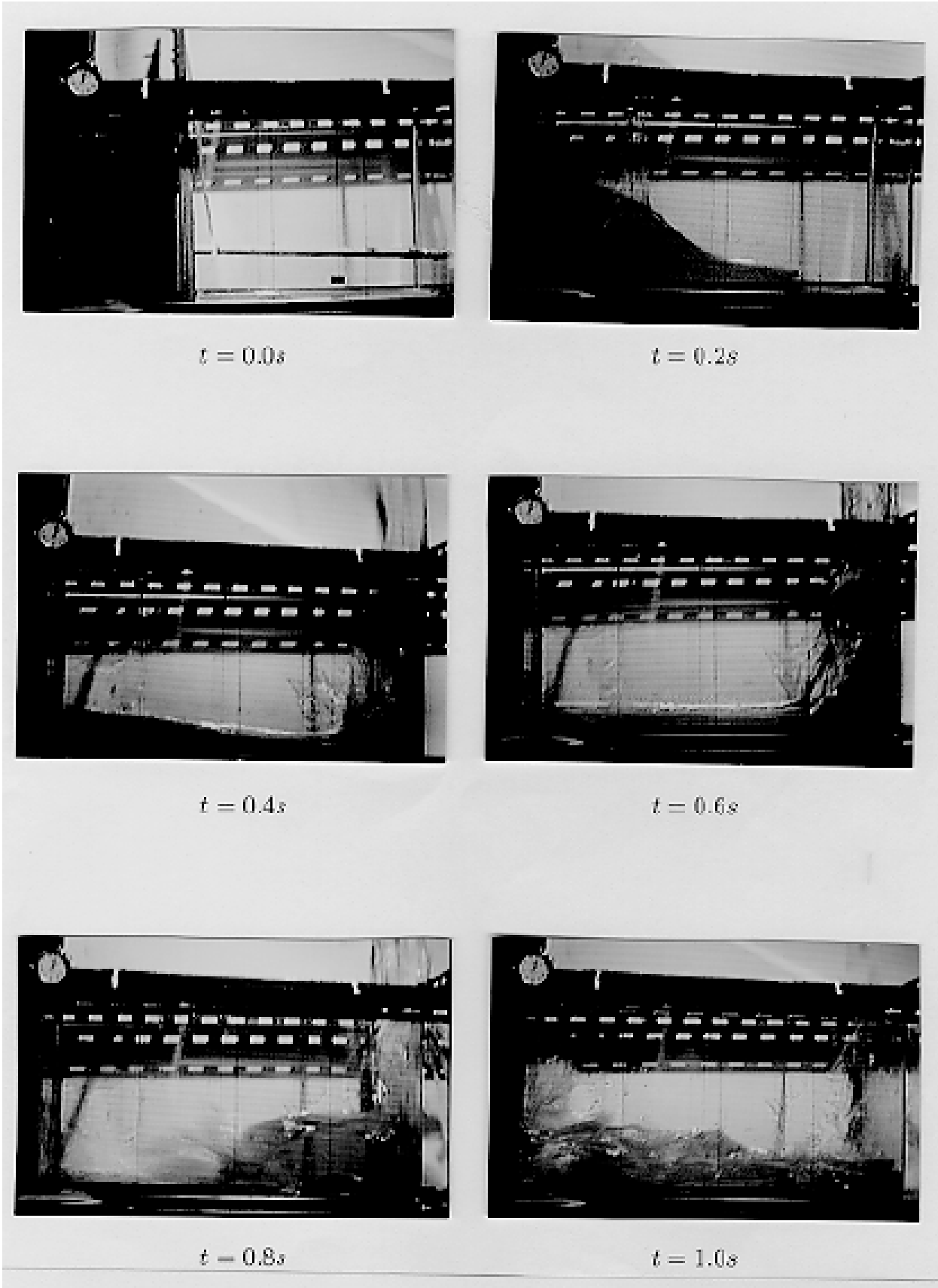


Figure 5.35 Experimental results of a collapsing water column by Koshizuka

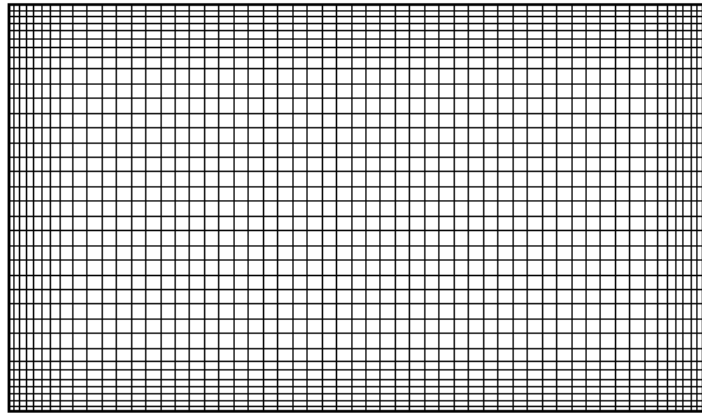


Figure 5.36 Schematic representation of the non-uniform and quadrilateral mesh with  $56 \times 36$  grids in broken dam

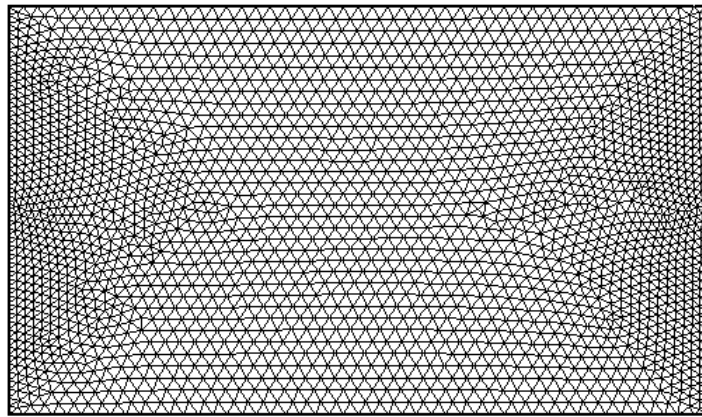


Figure 5.37 Schematic representation of the triangular mesh with 4506 cells in broken dam

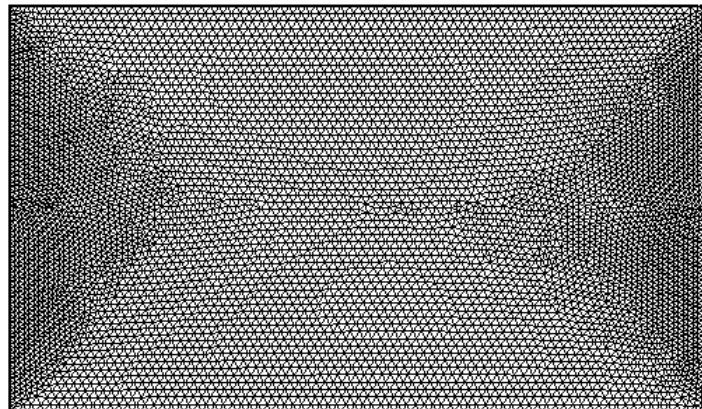


Figure 5.38 Schematic representation of the triangular mesh with 12354 cells in broken dam



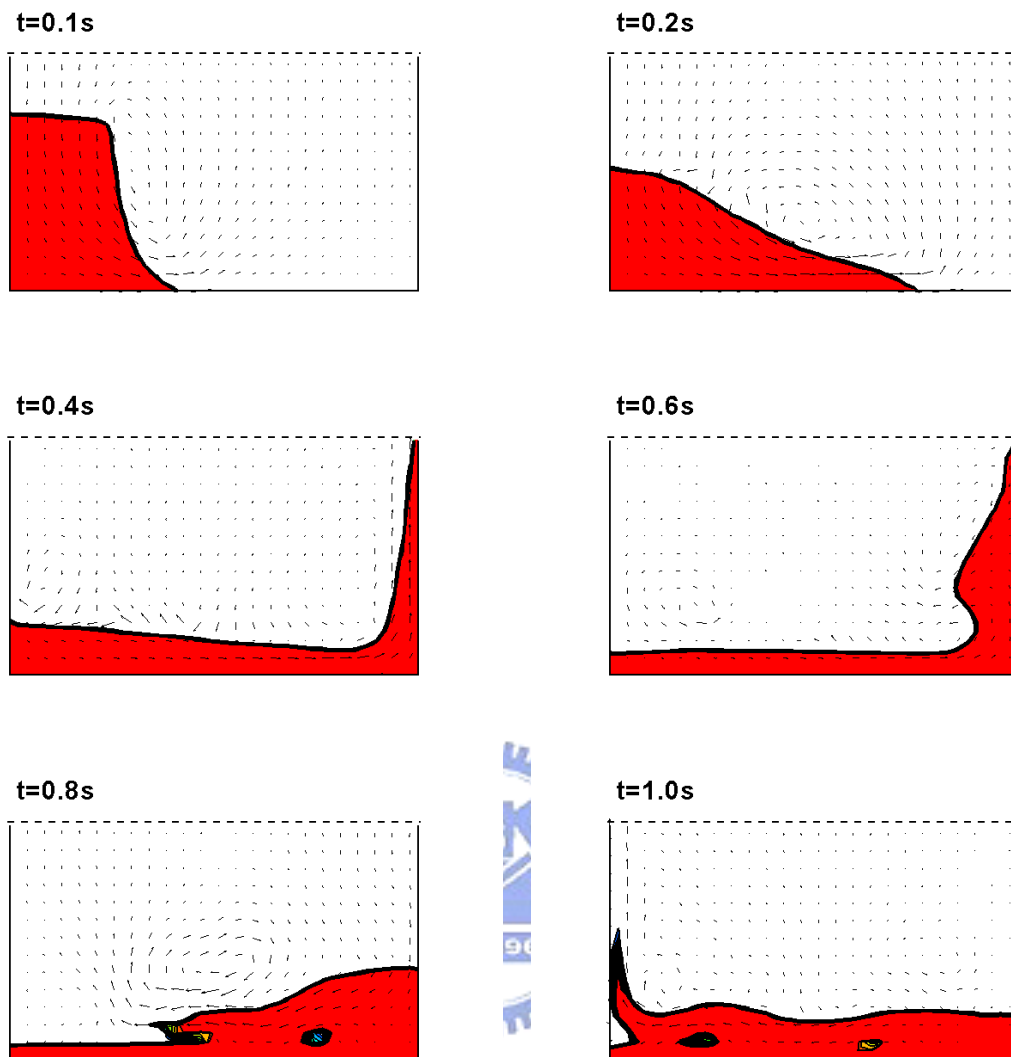


Figure 5.39 Numerical results of the broken dam on the uniform and quadrilateral mesh with  $48 \times 28$  grids

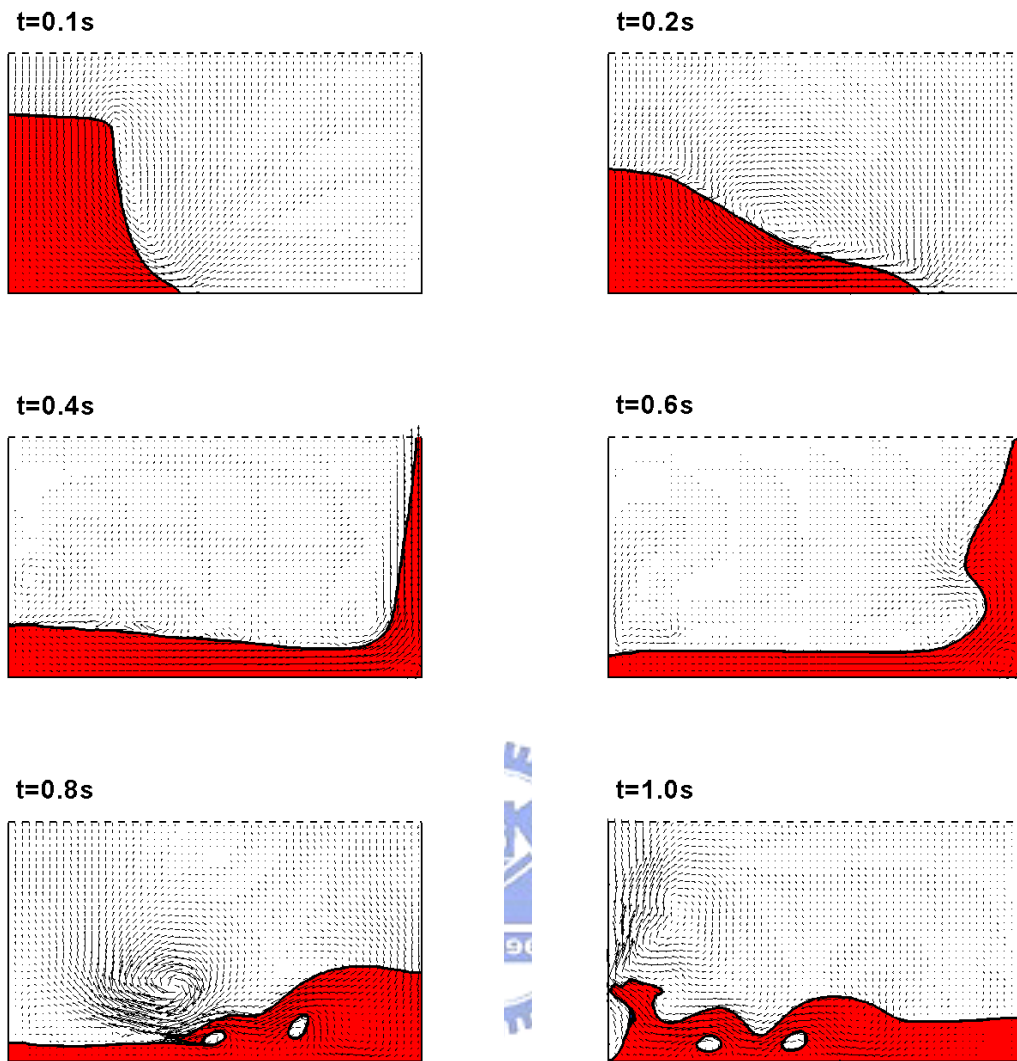


Figure 5.40 Numerical results of the broken dam on the uniform and quadrilateral mesh with  $120 \times 70$  grids

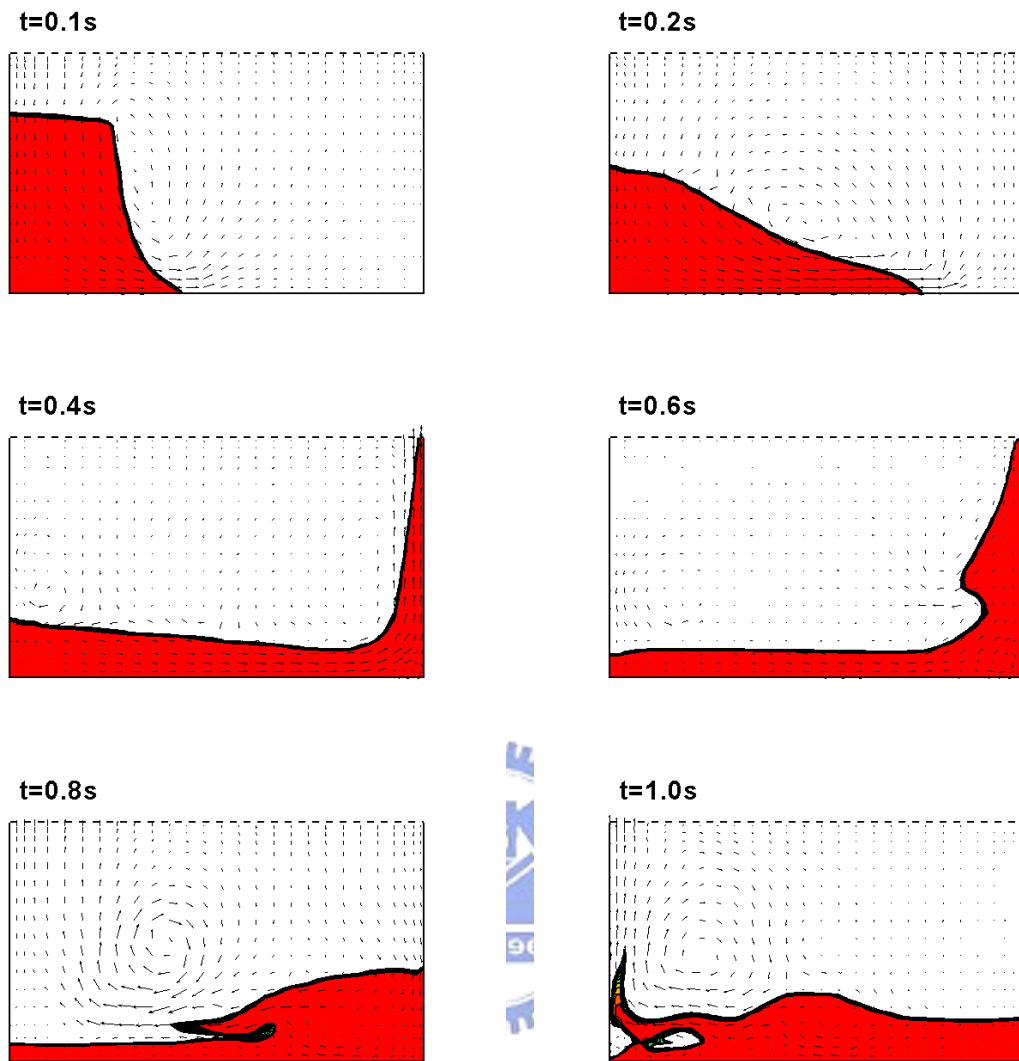


Figure 5.41 Numerical results of the broken dam on the non-uniform and quadrilateral mesh with  $56 \times 36$  grids

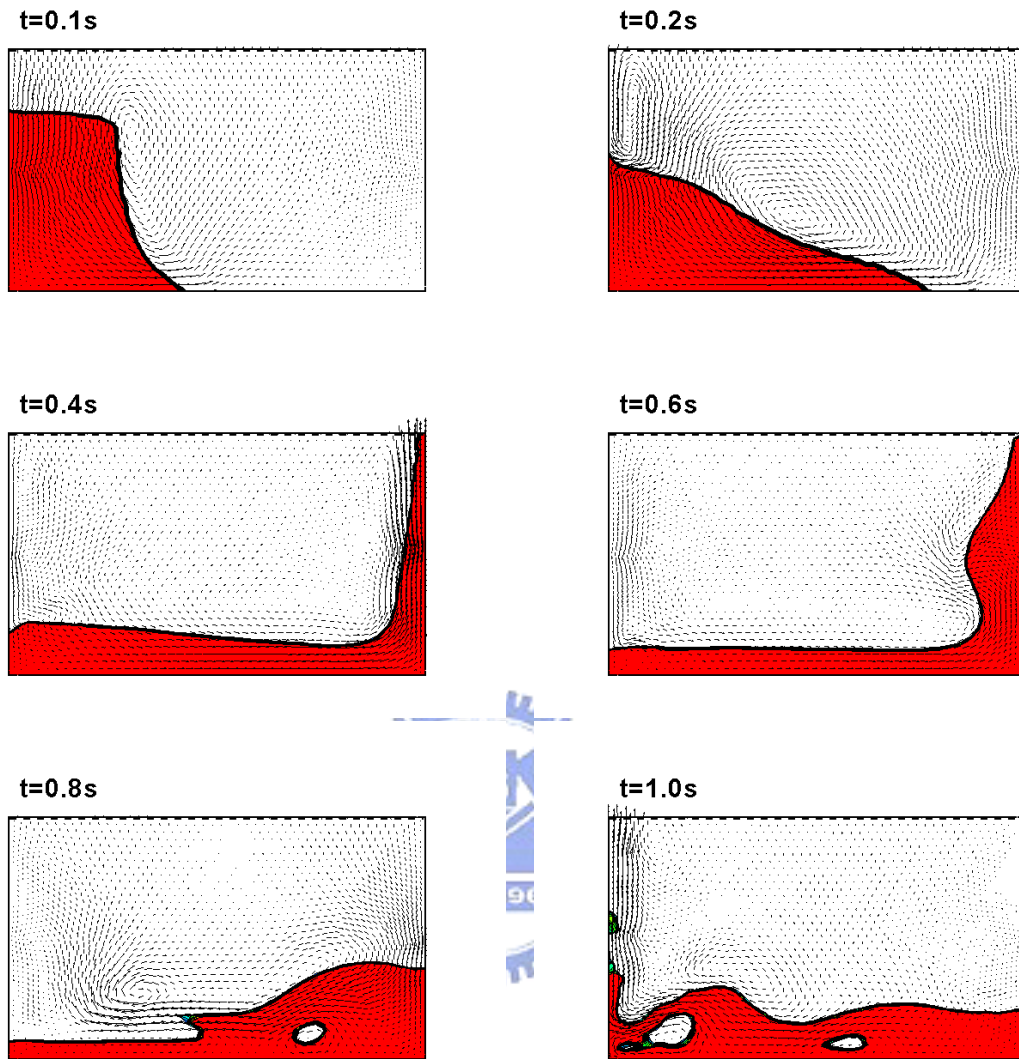


Figure 5.42 Numerical results of the broken dam on the triangular mesh with 4506 cells

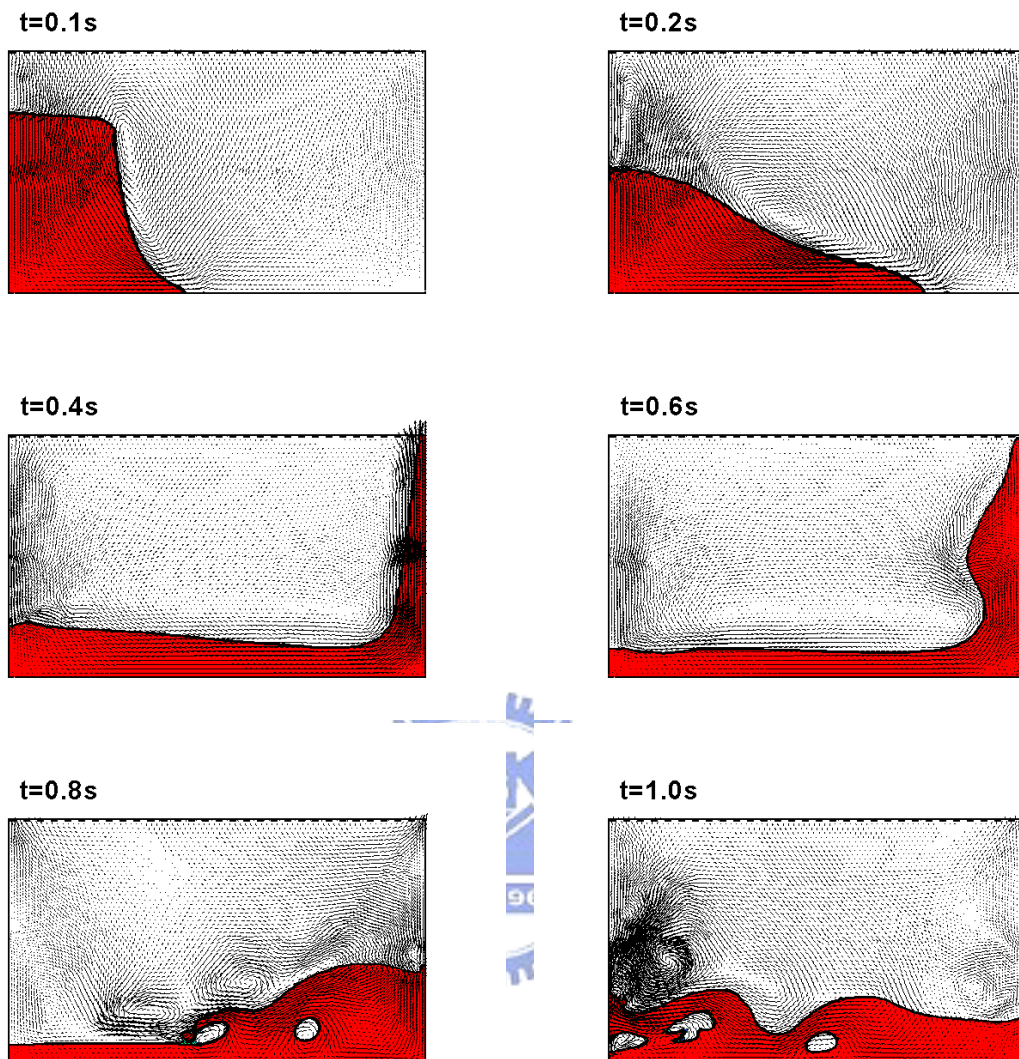


Figure 5.43 Numerical results of the broken dam on the triangular mesh with 12354 cells

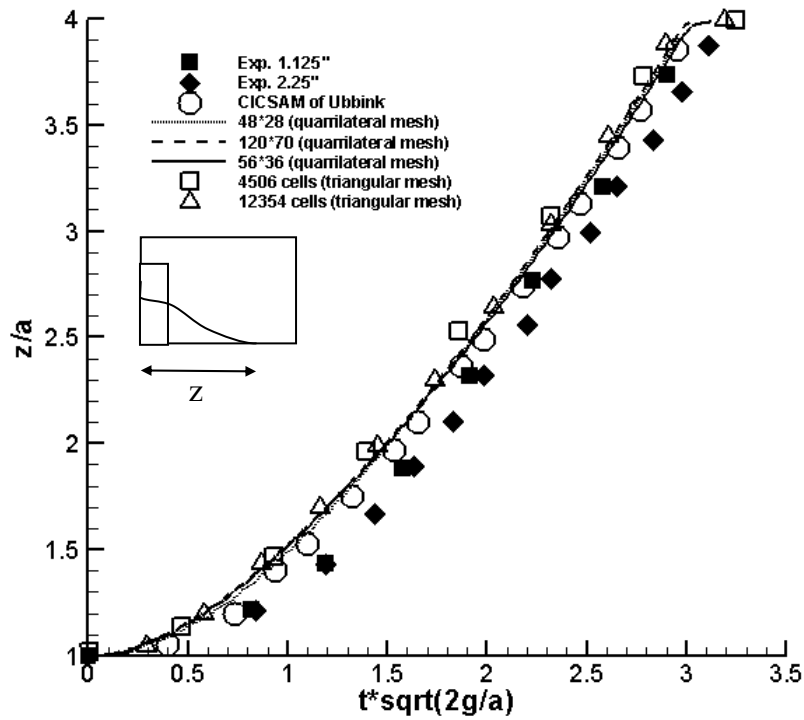


Figure 5.44 The position of the leading edge in broken dam

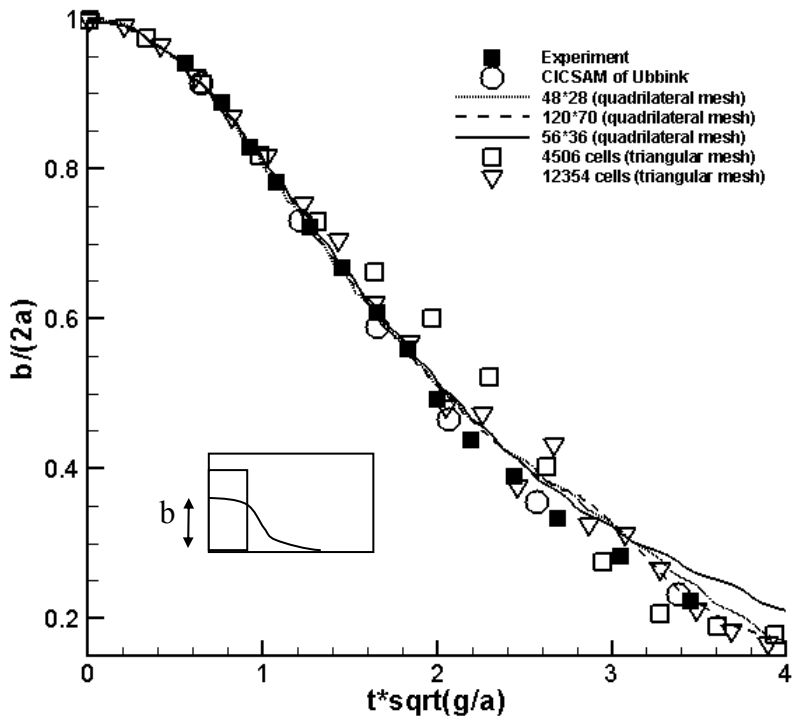


Figure 5.45 The height of the collapsing water in broken dam

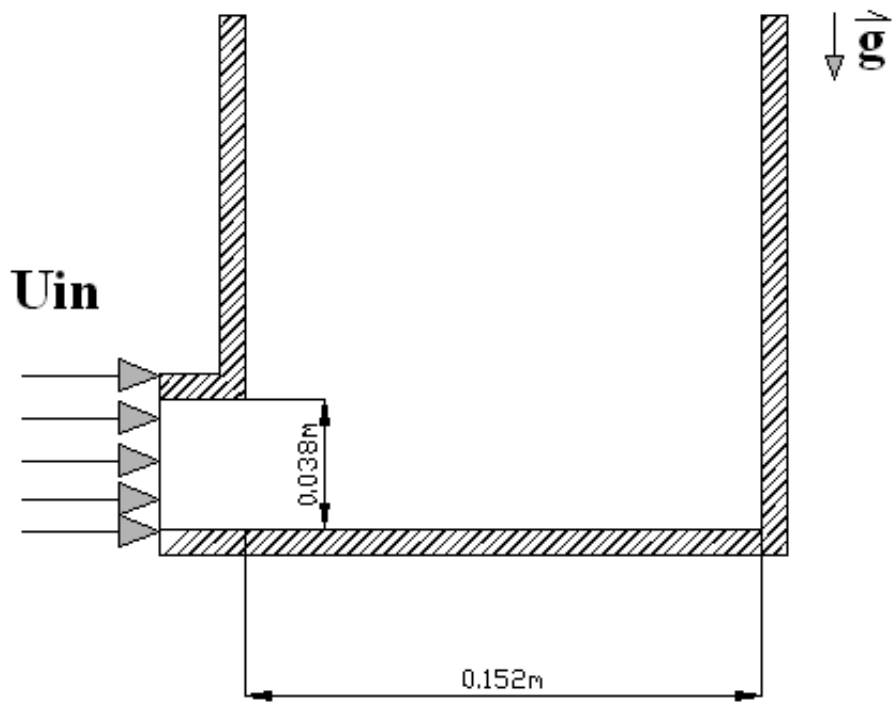


Figure 5.46 Schematic representation of the filling process in an open tank

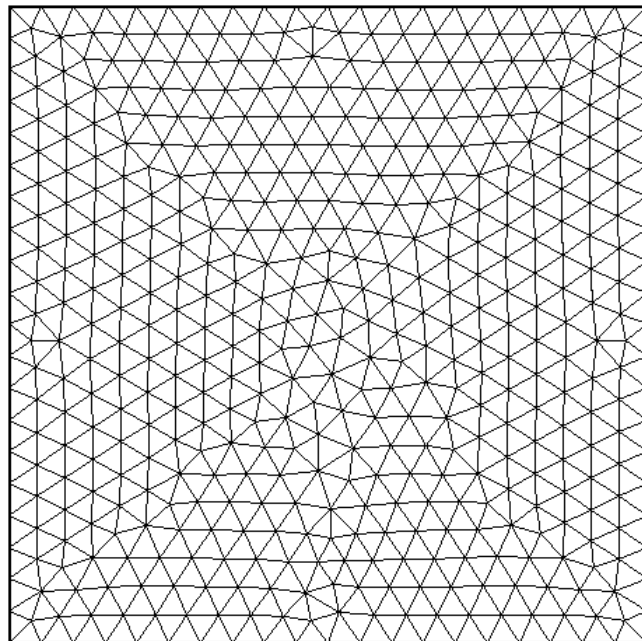


Figure 5.47 Schematic representation of the triangular mesh with 902 cells in filling process

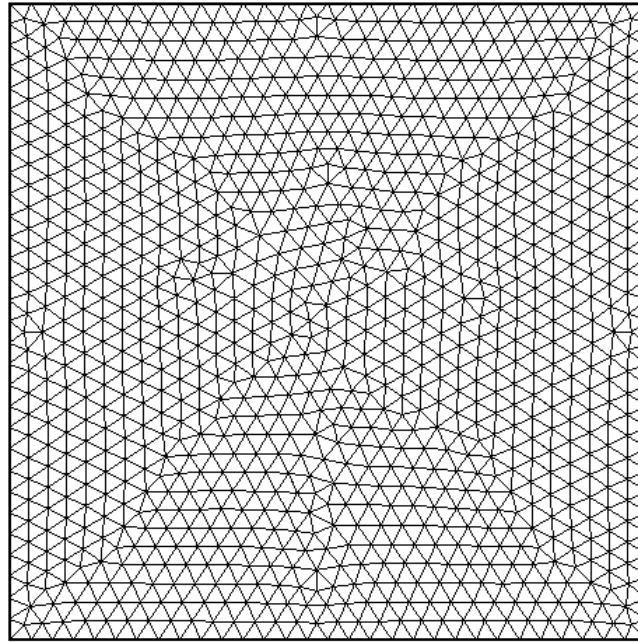


Figure 5.48 Schematic representation of the triangular mesh with 2024 cells in filling process

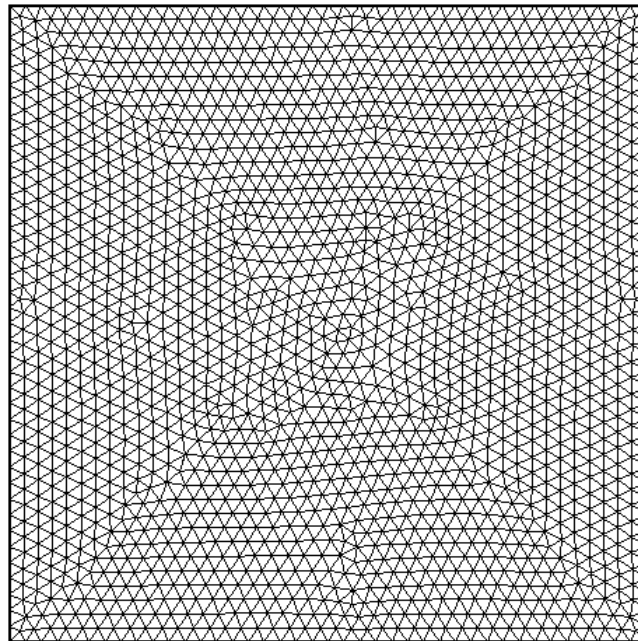


Figure 5.49 Schematic representation of the triangular mesh with 3584 cells in filling process



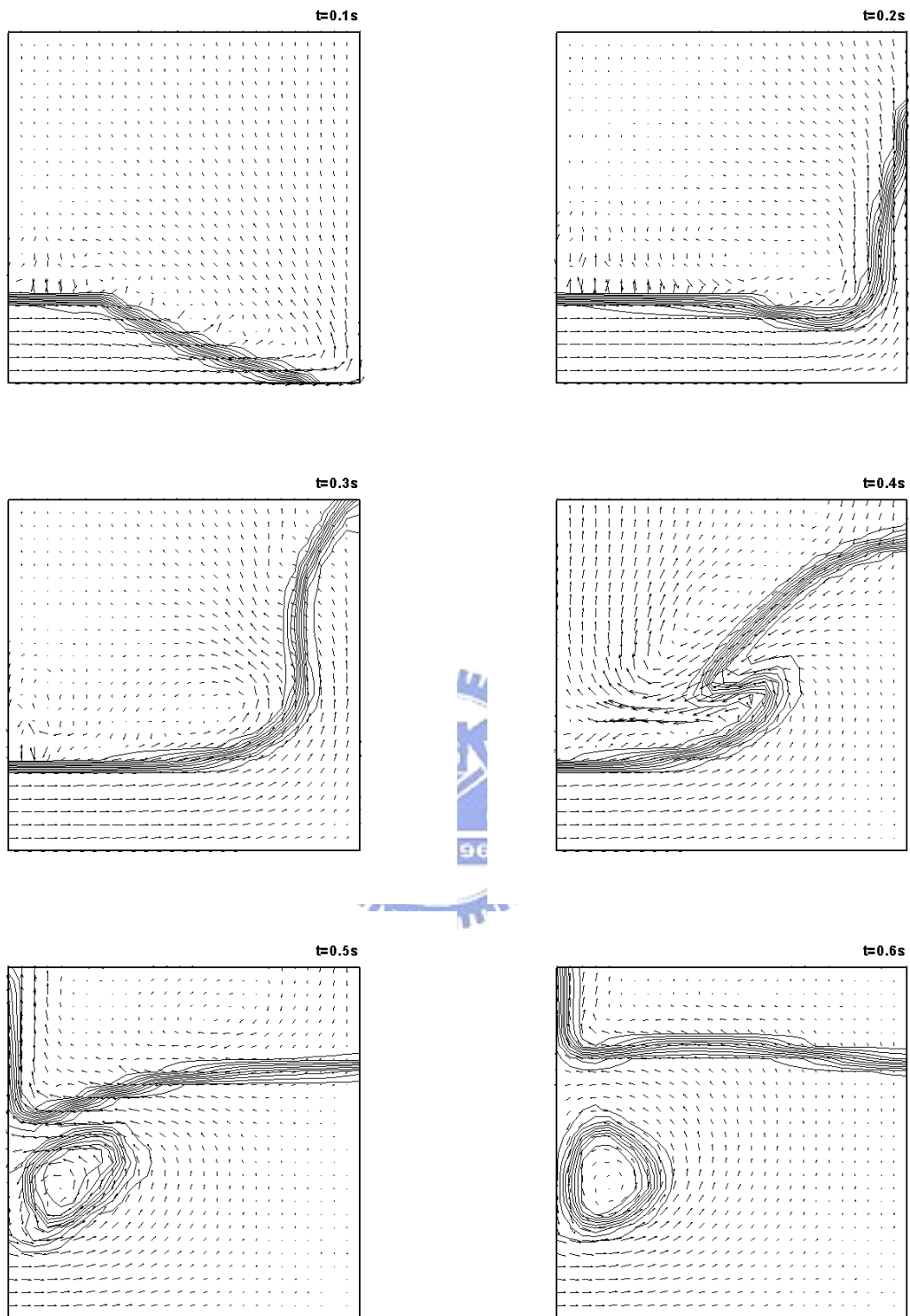


Figure 5.50 The volume fraction distribution and velocity field of the filling process on the uniform and quadrilateral mesh with  $28 \times 28$

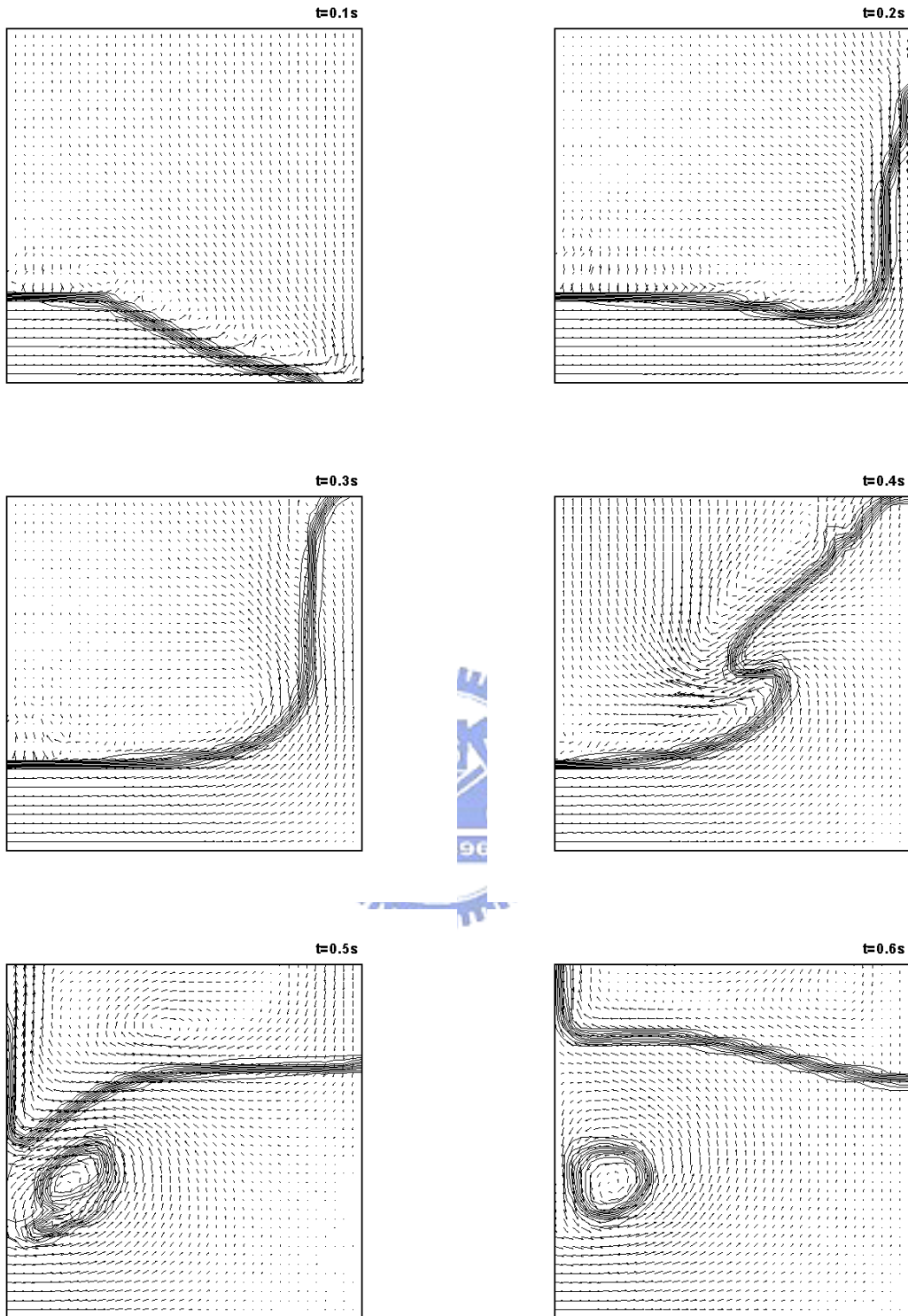


Figure 5.51 The volume fraction distribution and velocity field of the filling process on the uniform and quadrilateral mesh with  $40 \times 40$  grids

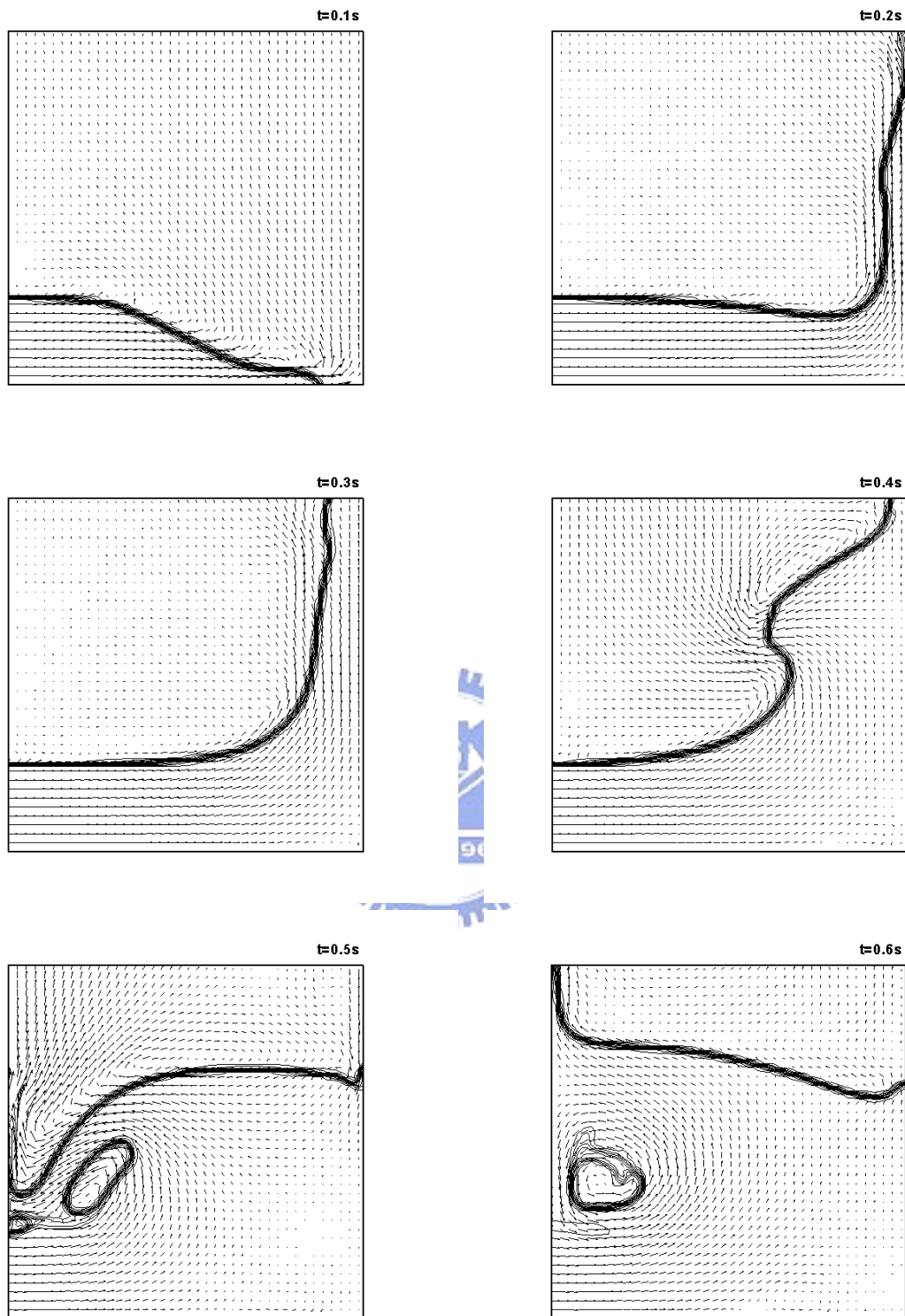


Figure 5.52 The volume fraction distribution and velocity field of the filling process on the uniform and quadrilateral mesh with  $80 \times 80$  grids

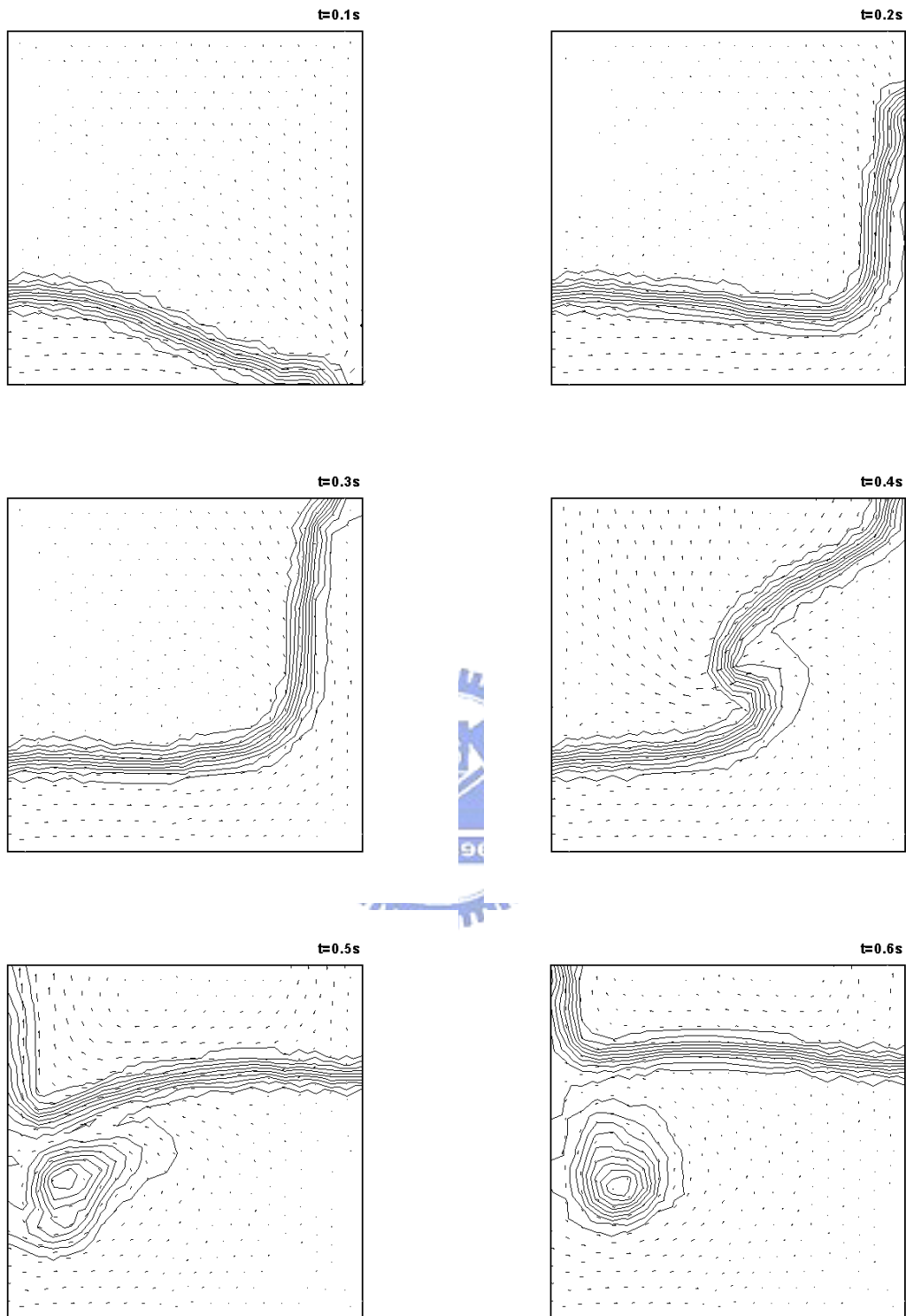


Figure 5.53 The volume fraction distribution and velocity field of the filling process on the triangular mesh with 902 cells

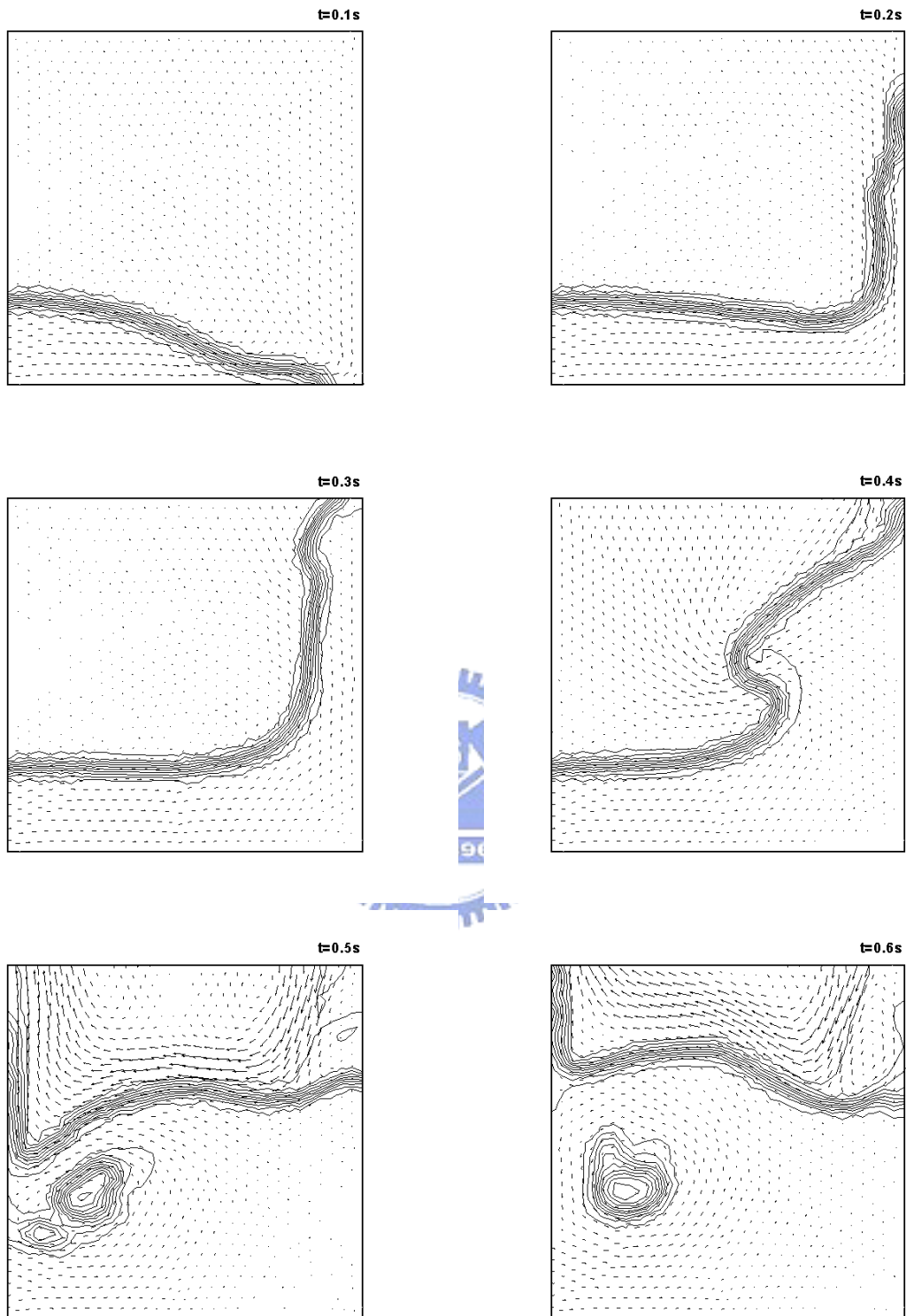


Figure 5.54 The volume fraction distribution and velocity field of the filling process on the triangular mesh with 2024 cells

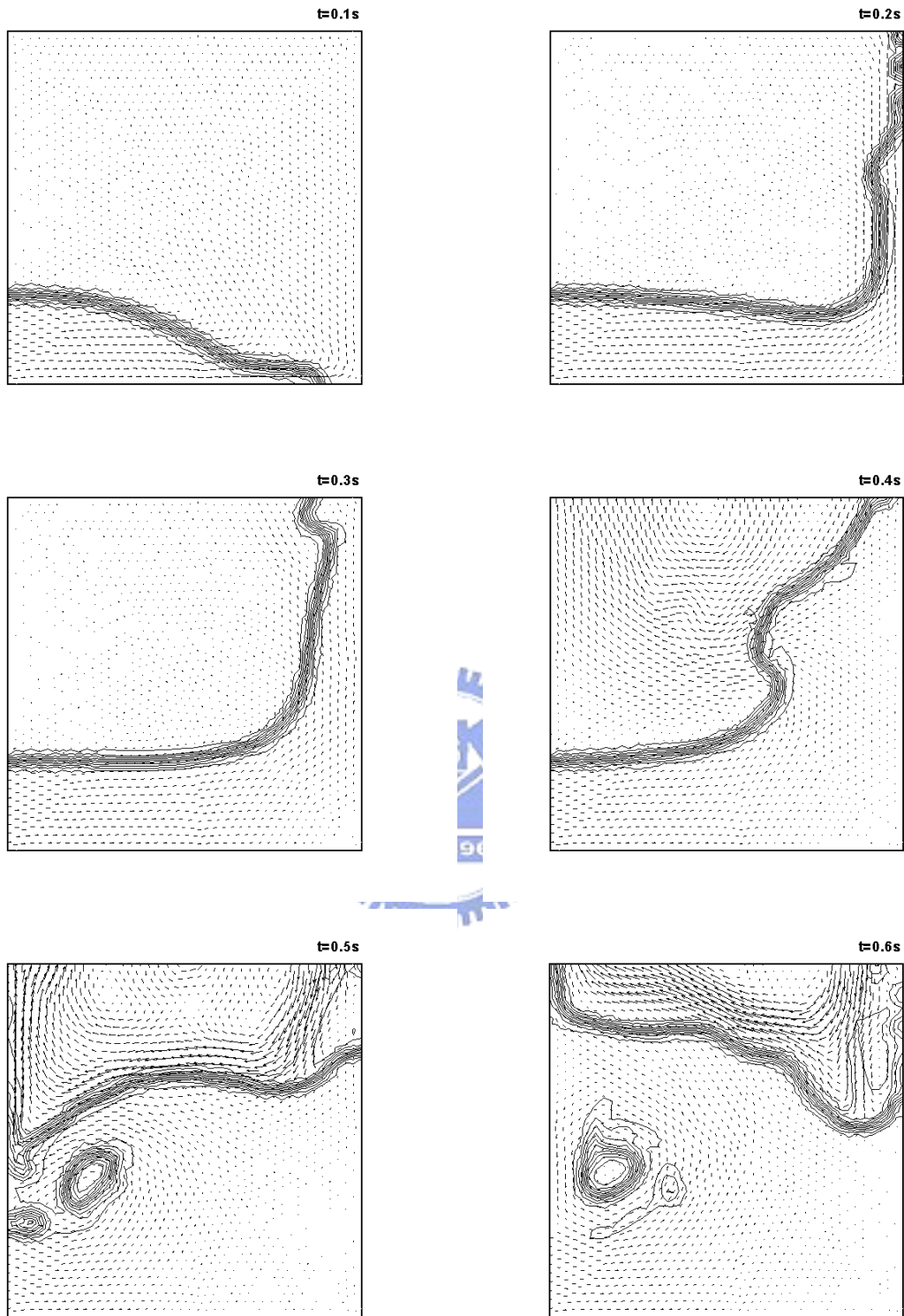


Figure 5.55 The volume fraction distribution and velocity field of the filling process on the triangular mesh with 3584 cells

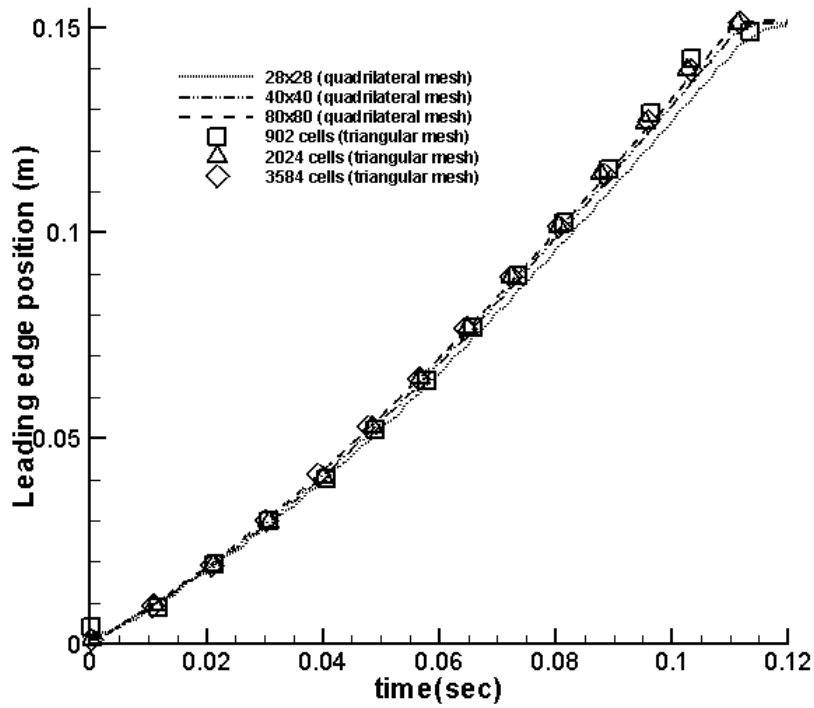


Figure 5.56 The position of leading of the filling process in the open tank

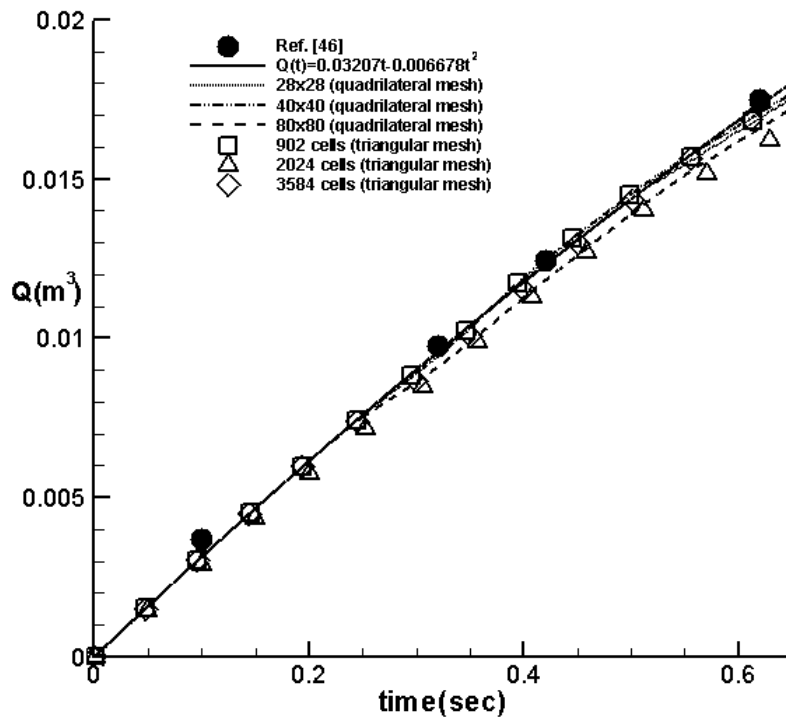


Figure 5.57 The water volume inside the tank